MOLECULAR DYNAMICS MODELING OF INTERFACIAL PLASTICITY IN NANOMATERIALS

CHEN KAIGUO

Ph. D

The Hong Kong Polytechnic University

2015

The Hong Kong Polytechnic University

Department of Mechanical Engineering

Molecular Dynamics Modeling of Interfacial Plasticity in Nanomaterials

CHEN Kaiguo

A thesis submitted in partial fulfillment of the
requirements for the degree of Doctor of
Philosophy

September 2014

CERTIFICATE OF ORIGINALITY

I hereby declare that this confirmation report is my own work and that, to the best of my knowledge and belief, it reproduces no material previously published or written, nor material that has been accepted for the award of any other degree or diploma, except where due acknowledgement has been made in the text.

CHEN Kaiguo (name of student)

Dedicate to my parents

CHEN Peigeng (陈培根)

And

XIE Xiaoling (谢小林)

ABSTRACT

The interface has been confirmed over the last decade as playing a key role for nanomaterials, and has attracted widespread attention from research communities. It is not surprising that interfacial plasticity becomes much more pronounced in nanomaterial than in conventional materials due to the dramatic increase in interface atom fraction with decreasing geometric or structural material size to the nano scale. Boundless possibilities of interfacial plasticity have opened a window for developing materials with both high strength and ductility, which has been a long-standing goal for material scientists. Current knowledge obtained from different nanomaterials, such as nanocrystalline metals, nanotwinned materials, nanolaminates, nanowire and structural biomaterials, indicates that the ability of an interface to carry and transmit plastic events corresponds to the materials' strengths and deformation homogeneity, respectively. However, the study of interfacial plasticity has remained quite challenging both experimentally and theoretically due to the complexity originating from the fact that the problem relies on both external loading conditions and internal microstructure, the latter have numerous possibilities.

The interfacial plasticity in several typical nanomaterials has been investigated in this work by molecular dynamics (MD) simulation. First, a multi-mode deformation model was introduced to MD simulation of nanocrystalline copper. Abundant deformation twin (DT) lamellae developed during shearing following compression to the elastic limit. The DTs nucleated through two different mechanisms facilitated by Shockley partial slips. And we also found that DTs' densities increase with increasing twin spacing. The interactions between DT and Shockley partials were observed in this simulation.

Second, the tensile properties along the <111> direction of single crystalline copper with 90o nano twins are investigated by molecular dynamics simulation. The following results are observed. First, twin boundaries do not serve as a dislocation source at the very beginning of plastic deformation; instead, dislocations nucleate inside the crystal between the twin boundaries. Second, twin boundaries provide obstacles to the motion of dislocations on the inclined glide plane, and allow dislocations to move through under high stress. When the spacing of the twin boundaries is greater than 10 nm, deformation twinning starts to form during plastic deformation. Third, the flow strength of single crystal copper with nano twins increases as the twin spacing decreases, which resembles a Hall-Petch-like relationship. The strengthening mechanism is explained by a simple dislocation model.

Third, the properties of Cu46Zr54 amorphous/crystalline interface and their effects on mechanical responses are studied via molecular dynamics simulation. Structural heterogeneity is observed in a Cu46Zr54 layer with both an as-quenched sample and a separately-quenched sample. A new multi-yielding scenario of interfacial sliding and the thickening of micro sliding bands is proposed by our simulations. During shear deformation, both samples yield first via the formation of shear transformation zones (STZs) in amorphous layers. After the STZ formation, micro sliding bands with highly localized atomic shear strain are developed in both samples via different interfacial mechanisms, sliding via STZs growth at ACIs for the separately-quenched sample and sliding via dislocation loop spreading at ACIs for the as-quenched sample. The thickening of micro sliding bands on an amorphous layer via internal friction is found to be a new plastic deformation mechanism when loading conditions are appropriate. The thickening rate in the as-quenched sample is higher than that in the separately-quenched sample. Finally, a crystalline layer yield via partial dislocation slip. An analytical model suggests that this new multi-yielding scenario should be expected to operate in bulk metallic glass based composites.

Finally, by utilizing molecular dynamics, tensile deformation of copper nanowire with an amorphous $Cu_{46}Zr_{54}$ coating layer is simulated. Even though the presence of the amorphous coating layer on the surface of nanowire is quite common, its impact on mechanical response has not been discussed. Unprecedented size-dependent elasticity and plasticity in atomistic simulations is observed in core-shell nanowire. Results show that both Young's modulus and the yield strength of copper nanowire are significantly reduced by the amorphous layer and decrease with decreasing nanowire diameter and increasing coating thickness. A simple core-shell model is presented to explain our results and may explain experimental results. After elastic response, the amorphous layer yields first via formation of shear transformation zones (STZs) and can further suppress the serrated flow of copper nanowire because STZs provide continuum dislocation nucleation sites, avoiding the establishment of dislocation starvation states in nanowire.

This dissertation includes a diverse discussion of interfacial plasticity in four nanomaterial models, as revealed by molecular dynamics. The atomic details of several interface-mediated plastic deformation mechanisms are presented. A bridge between knowledge obtained by MD simulations and the macro mechanical properties of nanomaterials is shown. The results help us to further understand material behavior from an angle of interface-mediated plastic deformation. We believe that this dissertation may help to design high strength and high ductility materials via introducing appropriate interfacial plasticity.

Keywords: interfacial plasticity; nanomaterials; nanocrystalline; nano twin; nanolaminate; amorphous/crystal interface; nanowire; coating; deformation twin; dislocation; nucleation;

PUBLICATIONS

Journal Papers:

1. **Chen K**, Shi S-Q, Lu J. Deformation twins induced by multi-mode deformation in nanocrystalline copper. Philos Mag Lett. 2013;93:490-7.
2. **Chen K**, Shi SQ, Lu J. Tensile deformation properties of single crystal copper with nanotwins. Computational Materials Science. 2014;83:269-76.
3. **CHEN Kaiguo**, SHI SQ, ZHU WJ. Interfacial sliding dominated plastic deformation in amorphous/crystalline nanolaminates. Submitted.
4. **CHEN Kaiguo**, SHI SQ, ZHU WJ etc. Effect of amorphous Cu46Zr54 coating layer on the mechanical response of copper nanowire. To be submitted.

Journal Papers in preparation:

1. **CHEN Kaiguo,** SHI SQ etc. On mechanical response of coated copper nanowire, in preparation.
2. **CHEN Kaiguo,** ZHU WJ, SHI SQ etc. Shockwave propagation in nanolaminates, in preparation.

Conference Papers:

1. Chen K, Shi SQ, Lu J. Deformation Twin Induced by Multi-strain in Nanocrystalline Copper: Molecular Dynamic Simulation. Proceedings of the 1st World Congress on Integrated Computational Materials Engineering (ICME)

ACKNOWLEDGMENTS

First of all, I would like to express my sincere gratitude to my chief supervisor, Prof. San-Qiang Shi, without whose wisdom and guidance this thesis would not have been possible. His never-ending patience, passion for research, rigorous attitude to science has affected me for these years. Prof. Shi supported me during a critical phase of my life, from 25 to 30 years old. He also financially funded me all these years. Prof. Shi led me to a beautiful world of computational material science. Most importantly, he trained me as a true researcher. What I have learned under his mentoring, not only knowledge but also attitudes, will benefit my whole life and shed light on me in the long journey of science.

I would like to thank Prof. Lu Jian at HKCU, Prof. ZHANG Tongyi at HKUST and Prof. WANG Yunzhi at OSU for many exciting discussions. I would also like to express my gratitude to Prof. ZHU WJ and Prof. HE HL at CAEP, for their supports and providing help by thoughtful discussions. I also thank Dr. Sanket Sarkar, Gao Yipeng, SHI Rongpei, and ZHAO Pengyang for their help during my visit to OSU.

I am thankful to many faculty members in department of mechanical engineering at PolyU who helped me these years. I take this opportunity to thank Prof. ZHOU Liming, Dr. ZHENG GP, Dr. YANG Yong (currently at HKCU), Dr. Fung and many others. My labmates-Dr. XU Hao, Dr. ZHANG Xiaochun, Dr. XIAO Zhihua, Dr. FAN Rongping, Dr. KUANG YD, and my friends- Dr. LUO Jiaqing, Dr. LIU Xiaofan, Dr. XU Liang, LI Bing, HOU Jia, and many others deserves special mention for making my Hong Kong days full of fun and for helping me selflessly. Without them, even as one of the

most prosperous cities all over the world, Hong Kong would not be attractive to me.

Most importantly, I would like to express my gratitude to my parents and my entire family for their love, support and encouragement.

Finally, I acknowledge the Research Grants Council of Hong Kong and the Hong Kong Polytechnic University for financial support.

TABLE OF CONTENTS

LIST OF TABLES.

LIST OF FIGURES

Chapter 1: Introduction

Motivations

A long standing goal in the material scientist community is to find both strong and ductile materials to meet fast advancing requirements from developing industry, including that of ground transportation vehicles, energy, aerospace, etc... Future structural materials should be strong and ductile enough to bear extremely high load with significant resistance to failure. It's well known that materials' mechanical responses are determined by their microstructures. To achieve strong ductile materials, the manipulation of deformation and plasticity at multiscale by controlling microstructures is a confirmed necessity. Interfaces play a key role in this process for their widespread presence in materials and ability to nucleate plastic deformation carriers and hinder or stagger those carriers' propagations. Because interface atoms' fractions increase inversely with grain size, it's not surprising that interfacial plasticity becomes much more pronounced in nanomaterials than in conventional materials. In this dissertation, discussion will be restricted to metallic system due to metals' wide deployment in human society and also because of the simplicity for modeling.

Three emphases should be made in illustrating the necessity of study on interfacial plasticity in metallic nanomaterials. The first is that high density interfaces make nanomaterials more uniform and allow them to deform more homogeneously. A perfect crystal is an extreme example of "uniform" material in which the nucleation of incipient plasticity is homogeneous. An interface is a "weak" region in comparison with crystal regions and thus makes conventional materials non-uniform at the meso scale. However, if a nanomaterial is pictured by microscopies with different scales, it should appear non-uniform at nano scale but **uniform at meso and macro scale**. In this way, nanomaterial can also be considered as uniform.

The second emphasis is that interfacial plasticity becomes dominant in nanomaterial and allows it the ability to deform “homogeneously” without fatal stress concentration. Interfacial plasticity refers to all possible plastic deformation mechanisms mediated by an interface, including interface sliding, grain rotation, interface mediated dislocation activity and so on. These mechanisms allow continuous plastic events to occur at the interface, such as dislocation emission and annihilation, and slip transferring. The strain or stress accumulation in nanomaterial thus hardly takes place, resulting in “uniform” deformation.

The third emphasis is that the condition of “small-being-stronger” can reach to the nanoscale. At meso scale, the well-known Hall-Petch relationship explains that a metal’s strength increases with d following d^{-m} in which d is a related internal microstructure feature size - for instance, grain size or the spacing between two closest non-connected interfaces - and m is a positive constant. A possible underlying mechanism behind the Hall-Petch relationship is that interfaces behave as obstacles to dislocation motion, leading to the formation of dislocation pile-ups against them that hinder further dislocation nucleation and motion. If d is at nano scale, dislocation pile-up no longer appears and the Hall-Petch relationship breaks down. However, nucleation of plastic deformation carriers, such as partial dislocation at the interface, and the intersection between these carriers and interfaces, can become dominant in nanomaterials, with the result that yielding stress reaches ideal strength. This nucleation-strengthening mechanism via the interface competes with other “softening” interfacial plasticity, including interface sliding, grain rotation.

The study of interfacial plasticity will allow us to artificially control this competition via microstructure design.

In general, interfacial plasticity relies on both internal microstructures and external loading conditions. Internal microstructures include crystalline structure and density and distribution of defects such as vacancy, dopant, dislocation, interface, void, secondary phase and so on. The countless microstructure features of material are difficult to characterize three-dimensionally. Even if only interface properties are considered to affect interfacial plasticity, these include type, internal structure, energy, free volume, and composition. Furthermore, the character and geometrical factors of other defects impinging on the interface should also be taken into account. External loading conditions include temperature, applied stress and strain rate. Due to the complexity, the study of interfacial plasticity in materials has remained quite challenging, both experimentally and theoretically.

However, quick development of high performance clusters in recent decades has allowed scientists to directly simulate the several billions of atoms which constitute a typical model of nanomaterials. Interfacial plasticity in nanomaterials thus lies within current computational capability, making the gain of atomic details, mechanism and modeling accessible via atomistic simulations. Such simulations, *e.g.* molecular dynamics simulation, have illustrated some deformation mechanisms related to interfacial plasticity in some nanomaterials. However, due to the complexity and challenges of this problem, there is still plenty of room for the study of interfacial plasticity.

Outline of content

The major goal of the present work is to model interfacial plasticity in different nanomaterials by molecular dynamic simulation. This dissertation is organized as follows. Chapter 2 provides a literature review on interfacial plasticity in nanomaterials, including nanocrystalline metals, nanolaminates and structural biomaterials. Modeling methods are discussed in Chapter 3. In Chapter 4, deformation twinning in nanocrystalline copper is studied. Chapter 5 focuses on deformation mechanisms of nanotwinned single crystal copper. Chapter 6 discusses interfacial plasticity in amorphous/crystal nanolaminates. The topic of Chapter 7 is the effect of an amorphous coating on the mechanical response of nanowire. Finally, Chapter 8 concludes this work and provides suggestions for future work.

Chapter 2: Literature review

Introduction

In this chapter, an extensive review on interfacial plasticity in nanomaterials will be provided. This chapter is organized as following. Section 2.1 gives a general overview of material strengthening. Section 2.2 provides a brief introduction to interfacial plasticity in nanomaterials. Interfacial plasticity in several typical nanomaterials, including nanocrystalline materials, nanotwinned materials, metallic nanolaminates, bulk metallic glass based composites and nano biomaterials, is reviewed in section 2.3.

2.1 General overview of material strengthening: why nanomaterial?

Microstructural characteristics of a material, including the crystalline structure and the type and distribution of defects, determine its mechanical properties, such as strength, ductility, as well as the dependence of its properties on strain rate and temperature, etc… The ultimate strength of the material is determined by its crystalline structure and atomic interactions. By using the *ab-initio* method, Ogata, Li Ju and Sidey Yip obtained the ideal shear strength of pure aluminum and copper crystals [1, 2], 2.89 and 2.18GPa, respectively. This strength is the minimum shear stress necessary to glide one adjacent FCC close-packed atomic plane in respect to another, and is also the upper strength limit of copper and aluminum materials. Their *ab-initio* calculations of twin energy revealed the underlying physics that explains the phenomenon that it’s easier for BCC metals to deform plastically via deformation twinning than FCC metals [3]. The deformation mechanisms corresponding to the ideal strengths of metals and ceramics are dislocation nucleation and micro crack nucleation, respectively, both of which can be interpreted under the framework of phonon instability [1, 4-6]. P-wave and S-wave phonon instability corresponds to cracks and dislocations, respectively. This theoretical work essentially pointed out the ideal strength of the material [2] and predict ideal yield strain but not the deformation limit [1]. The ideal strength is the ultimate goal for strength in designing materials, while the deformation limit is almost completely determined by structural defects. Another evaluation of structural materials is their fracture toughness, which is determined by both strength and deformability. The strengthening of materials should both improve strength and fracture toughness. Generally, structural materials can be divided into two groups, ductile and brittle. The former, mostly metals, has lower strength but higher deformability. The latter, including ceramics and some metals, has higher strength but lower deformability. The strengthening of materials implies both improvement of strength of ductile materials and improvement of deformability of brittle materials.

However, materials always contain defects, which determine both strength and deformability. Dislocation [7-9] in metals can reduce their strengths from ideal values to only tens to hundreds of MPa, while the presence of micro cracks and interfaces in ceramics will greatly affect the fracture toughness [10]. The strengthening of metallic materials and toughening of brittle materials has been a long-standing problem for both engineering and science [8]. The solution of this problem in the traditional theoretical framework requires tradeoff between strength and deformability. Metals with strength at GPa level can hardly maintain good deformability, while toughening of brittle materials is usually at the expense of loss of strength. However, in recent years, the development of nano ultra-strength materials has provided some new ideas for designing materials with both high strength and ductility [11-22].

In general, the smaller the scale is, the stronger the material is [23]. The scale mentioned here may be either the extrinsic geometric scale of the material or the intrinsic microstructural defect scale [24, 25]. For the former, it has long been found that when the sample scale decreases, the strength will be increased accordingly [25]; for the latter, a classic example is the Hall-Petch relationship [8, 9], which shows that the strength of metals increases with decreasing grain size, while when the grain size of the brittle ceramic materials decreases their deformability will be improved [21, 26-28]. When the defect scale in metallic materials is at the micron level or greater, the strain gradient theory [29-31], which employs the concepts of geometry necessary dislocation (GND) and statistical storage dislocation (SSD), can usually explain size-dependent mechanical properties. On this basis, H.J. Gao et al [32-34] have introduced direct description of plastic deformation mechanism to strain gradient theory. This theory has been applied in a unified multi-scale modeling framework [35-37]. However, when the material defects are characterized by the nanometer scale, the physical picture on which traditional theory relies no longer exists, new deformation mechanisms are mostly mediated by interfaces in nanomaterials [21, 23, 25, 38-48]. The structures, deformation and plastic deformation mechanisms of nanomaterial have brought new opportunities for the development of high strength and high ductility material [11, 18, 21, 49-52].

Dislocations and cracks play important roles in the deformation of metals

[7-9] and ceramics [21, 53], respectively. In conventional metallic materials, the activation of a dislocation slip corresponds to the yielding [7-9]. The plastic deformation is contributed by the dislocation slip and can be quantitatively described by the Orowan relationship [7, 54, 55], $\gamma = \rho bl$ in which γ is shear strain, ρ is dislocation density, b is Burgs vector of dislocation and l is the length of dislocation. During the slip, dislocation [7] suffers from the impedance of other structural defects, including grain boundary, precipitates, other dislocations etc… In particular, the impedance of grain boundary to dislocation causes the formation of dislocation pile ups against grain boundary and impedes further dislocation [7]. This scenario is the underlying mechanism responsible for the classic Hall-Petch relationship. Meanwhile, dislocation can multiply itself during plastic deformation via the Frank-Read source [7, 56] and cross slip (Koehler source) mechanisms [7]. Another important plastic deformation mechanism in metals is deformation twinning, which can be carried by successive dislocation actions [8, 57, 58]. Dislocation-dominated deformation and deformation twinning dominating deformation can provide metals with good deformability and make them exhibit either strain hardening or strain softening.

Brittle materials can typically sustain large elastic deformation with very high stress. When stress and strain rate are sufficiently high, micro cracks [1, 53] or shear bands [59-61] in brittle materials start to form, propagate and converge, resulting in rapid fracture. In contrast, the failure and fracture of ductile metal is much more complex, generally due to crack nucleation and growth induced by the hindrance to further plastic deformation provided by large local accumulation of dislocation [61]. In the framework of traditional theory, strengthening of ductile materials and toughening of brittle materials should be achieved via manipulation of dislocation, micro cracks and shear bands by designing the materials' microstructures. These designs are often made in a trade-off between strength and deformability. The improvement of either one is at the expense of loss of the other. The enhanced impedance to dislocation motion will induce loss of the ability to further deform plastically, while the increase in plastic deformation carried by micro crack motion in ceramics induces a corresponding decrease in strength. However, when the scale of structural defects decreases to the nanometer level, the plastic deformation mechanisms for both ductile and brittle materials are completely different from the traditional image of them: for example, the behavior of dislocations in metals will be confined to a small volume [62-69], the propagation of micro-cracks in ceramic will be greatly hindered. Meanwhile some new plastic deformation mechanisms mediated by interfaces will emerge to introduce an enhanced ability of new structural materials to plastically deform under loading.

The new deformation maps introduced at the 'nanoscale' can greatly enhance the strength of metals and the deformability of brittle materials. The nanoscale also introduces the possibility of maintaining both strength and deformability in materials. These nanostructured materials of nanoscale structural size include nanocrystalline materials, nanotwinned materials, nanolaminates, nanowire and some natural structural biomaterials.

2.2 Some examples

2.2.1 Nanocrystalline materials

Nanocrystalline materials are defined as a family of materials which are polycrystalline and whose grain size is at nanoscale [38]. The major characteristic of nanocrystalline materials is the very high fraction grain boundary atoms in the bulk. Due to this fact, dislocation structures are not stable within grain interiors because grain boundaries provide a force that attracts dislocation. It has been reported that the traditional Hall-Petch relationship breaks down in nanocrystalline materials because dislocation pile-ups no longer exist in such small grains [47, 70-75]. Thus nanocrystalline materials exhibit completely different plastic behavior than their polycrystalline counterparts, including grain boundary sliding (GB-sliding) [75-82] and migration [78, 82, 83], dislocation creation and annihilation [82, 84-90] at the grain boundary, deformation twinning [39, 91-96] via partial dislocation slip [97-101] and so on. These new plastic deformation mechanisms are all grain boundary mediated, and open a window for the improvement of material strength with sustained deformability.

Grain boundary sliding has been considered able to lead to superplasicity of materials [102]. For nanocrystalline materials with grain size <50nm, this can be the dominant plastic deformation mechanism [76, 77, 79]. GB-sliding has been thought to be produced by numerous thermally-activated atomic shear events at the grain boundary [103]. By utilizing MD simulations, Van Swygenhoven et al [79] revealed that the grain boundary sliding in nanocrystalline materials is mainly facilitated by atomic shuffling and stress-assisted free volume migration. They also showed that in materials with small grain size (<12nm), a buildup of stress across neighboring grains can be induced by GB-sliding and in turn be relieved by grain boundary and triple junction migration. The Coble creep equation can be used to estimate the contribution of GB-sliding to plastic deformation [77, 104-106]. It points out that the very high creep strain rate ($\propto d^{-3}$, with d indicating grain size) is induced by GB-sliding [105, 106]. Thus the GB-sliding mechanism becomes more and more pronounced as the grain size decreases, and thus nanocrystalline materials can exhibit reverse Hall-Petch relationship because GB-sliding results in a softening effect to materials [38, 77].

Another reason for the breakdown of the traditional Hall-Petch relationship is that dislocation pile-ups are no longer stable in nanocrystalline materials [38]. Fig. 2.1 shows that the concept of dislocation pile-ups is not valid for nanoscale grains. Fig. 2.1(a) depicts the presence of dislocation pile-ups in grain with sizes at micro scale. Dislocations can be generated via the Frank-Read source mechanism or via cross-slip mechanisms in large grains. But when grain size is reduced to the nanoscale, small grains are no longer able to provide room for dislocation pile-ups. Thus, as shown in Fig. 2.1(b), a loss of strain hardening induced by dislocation interaction should be the result. It should be noted that there is a critical grain size at which dislocation pile-ups break down. This critical size is essentially equal to the equilibrium spacing between two dislocations, as indicated by Eq. 2.1 in which G is shear modulus, H is hardness, b is the Burgers vector and v is the Poisson ratio. Below the critical grain size, dislocation pile-up can no longer exist in grains.

$$\mathrm{d} = \frac{3Gb}{\pi(1-v)H} \qquad \text{Eq. 2.1}$$

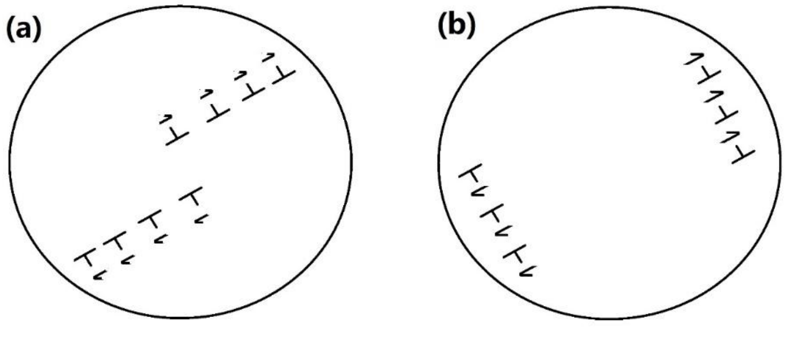

Figure 2.1. Illustration of dislocation pile up breakdown: (a) the presence of dislocation pile-up within large grains; (b) the absence of dislocation pile-up in nanoscale grains.

It has been found that dislocation behavior in nanocrystalline materials is distinct from that in their polycrystalline counterparts. MD simulations carried out by Van Swygenhoven [47, 71, 82, 84, 85, 107, 108] and others [77, 86, 109], and further TEM observations [110-112], have revealed that the dislocation density is relatively low in nanocrystalline materials during plastic deformation. This fact promotes the development of a grain boundary source-sink model [86, 89, 113-115]. It is widely acknowledged that dislocation can be formed at grain boundary ledges in polycrystalline metal [7]. In nanocrystalline metals [47, 84, 108], intrinsic and extrinsic grain boundary dislocations must be pushed out into the grains. The decomposition of grain boundary dislocations [84] is responsible for the dislocation emission from the grain boundary and results in fruitful nucleation phenomenon, including Shockley partial dislocation, full dislocation, extended dislocation and deformation twinning. The type of defect formed at the grain boundary is determined by the material’s intrinsic characteristics, including general stacking fault energy (GSFE) [116, 117]. Dislocation behavior within the grain interior also depends on the grain size. For polycrystalline materials, dislocations can multiply during a relatively long slip process via the Frank-Read source dislocation multiplication mechanism [7]. Dislocation cross-slip also occur under certain conditions [7]. Large grains always allow the formation of dislocation pile-ups, so that a dislocation slip can be impeded by repulsive force induced by the interaction of defects [7]. However, in nanocrystalline materials, such impedance to dislocation slip is no longer available. The slip of dislocation in small grains is limited by the small volume. There should be rare dislocation reactions, cross slip, or other dislocation multiplication mechanisms. Dislocations move “freely” to annihilation at the opposite grain boundary in nanocrystalline materials [47, 70]. The grain boundary behaves as both source and sink within nanocrystalline materials. The difference in plastic deformation carried by dislocation events is illustrated in Fig. 2.2.

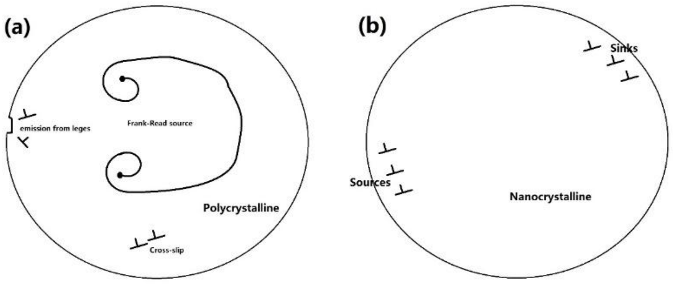

Figure 2.2. Dislocation behavior in: (a) polycrystalline materials and (b) nanocrystalline materials.

Deformation twinning competes with dislocation nucleation and slip in metals. In the traditional framework presented by M.A. Meyers et al [57], deformation twinning favors conditions such as low temperature, high strain rate, large grain size and BCC crystals. The BCC system has unique general stacking fault curves with low ratio of twin energy over stacking fault energy (SFE), so that the system can easily deform via deformation twinning [3]. According to this scenario, FCC nanocrystalline metals should not deform via deformation twinning even at very high strain rate. However, both MD simulations [91] and experiments [39, 95, 118] have confirmed the presence of deformation twinning in nanocrystalline aluminum during plastic deformation. Several twinning mechanisms at nano scale have been proposed and all operate via successive partial dislocation nucleation from the grain boundary [97, 99, 101, 111, 118-121].

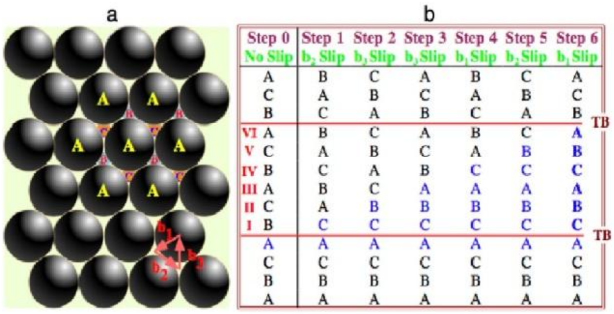

	Step 0 No Slip	Step 1 b_2 Slip	Step 2 b_3 Slip	Step 3 b_3 Slip	Step 4 b_1 Slip	Step 5 b_2 Slip	Step 6 b_1 Slip	
	A	B	C	A	B	C	A	
	C	A	B	C	A	B	C	
	B	C	A	B	C	A	B	TB
VI	A	B	C	A	B	C	A	
V	C	A	B	C	A	B	B	
IV	B	C	A	B	C	C	C	
III	A	B	C	A	A	A	A	
II	C	A	B	B	B	B	B	
I	B	C	C	C	C	C	C	TB
	A	A	A	A	A	A	A	
	C	C	C	C	C	C	C	
	B	B	B	B	B	B	B	
	A	A	A	A	A	A	A	

Figure 2.3. The RAP twinning mechanism. (a) *A*, *B* and *C* are atom stacking sequences, and b_1, b_2, and b_3 are the Burgers vectors of the partials. (b) Evolution of stacking sequence and formation of a RAP twin via the slip of partials b_2, b_3, b_3, b_1, b_2 and b_1 on layers I through VI, respectively. TB marks the two twin boundaries. Partials with negative Burgers vectors are not possible because they place two atoms on top of each other, increasing the system energy. Reprinted from Ref [101].

Fig. 2.3 shows a special deformation twinning mechanism via random activation of partials (RAP) at grain boundary, generating macro zero strain [101]. Y. T. Zhu et al. have presented an analytical model, based on classical dislocation theory, to explain the nucleation and growth of DTs in nanocrystalline Al [100]. In this model, a 60° full dislocation consisting of a 90° leading partial and a 30° trailing partial readily nucleates and grows a deformation twinning. This mechanism is easily modeled analytically. The schematic of the dislocation model for deformation twin nucleation is illustrated in Fig. 2.4. The critical shear stress for twinning and trailing partial nucleation are thus derived from an energy equilibrium approach, as depicted in Eq. 2.2 and Eq.2.3 in which *G, a, d, γ* and *ν* are shear modulus, dislocation core width, grain size, stacking fault energy and Poisson ratio, respectively. This model indicates that there is an optimum grain size range for deformation twinning nucleation in nanocrystalline aluminum and this range falls under the scope of computational capability. In contrast, the suitable grain size regime for deformation twinning nucleation in nanocrystalline copper is beyond computational capability and there is little literature regarding deformation twinning as a plastic deformation mechanism in nanocrystalline copper [116]. In addition, Van Swygenhoven et al. conclude that whether deformation twinning or trailing partials prevail in MD simulations depends on the GSF curve [116]. Again, for copper, it's difficult for deformation twinning to appear in MD simulations.

$$\tau_{twin} = \frac{Ga}{2\sqrt{6}\pi d \sin\alpha} \ln\frac{\sqrt{2}d}{a} \qquad \text{Eq. 2.2}$$

$$\tau_{trail} = \frac{\sqrt{6}}{\cos(\alpha - 30^{\circ})}[\frac{Ga(8-5v)}{48\pi(1-v)d} \ln\frac{\sqrt{2}d}{a} - \frac{\gamma}{a}] \qquad \text{Eq. 2.3}$$

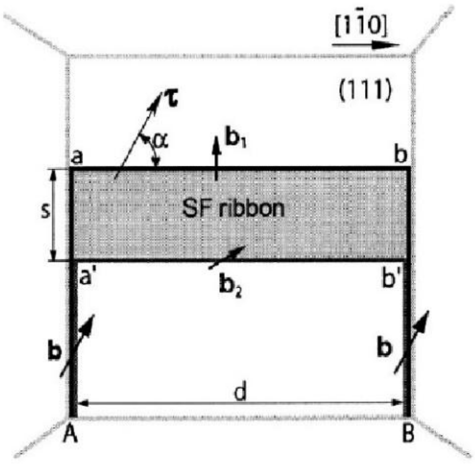

Figure 2.4. A schematic illustration of the dislocation model for deformation twin nucleation. Reprinted from Ref[100].

It should be noted that the overall yielding of nanocrystalline materials corresponds to grain boundary mediated nucleation events. Generally speaking, the "original" grain boundary dislocations in nanocrystalline materials can be decomposed into dislocations or twins in the grain interior slip dislocations. The strength corresponding to this decomposition depends on grain size and stacking fault energy rather than on interaction with other dislocations. It is worth to note that Eq. 2.2 and Eq. 2.3 reflect the fact that the strength of nanocrystalline materials depends on the nucleation mechanism, stacking fault energy and grain size. A universal scale law can be concluded from these two equations: the strength of nanocrystalline materials should scale with $1/d \ln d$ without regard to dislocation geometry. When the grain size decreases, resistance to formation of dislocation and twinning at grain boundaries increases but the contribution of grain boundary sliding to overall deformation increases, resulting in the presence of a critical grain size at which the strength of the material reaches maximum at the level of GPa. Below this critical grain size, it is well known that dislocation activity and associated stress-induced deformation within grain interior will be limited. This critical grain size has been proposed as between 10nm and 30nm, according to computer simulations and transmission electron microscopy observations. However, recent radial diamond anvil cell (rDAC) x-ray diffraction (XRD) experiments have revealed that very high hydrostatic external pressure can reduce this critical grain size to 3nm [88].

Besides the grain size, there are other controllable structural parameters to be used in designing the strength of nanocrystalline materials, including the distribution of grain size (e.g. bimodal materials), texture, grain boundary structure [122-128] and geometrical distribution [129] etc... With careful design, nanocrystalline materials should be able to carry large deformation without great loss of strength due to unique plastic deformation mechanisms. Via these grain boundary mediated mechanisms, there is little strain and stress concentration around the boundary leading to fatigue. However, due to the limitation of current manufacturing technology for preparing dense bulk nanocrystalline materials, it is still rather hard to verify whether we can achieve bulk materials both strong and tough by reducing grain size to nanoscale.

Recently some new techniques, such as surface mechanical attrition treatment (SMAT) [130-133] and the surface friction[134] method, have been developed to achieve compact nanostructure at the surface of metals. Large plastic deformation introduced by these techniques are able to significantly reduce grain size at the surface to nanoscale and induce the formation of surface layers with gradient grain size distribution. In Fig. 2.5 the typical TEM image and SEM image of SMAT treated copper show the presence of nano grains and ultrafine grains, respectively. Bulk metals, after being treated by these methods, can be considered composites consisting of ductile polycrystalline bulk and nanostructured surface layer of very high hardness. These materials exhibit both high surface strength and bulk strength - most importantly, without notable loss of ductility. Moreover, the compact, strong nanostructured surface layer can suppress propagation of surface cracks and thus greatly improve fatigue limits.

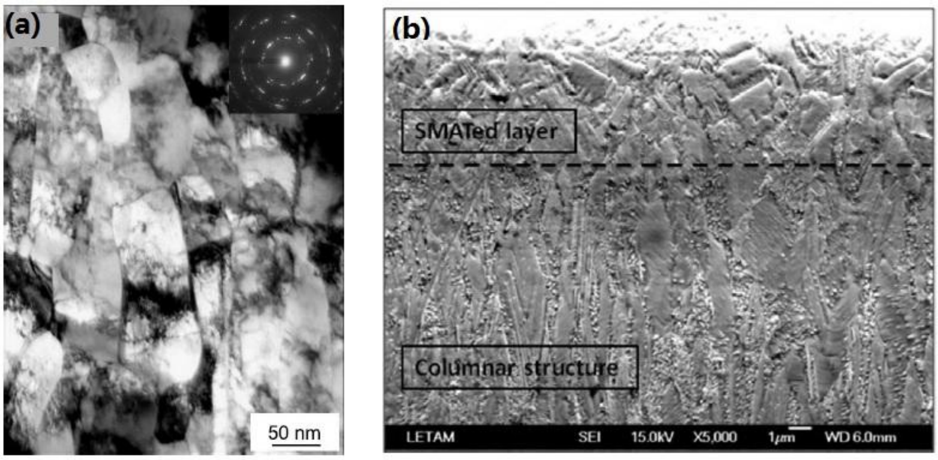

Figure 2.5. (a) TEM image of SMAT treated copper, reprinted from Ref [130]. (b) SEM image of SMAT treated copper, reprinted from Ref [131].

Studies on nanocrystalline materials have indicated that interfacial plasticity (e.g. grain boundary plasticity, in this section) at nanoscale should be substantially dissimilar to that observed at mesoscale. Generally speaking, interfaces usually hinder dislocation propagation, resulting in the formation of neighboring dislocation pile-ups and impedance to further plastic deformation via dislocation slip. But when spacing between interfaces is at nanoscale, a new deformation map appears. First, interfaces can provide continuum dislocation nucleation sources. Second, interfaces can behave as dislocation annihilation sinks. Third, interfaces can contribute to overall plastic deformation via mechanisms such as sliding. These mechanisms associated with the nanoscale can significantly reduce the possibility of stress and strain concentration, avoiding nucleation and fast development of material fatigue.

2.2.2 Nanotwinned materials

The ability of an interface to transmit plastic deformation also plays an important role in maintaining a material’s ductility [135-140]. When dislocation moves towards an interface, it suffers from a repulsive force beyond a critical distance (few nanometers). Once it interacts with the interface, the interface may emit into the adjoining crystal interior full dislocations, partial dislocations or deformation twins. It is also possible for the interaction between interface and dislocation to result in emission of dislocation either back to the grain of the incident slip system or along the interface. This can only happen at a considerable local stress level. If the spacing between interfaces is at nanoscale, this stress level can be attained rather easily. In molecular dynamics simulations, the transmission of a dislocation across interfaces is frequently observed [137, 138]. It has been concluded that the transmission process and stress depend on incoming slip systems, and incoming dislocation characteristics include screws, edges, or a mix of the two [137-139]. Interfaces always provide very high energy barriers for dislocation transmission. Mostly, the interaction between interface and dislocation only leaves an immobile dislocation on the interface plane but no dislocations in the adjoining crystal. The formation of immobile interfacial dislocation is a major cause of reduced deformability.

However, coherent twin boundary (CTB) in FCC materials is a special case. The interaction between CTB and dislocations mostly results both in dislocations in neighboring crystals and in mobile partial dislocations on CTB which only cause CTB migration but not strain accumulation on the CTB itself. Lu Ke *et al.* obtained nanotwinned copper foil by electronic deposition [18, 49, 50]. The major microstructural character of nanotwinned copper is that it contains CTBs with spacing at nanoscale in ultrafine grains. Nanotwinned copper is able simultaneously to exhibit high strength, high conductivity and considerable ductility [18]. Experiments [50, 141] and simulations [86, 142] have revealed that a maximum strength in nanotwinned materials can be achieved via varying twin boundary spacing and grain size. With a fixed grain size d, the optimal twin spacing for achieving high strength is proportional to $d^{0.5}$. Via massive MD simulations, X.Y. Li *et al.* show that there exists a transition in the deformation mechanism, occurring at a critical twin spacing [86]. At this critical twin spacing, the classical Hall-Petch type of strengthening due to dislocation pile-ups and cutting through twin planes switches to a dislocation-nucleation-controlled softening mechanism with twin boundary migration resulting from nucleation and motion of partial dislocations parallel to the twin planes. Fig. 2.6. illustrates that when twin spacing is 1.25nm, the plastic deformation is dominated by partial dislocations gliding on the twin boundary, whereas when twin spacing is 6.25nm, the controlling plastic deformation is dislocation cutting through the twin boundary. X.Y. Li *et al* have also proposed an analytical model based on nucleation theory to explain the softening effect [86]. The model is illustrated by Eq. 2.4 in which d is grain size, λ is twin spacing, ΔU is the activation energy, S is a factor representing local stress concentration and geometry, V is the activation volume, k_B and T are the Boltzmann constant and temperature, ν_D is the Debye frequency and $\dot{\varepsilon}$ is the applied strain rate. It is noted that Eq. 2.4 actually illustrates a reverse Hall-Petch relationship with varying twin spacing. By combining Eq. 2.4 and the Hall-Petch relationship with twin spacing as variable, optimal twin spacing can be deduced for each given grain size.

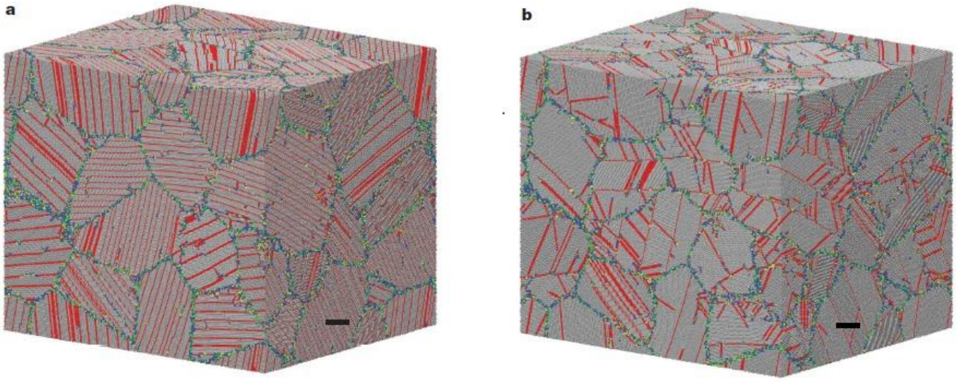

Figure 2.6. Simulated deformation patterns in nanotwinned copper with grain size of 20nm at 10% strain (scale bars, 5nm.). Samples with twin spacing of 1.25nm (a) and 6.25nm (b). Reprinted from Ref [86].

$$\tau = \frac{\Delta U}{SV^*} - \frac{k_B T}{SV^*} \ln\left(\frac{d \nu_D}{\lambda \dot{\varepsilon}}\right) \quad \text{Eq. 2.4}$$

2.2.3 Metallic nanolaminates

Metallic nanolaminates are two dimensional nanoscale laminated structures. The mechanical properties of this family of materials depend on thickness of layer and structure and properties of the interface (whether homophase or interphase) [135, 138]. Whether to allow the dislocation to transmit across the interface and whether such transmission leaves accumulative strain at the interface plays an important role in the design of material toughening for the metal [137, 138, 143-145]. In heterogeneous metallic laminates, dislocation pile-ups can be formed against the interface during deformation when the thickness of a single metallic layer is at mesoscale. The formation of dislocation pile-ups will hinder further plastic deformation around the interface, resulting in very high strength but low ductility of heterogeneous metallic laminates. This picture is similar to that of dislocation behaviors confined within large grains. But when the thickness of a single metallic layer decreases to a few tens of nanometers, plastic deformation of metallic nanolaminates will be carried by single dislocation motions confined within each phase. When the thickness further decreases to a few nanometers, dislocations are able to transit the interphase interface at considerable stress.

Four types of interphase interfaces based on geometric factors have been distinguished by Wang et al [135]. Type I are ones which are compact planes for both crystals. Type II are ones which are only a compact plane for one crystal, although there are several compact directions present in the interface. Type I and Type II interface all have periodic unit cells within the interface. Type III are ones which are compact planes for neither crystal and which do not contain compact directions on the interface, but which still have unit cells. Type IV are ones in which no geometric factors, including the compact planes, directions and unit cells of the interface, match. By employing atomistic simulations, they found out that the critical resolved shear stress for nucleation of a dislocation loop at the interface is inversely related to the interface shear resistance. When the dislocations are hindered at the interface, the dislocation transmission depends on dislocation climb along the interface, dissociation and recombination of interface defects, and nucleation and emission of a dislocation in the adjoining layer. A summation of their simulations is listed in Table 2.1. It should be noted that events related to dislocation transmission are thermally activated and thus depend on both temperature and local shear stress.

Typical examples of heterogeneous interfaces contain interfaces in Cu/Nb [146-150] and Al/Nb [151] nanolaminates, which have been successfully manufactured by the accumulative rolling band (ARB) method recently [152].

Following a specific preparation process, Al/Nb nanolaminates can contain Type I interfaces with Kurdjumov-Sachs orientation (KS) relations [146]. Dislocations are found to accumulate in the interfaces rather than within the layer. The transmission of dislocation can be achieved via dislocation climb, which depends on the diffusivity and density of vacancies within the interface. This observation agrees well with the fact that an interface is able to annihilate dislocations by the climb mechanism at room temperature [138, 140, 153]. Especially under shock loading, interfaces with KS relation in Cu/Nb nanolaminates allow direct transmission of dislocations [153-155].

Table 2.1. Correlation of interface structures and properties with interface types. Reprinted from Ref [135].

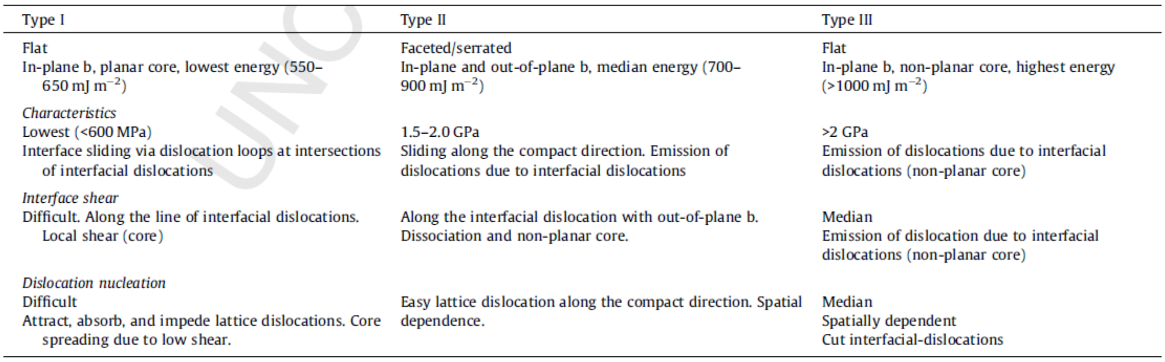

Type I	Type II	Type III
Flat	Faceted/serrated	Flat
In-plane b, planar core, lowest energy (550–650 mJ m^{-2})	In-plane and out-of-plane b, median energy (700–900 mJ m^{-2})	In-plane b, non-planar core, highest energy (>1000 mJ m^{-2})
Characteristics		
Lowest (<600 MPa)	1.5–2.0 GPa	>2 GPa
Interface sliding via dislocation loops at intersections of interfacial dislocations	Sliding along the compact direction. Emission of dislocations due to interfacial dislocations	Emission of dislocations due to interfacial dislocations (non-planar core)
Interface shear		
Difficult. Along the line of interfacial dislocations. Local shear (core)	Along the interfacial dislocation with out-of-plane b. Dissociation and non-planar core.	Median Emission of dislocation due to interfacial dislocations (non-planar core)
Dislocation nucleation		
Difficult Attract, absorb, and impede lattice dislocations. Core spreading due to low shear.	Easy lattice dislocation along the compact direction. Spatial dependence.	Median Spatially dependent Cut interfacial-dislocations

2.2.4 Bulk metallic glass and metallic glass nano composites

Bulk metallic glass (Bulk Metallic Glass, BMG) is a new functional and structural material which has attracted great interest from the materials science and engineering community over the last decade [156-159]. BMG is usually prepared by rapid cooling of alloy melts [158-161] and usually exhibits very high yield strength (GPa level) [162-165]. However, because of catastrophic development and merge process of the shear band after yielding, BMG can only very rarely have tensile ductility [163]. The structure of BMG is as disordered as ordinary glass, but has considerable medium-range-order (MRO) [166-168]. Recent atomistic simulations and experiments indicate that there are icosahedron close package structures (ICO) with fivefold symmetry within BMG, resulting in the appearance of MRO [168, 169]. The presence and fraction of ICO may account for the mechanical properties of BMG [170]. Ma *et al* found that BMG with higher ICO fraction has greater strength [168]. By adjusting the chemical composition of BMG, Poisson ratio, modulus and strength can be tuned. However, it is still very challenging to introduce tensile ductility to BMG by structural design.

The major plastic deformation mechanism of BMG is the formation and propagation of shear bands. Akin to the manipulation of dislocation within metals, the manipulation of shear bands via structural design may be able to introduce ductility to BMG and BMG based composites [163]. The formation of shear band has historically been interpreted according to the free volume model proposed by Spaepen [171, 172] and by shear transformation zones (STZ), which were first proposed by Argon [173]. Recently, the STZ model has been greatly developed due to MD simulations and is able to predict the strength of BMG [174-178]. In an elastic deformation region, deformation of BMG is homogeneously distributed, but with the consideration of thermal fluctuation and microstructure heterogeneity, STZs with shear strain concentration and activation of only a few tens of atoms nucleate within BMG [179]. With further loading, STZs grow into a mature shear band, resulting in a transition from homogeneous deformation to heterogeneous deformation. The rapid propagation of mature shear bands results in the failure of BMG. Even though the atomic structural details still remain unknown, STZ can still be considered as an elementary plastic deformation carrier, similar to the role of dislocation in crystal metals. The toughening of BMG can be achieved via controlling the nucleation and distribution of STZs, and suppressing the formation of shear bands [177, 180-185].

In particular, Ogata and Ju Li *et al* developed an aged-rejuvenation-glue-liquid (ARGL) model [175, 186] of shear bands in BMGs based on atomistic simulation results to predict the critical condition that corresponds to embryonic shear band (ESB) propagation. This model is illustrated in Fig. 2.7. To propagate an ESB, the far-field shear stress must exceed the quasi-steady-state glue traction of τ_{glue} of shear-alienated glass, represented in Zone III of Fig. 2.7, until the glass transition temperature is approached internally due to frictional heating, at which the ESB can mature as a runaway shear crack. Thus a critical incubation length l_{inc} is necessary for the propagation of an ESB, *e.g.* about 100 nm for Zr-based BMGs. If the sample size is below l_{inc}, mature shear bands cannot be formed in BMGs.

By employing the idea of the ARGL model, materialists should be able to suppress the formation and propagation of shear bands in BMGs by limiting STZs to a small volume. An example is the metallic glass nanowire: when its diameter is below l_{inc}, it exhibits good tensile ductility because no shear band can be formed during deformation before the STZ escapes from the free surface [180, 187, 188]. Another example is BMG with a very large fraction of crystal dendrites in which deformation of BMG is limited to a small volume confined by the interface between crystal and glass [184, 189-193]. Qiao et al [189, 193] proposed a multi-yielding mechanism for such materials to explain why they can exhibit considerable ductility. In the context of designing tough BMG composites, interfaces in these materials behave as a high barrier to limit the propagation of ESB. Thus these materials can deform via multiple ESB nucleation and other plastic events of crystal components.

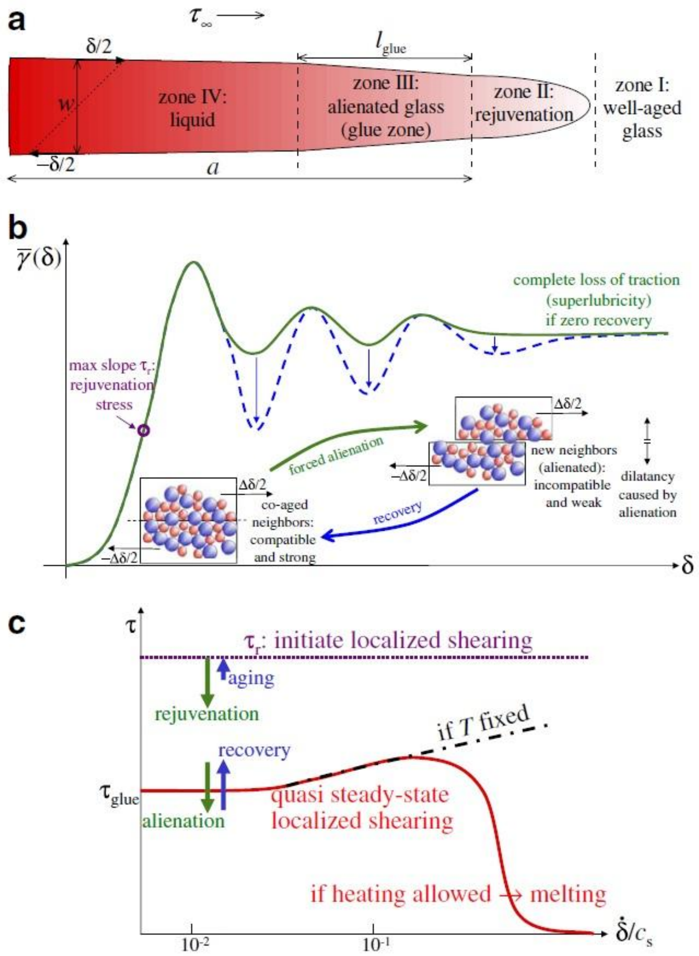

Figure 2.7. (a) Aged-rejuvenation-glue-liquid (ARGL) model of shear band in BMGs. The shading represents temperature. (b) GSF energy of a glass as a function of a sharp displacement discontinuity. The solid curve illustrates the behavior without any recovery process. The dashed curve shows that, as time increases, recovery occurs and the energy traps get deeper. (c) Shear traction of glass as a function of local sliding speed, evaluated at a fixed observation time. Reprinted from Ref [175].

The plastic deformation map for BMG-based composites may involve more than consideration of shear bands. The interface between glass or amorphous constituents and crystal constituents should be emphasized. Wang et al [194] found that amorphous/crystalline nanolaminates exhibit ideal plasticity after yielding. In this context, amorphous structure can be thought of as identical to glass structure. The amorphous/crystal interface (ACI) is able to transmit the plastic deformation carried by dislocation in the crystal layer to the STZs in the amorphous layer [194]. Fig. 2.8 shows TEM observation and supporting MD simulation evidence for this mechanism. The transformation from dislocation to STZ is not like the dislocation transmission at the interface between crystals. Since STZ is directionless, the former requires rather low activation energy, leaves no accumulative strain on ACI, and, most importantly, occurs continually. However, more details of the ACI's role in plastic deformation are not clear. For example, the ACI has finite width and interfacial dislocation, and definitely affects the atomic structure of amorphous constituents [195]. How the change of atomic structure near the ACI and interfacial dislocation affect plastic deformation remains unknown.

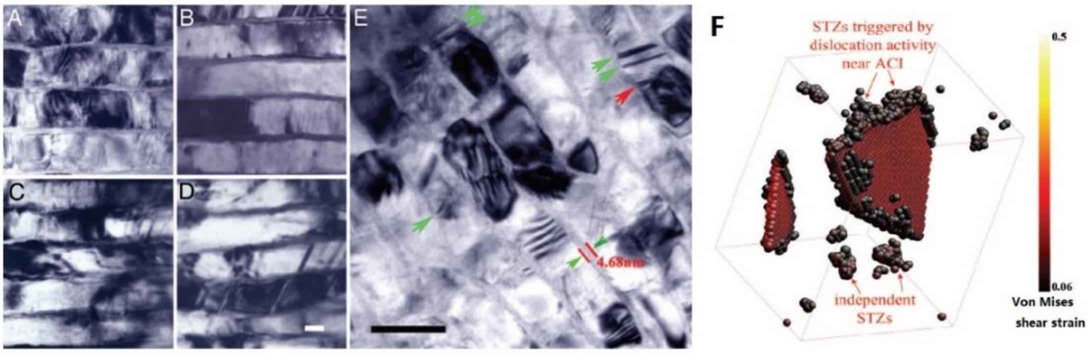

Figure 2.8. Deformation microstructures. (A-D) Sequential TEM images of the 5 nm/35 nm $Cu_{\approx 3}Zr$/Cu nanolaminates at tensile strain of 0%(A), 2%(B), 7%(C), and 10%(D). TEM images show that ACIs may have become dislocation, partial dislocation and deformation twin nucleation sites. (Scale bars: A-D, 20 nm; E, 50nm). Dislocation-trigger-STZ mechanism at ACI is shown in (F), obtained by MD simulations. Reprinted from Ref [194].

2.2.5 Ideas from biological structural materials

In the context of materials design, nature usually provides very good examples [196-198]. Skeletons, teeth, shells etc. are made of soft organic substances and hard inorganic crystal minerals. Most surprisingly, these structural biomaterials of great toughness usually have perfect hierarchical structures [197-202]. The six-level hierarchical structure of nacre is shown in Fig. 2.9 [201]. A “brick & mortar” structure is revealed in Fig. 2.9(f). The “brick” refers to polygonal tablets made of aragonite crystals with a thickness of approximately 500 nm. The “mortar” refers to organic material located inside and between these tablets. At smaller scale, the tablets consist of the assembly of nanograins with an average size of about 32 nm and are delimited by a fine three-dimensional network of organic material (as shown in Fig. 2.9(g)). At larger than micrometer scale, the tablets are assembled and linked by soft organic polymers. In bone, which also has “brick & mortar” structure [199, 203], the mineral crystals (hydroxyapatite) are confirmed to have nanoscale size; furthermore, the thickness is typically on the order of 1 nm and the length approximately 60~100 nm.

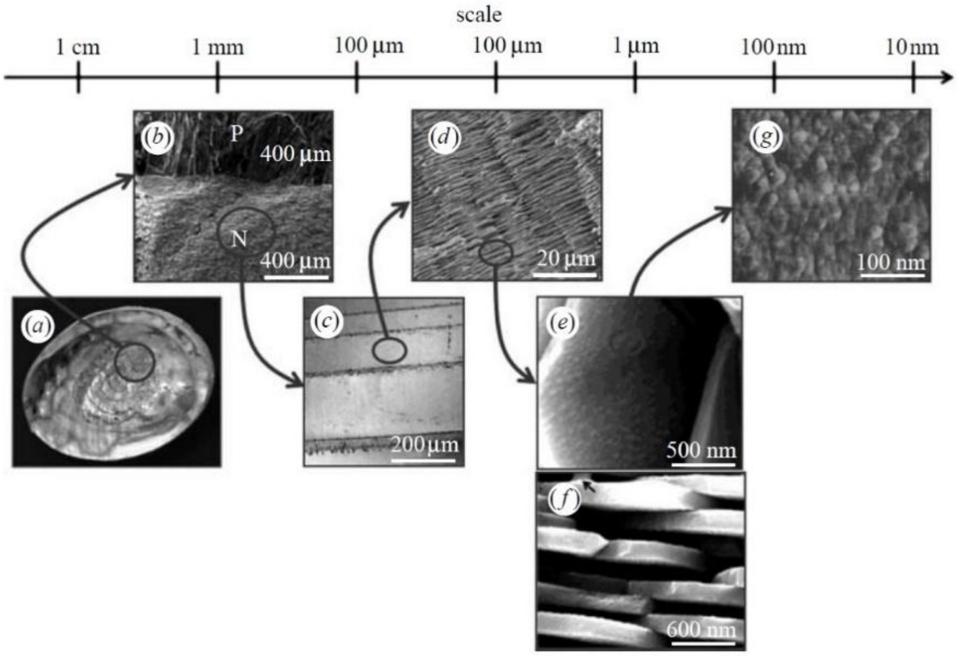

Figure 2.9. Hierarchical organization in nacre showing at least six structural levels.

Reprinted from Ref [201].

These structural biomaterials with "brick & mortar" structure usually have an optimum combination of mechanical properties. For example, the tensile strength of compact bone along the longitudinal direction is higher than that of either hydroxyapatite (100 MPa) or collagen (~50 MPa), demonstrating the synergistic effect of successful composites [199, 203-206]. At the same time, the tensile strength along the longitudinal direction is three times higher than it is in the circumferential direction. The fracture toughness of bone is also higher than any of its components [206]. Another wonderful case is the exoskeleton of the American lobster [207]. A light optical micrograph of a cross section through the thickness of the exoskeleton is shown in Fig. 2.10. It should be noted that lobster exoskeleton has Bouligand hierarchical structure, made of chitin and protein. The two layers, exocutile and endocuticle, have different stacking density. The outer layer, the exocutile, has a very compact twisted plywood-like structure and high stiffness, in the range of 8.5-9.5 GPa. The endocuticle shows a much coarser twisted plywood-like structure and a low stiffness of 3-4.5 GPa. Within the exocutile, a gradual increase in stacking density, from 100 micrometers depth to 300 micrometers depth, has been identified, resulting in the same trend of an increase in stiffness. Across the interface between exocutile and endocuticle, both abruptly change, resulting in a drop in stiffness. This gradient structure of the skeleton provides great resistance to occasional impacts from the environment of lobsters.

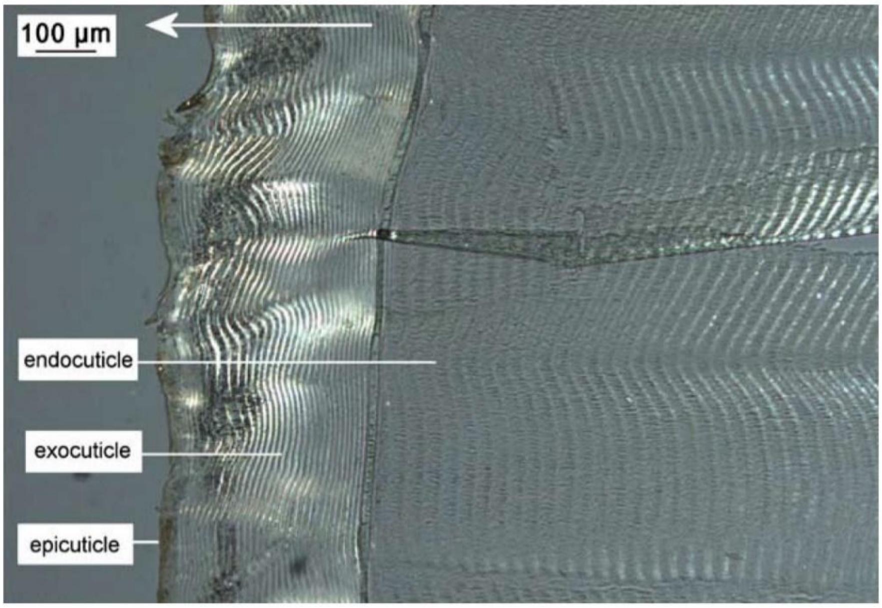

Figure 2.10. Light optical micrograph of a cross section through the thickness of the skeleton of the American lobster. Reprinted from Ref [207].

Some key findings in structural biomaterials in the last decade include the identification of the principal deformation mechanisms [197, 206, 208-212]. Some of these mechanisms are related to interfaces. Gupta H. S. *et al* used synchrotron X-ray scattering to measure deformation distribution in bone at micrometer scale [208, 210]. The tensile strain of bone comes from two contributions: tensile stretching of the mineralized collagen fibrils, and a predominantly shear deformation of the interfibrillar matrix. It should be noted that the mineralized collagen fibrils are made up by mineral tablets at nanoscale, and proteins. The interfibrillar matrix is also mineralized and contains a small fraction of minerals. After the yielding, the strain of mineralized fibrils is not relaxed. A possible mechanism is proposed by Gupta et al that the stick/slip interfibrillar matrix flow past the mineralized fibrils can transmit a constant flow shear stress between fibrils [208], maintaining a constant strain in the fibrils when local shear stress exceeds the critical interfacial shear strength between fibril and matrix. At smaller scale in the mineralized fibrils, the interface between mineral crystal and organic material may have nano-asperities which can create frictional resistance to interfacial sliding, contributing to toughening. Gao et al. found that the fracture strength of mineral tablets may exceed ideal Griffith strength if the size of tablet is at nanoscale and the fracture strength of structural biomaterials mostly depends on the interfacial strength [197]. The identification of interface-mediated deformation mechanisms in hierarchical biomaterials may provide fruitful insights for designing materials.

Most importantly, biomaterials are natural products of the evolution of life since its beginning on our planet. Meyers [205] has presented seven key features of biomaterials: 1. self-assembly, 2. multi-functionality, 3. hierarchy, 4. hydration, 5. mild synthesis conditions, 6. evolution and environmental constraints, and 7. self-healing. A synthesis of materials with these features has been a long-term goal for the materials research community for centuries. The study of biomaterials has provided at least two lessons for us: 1. it may be possible to synthesize structural materials by mimicking natural DNA assembly processes or using organic macromolecular as template in future

[213-218]; and 2. the structure and deformation mechanisms of biomaterials have greatly inspired scientists even though such studies are still at the beginning [198, 207, 219, 220].

2.3 Summary and problems

In conclusion, several typical structural nanomaterials and their relative interfacial plasticity are reviewed in this chapter. It can be concluded that an interface strengthens nanomaterials via hindering propagation of dislocation and nucleating dislocation. The first is an expansion of the traditional Hall-Petch relationship. The second follows in the realm of both thermodynamics and mechanics. A large fraction of interfacial atoms transforms plasticity from slip-dominated to nucleation-dominated. These examples also show that interfacial plasticity is not only able to strengthen nanomaterials but also helps maintain considerable ductility. Key reasons for the considerable ductility of nanomaterials of high strength include the ability of interfaces to allow the transmission of plasticity and the avoidance of deformation concentration. Investigation of interfacial plasticity by atomistic simulations will help evaluate the ability of interfaces to strengthen nanomaterials without great loss of ductility.

Physically, plasticity events in materials are collective motions of groups of atoms and make elementary contribution to overall deformation. The microstructure evolution of such events is along the minimum energy path (MEP) on the potential energy surfaces (PES). The fingerprint of plastic events and the activation volume and energy of such events are associated with local atomic structure and relative PES. In conventional metallic materials, the most popular plastic events are dislocation climb, dislocation slip, and deformation twinning, all being associated with pre-existing defects and requiring large activation volume (~1000 atomic volume). Investigation of such events is beyond the capability of atomistic simulations. But in nanomaterials, plastic events are always associated with collective motion of only tens of atoms, requiring small activation volume (~ several atomic volume). In this chapter we have reviewed several typical interfacial plastic deformation mechanisms, including interface sliding and dislocation nucleation. However, theoretical connections among atomic structure of interface, interfacial plasticity and relative mechanical properties have not been established.

Several challenges will be encountered in discussing interfacial plasticity. The first is that it is quite hard to describe interface atomic structure three-dimensionally – this has not been reviewed in this chapter but can be found elsewhere. There is extensive evidence showing that interfacial plasticity in nanomaterials strongly depends on atomic structure. The second is that current atomistic simulations are not able to predict mechanical response of interface under experimental conditions. Even though some progress has been made in modeling plasticity under low strain rates, this is still far from simulating real structure under real conditions. The third is that even though interfacial plasticity in nanomaterials is always associated with group activation of rather few atoms, the complexity of PES (several hundred freedoms) still makes direct modeling from atomistic simulation results and further comparison with experimental results quite challenging. Thus the investigation of interfacial plasticity still remains quite preliminary, and there is still plenty of room for the investigation of interfacial plasticity in nanomaterials.

Reference

[1] Ogata S, Li J, Hirosaki N, Shibutani Y, Yip S. Ideal shear strain of metals and ceramics. Physical Review B. 2004;70.

[2] Ogata S, Li J, Yip S. Ideal pure shear strength of aluminum and copper. Science.

2002;298:807-11.

[3] Ogata S, Li J, Yip S. Energy landscape of deformation twinning in bcc and fcc metals. Physical Review B. 2005;71.

[4] Van Vliet KJ, Li J, Zhu T, Yip S, Suresh S. Quantifying the early stages of plasticity through nanoscale experiments and simulations. PHYsical Review B. 2003;67:104105.

[5] Li J, Van Vliet KJ, Zhu T, Yip S, Suresh S. Atomistic mechanisms governing elastic limit and incipient plasticity in crystals. Nature. 2002;418:307-10.

[6] Li J. The mechanics and physics of defect nucleation (vol 32, pg 151, 2007). MRS Bull. 2007;32:462-.

[7] Hirth JP, Lothe J. Theory of dislocations. 1982.

[8] McLean D. Mechanical properties of metals: RE Krieger Publishing Company; 1977.

[9] Reed-Hill RE, Abbaschian R. Physical metallurgy principles. 1973.

[10] Bravo-Leon A, Morikawa Y, Kawahara M, Mayo MJ. Fracture toughness of nanocrystalline tetragonal zirconia with low yttria content. Acta Mater. 2002;50:4555-62.

[11] Zhu T, Li J. Ultra-strength materials. Prog Mater Sci. 2010;55:710-57.

[12] Zhu T, Li J, Ogata S, Yip S. Mechanics of Ultra-Strength Materials. MRS Bull. 2009;34:167-72.

[13] Deng C, Sansoz F. Enabling Ultrahigh Plastic Flow and Work Hardening in Twinned Gold Nanowires. Nano Lett. 2009;9:1517-22.

[14] Tian Y, Xu B, Yu D, Ma Y, Wang Y, Jiang Y, et al. Ultrahard nanotwinned cubic boron nitride. Nature. 2013;493:385-8.

[15] G R, K H, DS G, R M, O K, CA V. Ultrahigh strength single crystalline nanowhiskers grown by physical vapor deposition. Nano Lett. 2009;9:3048.

[16] Yu Q, Qi L, Mishra RK, Li J, Minor AM. Reducing deformation anisotropy to achieve ultrahigh strength and ductility in Mg at the nanoscale. Proceedings of the National Academy of Sciences. 2013;110:13289-93.

[17] Bringa EM, Caro A, Wang Y, Victoria M, McNaney JM, Remington BA, et al. Ultrahigh Strength in Nanocrystalline Materials Under Shock Loading. Science. 2005;309:1838-41.

[18] Lu L, Shen YF, Chen XH, Qian LH, Lu K. Ultrahigh strength and high electrical conductivity in copper. Science. 2004;304:422-6.

[19] Fang TH, Li WL, Tao NR, Lu K. Revealing Extraordinary Intrinsic Tensile Plasticity in Gradient Nano-Grained Copper. Science. 2011;331:1587-90.

[20] Maass R, Van Petegem S, Ma DC, Zimmermann J, Grolimund D, Roters F, et al. Smaller is stronger: The effect of strain hardening. Acta Mater. 2009;57:5996-6005.

[21] Ovid’ko I, Sheinerman A. Grain size effect on crack blunting in nanocrystalline materials.

Scripta Mater. 2009;60:627-30.

[22] Wang Y, Chen M, Zhou F, Ma E. High tensile ductility in a nanostructured metal. Nature. 2002;419:912-5.

[23] MD U, DM D, JN F, WD N. Sample dimensions influence strength and crystal plasticity. Science. 2004;305:986.

[24] Kuzmin OV, Pei YT, Chen CQ, De Hosson JTM. Intrinsic and extrinsic size effects in the deformation of metallic glass nanopillars. Acta Mater. 2012;60:889-98.

[25] Greer JR, De Hosson JTM. Plasticity in small-sized metallic systems: Intrinsic versus extrinsic size effect. Prog Mater Sci. 2011;56:654-724.

[26] Mayo M, Hague D, Chen D-J. Processing nanocrystalline ceramics for applications in superplasticity. Materials Science and Engineering: A. 1993;166:145-59.

[27] Kuntz JD, Zhan G-D, Mukherjee AK. Nanocrystalline-matrix ceramic composites for improved fracture toughness. MRS Bull. 2004;29:22-7.

[28] Voevodin A, Prasad S, Zabinski J. Nanocrystalline carbide/amorphous carbon composites. J Appl Phys. 1997;82:855-8.

[29] Fleck NA, Hutchinson JW. A PHENOMENOLOGICAL THEORY FOR STRAIN GRADIENT EFFECTS IN PLASTICITY. Journal of the Mechanics and Physics of Solids. 1993;41:1825-57.

[30] Fleck NA, Muller GM, Ashby MF, Hutchinson JW. STRAIN GRADIENT PLASTICITY - THEORY AND EXPERIMENT. Acta Metallurgica Et Materialia. 1994;42:475-87.

[31] Nix WD, Gao HJ. Indentation size effects in crystalline materials: A law for strain gradient plasticity. Journal of the Mechanics and Physics of Solids. 1998;46:411-25.

[32] Gao H, Huang Y, Nix WD, Hutchinson JW. Mechanism-based strain gradient plasticity - I. Theory. Journal of the Mechanics and Physics of Solids. 1999;47:1239-63.

[33] Huang Y, Gao H, Nix WD, Hutchinson JW. Mechanism-based strain gradient plasticity - II. Analysis. Journal of the Mechanics and Physics of Solids. 2000;48:99-128.

[34] Qiu X, Huang Y, Wei Y, Gao H, Hwang KC. The flow theory of mechanism-based strain gradient plasticity. Mech Mater. 2003;35:245-58.

[35] J. Luscher D, A. Bronkhorst C, N. Alleman C. A Model for finite-deformation nonlinear thermomechanical response of single crystal copper under shock conditions. Journal of the Mechanics and Physics of Solids. 2013;61:1877-94.

[36] Yoshiie T, Ito T, Iwase H, Kaneko Y, Kawai M, Kishida I, et al. Multi-scale modeling of irradiation effects in spallation neutron source materials. Nuclear Instruments & Methods in Physics Research Section B-Beam Interactions with Materials and Atoms. 2011;269:1740-3.

[37] Roters F, Eisenlohr P, Hantcherli L, Tjahjanto DD, Bieler TR, Raabe D. Overview of

constitutive laws, kinematics, homogenization and multiscale methods in crystal plasticity finite-element modeling: Theory, experiments, applications. Acta Mater. 2010;58:1152-211.

[38] Meyers MA, Mishra A, Benson DJ. Mechanical properties of nanocrystalline materials. Prog Mater Sci. 2006;51:427-556.

[39] Chen MW, Ma E, Hemker KJ, Sheng HW, Wang YM, Cheng XM. Deformation twinning in nanocrystalline aluminum. Science. 2003;300:1275-7.

[40] Hao S, Cui L, Jiang D, Han X, Ren Y, Jiang J, et al. A Transforming Metal Nanocomposite with Large Elastic Strain, Low Modulus, and High Strength. Science. 2013;339:1191-4.

[41] Ovid'ko IA. Materials science - Deformation of nanostructures. Science. 2002;295:2386-.

[42] Shan Z, Stach EA, Wiezorek JMK, Knapp JA, Follstaedt DM, Mao SX. Grain Boundary-Mediated Plasticity in Nanocrystalline Nickel. Science. 2004;305:654-7.

[43] Shan Z, Stach EA, Wiezorek JMK, Knapp JA, Follstaedt DM, Mao SX. Response to Comment on "Grain Boundary-Mediated Plasticity in Nanocrystalline Nickel". Science. 2005;308:356.

[44] Szlufarska I, Nakano A, Vashishta P. A Crossover in the Mechanical Response of Nanocrystalline Ceramics. Science. 2005;309:911-4.

[45] Van Swygenhoven H. Polycrystalline materials - Grain boundaries and dislocations. Science. 2002;296:66-7.

[46] YH L, G W, RJ W, DQ Z, MX P, WH W. Super plastic bulk metallic glasses at room temperature. Science. 2007;315:1385.

[47] Van Swygenhoven H, Derlet PM, Fr 鴎 eth AG. Nucleation and propagation of dislocations in nanocrystalline fcc metals. Acta Mater. 2006;54:1975-83.

[48] Wu ZX, Zhang YW, Srolovitz DJ. Dislocation-twin interaction mechanisms for ultrahigh strength and ductility in nanotwinned metals. Acta Mater. 2009;57:4508-18.

[49] Lu K, Lu L, Suresh S. Strengthening Materials by Engineering Coherent Internal Boundaries at the Nanoscale. Science. 2009;324:349-52.

[50] Lu L, Chen X, Huang X, Lu K. Revealing the Maximum Strength in Nanotwinned Copper. Science. 2009;323:607-10.

[51] Lu L, Sui ML, Lu K. Superplastic extensibility of nanocrystalline copper at room temperature. Science. 2000;287:1463-6.

[52] Mayo M. Nanocrystalline ceramics for structural applications: processing and properties. Nanostruct Mater: Springer; 1998. p. 361-85.

[53] Evans A, Fuller E. Crack propagation in ceramic materials under cyclic loading conditions. Metallurgical transactions. 1974;5:27-33.

[54] Taylor GI. The mechanism of plastic deformation of crystals. Part I. Theoretical. Proceedings of the Royal Society of London Series A, Containing Papers of a Mathematical and Physical Character. 1934:362-87.

[55] Taylor G. The mechanism of plastic deformation of crystals. Part II. Comparison with observations. Proceedings of the Royal Society of London Series A, Containing Papers of a Mathematical and Physical Character. 1934:388-404.

[56] Campbell J, Simmons JA, Dorn JE. On the dynamic behavior of a Frank-Read Source. Journal of Applied Mechanics. 1961;28:447-53.

[57] Meyers MA, Vohringer O, Lubarda VA. The onset of twinning in metals: A constitutive description. Acta Mater. 2001;49:4025-39.

[58] Christian JW, Mahajan S. DEFORMATION TWINNING. Prog Mater Sci. 1995;39:1-157.

[59] Hartley K, Duffy J, Hawley R. Measurement of the temperature profile during shear band formation in steels deforming at high strain rates. Journal of the Mechanics and Physics of Solids. 1987;35:283-301.

[60] Clifton R, Duffy J, Hartley K, Shawki T. On critical conditions for shear band formation at high strain rates. Scripta Metallurgica. 1984;18:443-8.

[61] Dillamore I, Roberts J, Bush A. Occurrence of shear bands in heavily rolled cubic metals. Metal Science. 1979;13:73-7.

[62] Kraft O, Gruber PA, Mönig R, Weygand D. Plasticity in Confined Dimensions. Annual Review of Materials Research. 2010;40:293-317.

[63] HD E, M P, S B, KW S. Discrete dislocation dynamics simulations to interpret plasticity size and surface effects in freestanding FCC thin films. Int J Plast. 2006;22:2091.

[64] HD E, BC P, B P. Plasticity size effects in free-standing submicron polycrystalline FCC films subjected to pure tension. J Mech Phys Solids. 2004;52:667.

[65] VS D, A N, E VDG. Plasticity size effects in tension and compression of single crystals. J Mech Phys Solids. 2005;53:2661.

[66] Weinberger CR, Cai W. Plasticity of metal nanowires. J Mater Chem. 2012;22:3277-92.

[67] Van Petegem S, Zimmermann J, Van Swygenhoven H. Microstructure and deformation mechanisms in nanocrystalline Ni–Fe. Part II. In situ testing during X-ray diffraction. Acta Mater. 2013;61:5846-56.

[68] Kumar KS, Van Swygenhoven H, Suresh S. Mechanical behavior of nanocrystalline metals and alloys. Acta Mater. 2003;51:5743-74.

[69] Nix WD. Mechanical properties of thin films. Metall Trans A. 1989;20:2217-45.

[70] Yamakov V, Wolf D, Phillpot SR, Mukherjee AK, Gleiter H. Deformation-mechanism

map for nanocrystalline metals by molecular-dynamics simulation. Nature Materials. 2004;3:43-7.

[71] Van Swygenhoven H, Derlet PM. Chapter 81 Atomistic Simulations of Dislocations in FCC Metallic Nanocrystalline Materials. In: John H, editor. Dislocations in Solids: Elsevier; 2008. p. 1-42.

[72] Chokshi A, Rosen A, Karch J, Gleiter H. On the validity of the Hall-Petch relationship in nanocrystalline materials. Scripta Metallurgica. 1989;23:1679-83.

[73] Hansen N. Hall–Petch relation and boundary strengthening. Scripta Mater. 2004;51:801-6.

[74] Carlton CE, Ferreira PJ. What is behind the inverse Hall-Petch effect in nanocrystalline materials? Acta Mater. 2007;55:3749-56.

[75] Padmanabhan KA, Dinda GP, Hahn H, Gleiter H. Inverse Hall–Petch effect and grain boundary sliding controlled flow in nanocrystalline materials. Materials Science and Engineering: A. 2007;452–453:462-8.

[76] Schäfer J, Albe K. Competing deformation mechanisms in nanocrystalline metals and alloys: Coupled motion versus grain boundary sliding. Acta Mater. 2012;60:6076-85.

[77] Vo NQ, Averback RS, Bellon P, Odunuga S, Caro A. Quantitative description of plastic deformation in nanocrystalline Cu: Dislocation glide versus grain boundary sliding. Physical Review B. 2008;77:134108.

[78] Bobylev SV, Morozov NF, Ovid’ko IA. Cooperative Grain Boundary Sliding and Migration Process in Nanocrystalline Solids. Phys Rev Lett. 2010;105:055504.

[79] Van Swygenhoven H, Derlet PM. Grain-boundary sliding in nanocrystalline fcc metals. Physical Review B. 2001;64:224105.

[80] Mohamed F, Chauhan M. Interpretation of the creep behavior of nanocrystalline Ni in terms of dislocation accommodated boundary sliding. Metall and Mat Trans A. 2006;37:3555-67.

[81] Sergueeva A, Mara N, Mukherjee A. Grain boundary sliding in nanomaterials at elevated temperatures. J Mater Sci. 2007;42:1433-8.

[82] Van Swygenhoven H, Weertman JR. Deformation in nanocrystalline metals. Mater Today. 2006;9:24-31.

[83] Ovid’ko I, Sheinerman A, Aifantis E. Stress-driven migration of grain boundaries and fracture processes in nanocrystalline ceramics and metals. Acta Mater. 2008;56:2718-27.

[84] Van Swygenhoven H, Derlet PM, Hasnaoui A. Atomic mechanism for dislocation emission from nanosized grain boundaries. PHYsical Review B. 2002;66:024101.

[85] Van Swygenhoven H, Derlet P. Atomistic simulations of dislocations in FCC metallic

nanocrystalline materials. Dislocations in solids. 2008;14:1-42.

[86] Li XY, Wei YJ, Lu L, Lu K, Gao HJ. Dislocation nucleation governed softening and maximum strength in nano-twinned metals. Nature. 2010;464:877-80.

[87] Yamakov V, Wolf D, Phillpot SR, Mukherjee AK, Gleiter H. Dislocation processes in the deformation of nanocrystalline aluminium by molecular-dynamics simulation. Nature Materials. 2002;1:45-8.

[88] Chen B, Lutker K, Raju SV, Yan J, Kanitpanyacharoen W, Lei J, et al. Texture of Nanocrystalline Nickel: Probing the Lower Size Limit of Dislocation Activity. Science. 2012;338:1448-51.

[89] Ovid'ko IA, Skiba NV. Enhanced dislocation emission from grain boundaries in nanocrystalline materials. Scripta Mater. 2012;67:13-6.

[90] Derlet PM, Gumbsch P, Hoagland R, Li J, McDowell DL, Van Swygenhoven H, et al. Atomistic Simulations of Dislocations in Confined Volumes. MRS Bull. 2009;34:184-9.

[91] Yamakov V, Wolf D, Phillpot SR, Gleiter H. Deformation twinning in nanocrystalline Al by molecular dynamics simulation. Acta Mater. 2002;50:5005-20.

[92] Wu XL, Narayan J, Zhu YT. Deformation twin formed by self-thickening, cross-slip mechanism in nanocrystalline Ni. Appl Phys Lett. 2008;93:-.

[93] Chen K, Shi S, Lu J. Deformation twin induced by multi-mode deformation in nanocrystalline copper. Philos Mag Lett.

[94] Liao XZ, Zhao YH, Srinivasan SG, Zhu YT, Valiev RZ, Gunderov DV. Deformation twinning in nanocrystalline copper at room temperature and low strain rate. Appl Phys Lett. 2004;84:592-4.

[95] Liao XZ, Zhou F, Lavernia EJ, He DW, Zhu YT. Deformation twins in nanocrystalline Al. Appl Phys Lett. 2003;83:5062-4.

[96] Froseth AG, Derlet PM, Van Swygenhoven H. Twinning in nanocrystalline fcc metals. Adv Eng Mater. 2005;7:16-20.

[97] Zhu YT, Narayan J, Hirth JP, Mahajan S, Wu XL, Liao XZ. Formation of single and multiple deformation twins in nanocrystalline fcc metals. Acta Mater. 2009;57:3763-70.

[98] Han WZ, Wu SD, Li SX, Zhang ZF. Origin of deformation twinning from grain boundary in copper. Appl Phys Lett. 2008;92:3.

[99] Wang J, Huang HC. Shockley partial dislocations to twin: Another formation mechanism and generic driving force. Appl Phys Lett. 2004;85:5983-5.

[100] Zhu YT, Liao XZ, Srinivasan SG, Zhao YH, Baskes MI, Zhou F, et al. Nucleation and growth of deformation twins in nanocrystalline aluminum. Appl Phys Lett. 2004;85:5049-51.

[101] X. L. Wu XZL, S. G. Srinivasan, F. Zhou, E. J. Lavernia, R. Z. Valiev, Y. T. Zhu. New

Deformation Twinning Mechanism Generates Zero Macroscopic Strain in Nanocrystalline Metals. Phys Rev Lett. 2008;100:095701.

[102] Nieh T-G, Wadsworth J, Sherby OD. Superplasticity in metals and ceramics: Cambridge university press; 2005.

[103] Lüthy H, White RA, Sherby OD. Grain boundary sliding and deformation mechanism maps. Materials Science and Engineering. 1979;39:211-6.

[104] Klinger L, Rabkin E. Thermal stability and creep of polycrystalline nanowires. Acta Mater. 2006;54:305-11.

[105] Yamakov V, Wolf D, Phillpot SR, Gleiter H. Grain-boundary diffusion creep in nanocrystalline palladium by molecular-dynamics simulation. Acta Mater. 2002;50:61-73.

[106] Choi I-C, Kim Y-J, Seok M-Y, Yoo B-G, Kim J-Y, Wang Y, et al. Nanoscale room temperature creep of nanocrystalline nickel pillars at low stresses. Int J Plast. 2012.

[107] AG F, PM D, H VS. Dislocations emitted from nanocrystalline grain boundaries: nucleation and splitting distance. Acta Mater. 2004;52:5863.

[108] H VS, PM D, AG F. Nucleation and propagation of dislocations in nanocrystalline fcc metals. Acta Mater. 2006;54:1975.

[109] V Y, D W, SR P, AK M, H G. Dislocation processes in the deformation of nanocrystalline aluminum by molecular-dynamics simulation. Nat Mater. 2002;1:45.

[110] Liao XZ, Zhou F, Lavernia EJ, Srinivasan SG, Baskes MI, He DW, et al. Deformation mechanism in nanocrystalline Al: Partial dislocation slip. Appl Phys Lett. 2003;83:632-4.

[111] Wu XL, Zhu YT. Partial-dislocation-mediated processes in nanocrystalline Ni with nonequilibrium grain boundaries. Appl Phys Lett. 2006;89:3.

[112] Wang L, Han X, Liu P, Yue Y, Zhang Z, Ma E. <i>In Situ</i> Observation of Dislocation Behavior in Nanometer Grains. Phys Rev Lett. 2010;105:135501.

[113] Asaro RJ, Suresh S. Mechanistic models for the activation volume and rate sensitivity in metals with nanocrystalline grains and nano-scale twins. Acta Mater. 2005;53:3369-82.

[114] Wei Q, Cheng S, Ramesh KT, Ma E. Effect of nanocrystalline and ultrafine grain sizes on the strain rate sensitivity and activation volume: fcc versus bcc metals. Materials Science and Engineering a-Structural Materials Properties Microstructure and Processing. 2004;381:71-9.

[115] Zhu T, Li J, Samanta A, Kim HG, Suresh S. Interfacial plasticity governs strain rate sensitivity and ductility in nanostructured metals. Proceedings of the National Academy of Sciences. 2007;104:3031-6.

[116] H. VAN SWYGENHOVEN PMDAAGF. Stacking fault energies and slip in nanocrystalline metals. Nat Mat. 2004;3:399.

[117] Zimmerman JA, Gao HJ, Abraham FF. Generalized stacking fault energies for embedded atom FCC metals. Modell Simul Mater Sci Eng. 2000;8:103-15.

[118] B. Li BYC, K. T. Ramesh, E. Ma. A nucleation mechanism of deformation twins in pure aluminum. Acta Mater. 2009;57:4500.

[119] Zhu YT, Liao XZ. Formation mechanism of fivefold deformation twins in nanocrystalline face-centered-cubic metals. Appl Phys Lett. 2005;86:-.

[120] Cao AJ, Wei YG. Formation of fivefold deformation twins in nanocrystalline face-centered-cubic copper based on molecular dynamics simulations. Appl Phys Lett. 2006;89:3.

[121] Y. T. Zhu XLW, X. Z. Liao, J. Narayan, S. N. Mathaudhu, and L. J. Kecskés. Twinning partial multiplication at grain boundary in nanocrystalline fcc metals. Appl Phys Lett. 2009;95:031909.

[122] Wan L, Wang S. Shear response of the Σ9 ⟨110⟩ {221} symmetric tilt grain boundary in fcc metals studied by atomistic simulation methods. Physical Review B. 2010;82:214112.

[123] Cerreta E, Escobedo JP, Perez-Bergquist A, Koller DD, Trujillo CP, Gray III GT, et al. Early stage dynamic damage and the role of grain boundary type. Acta Mater. 2012;66:638-41.

[124] Vo NQ, Schäfer J, Averback RS, Albe K, Ashkenazy Y, Bellon P. Reaching theoretical strengths in nanocrystalline Cu by grain boundary doping. Scripta Mater. 2011;65:660-3.

[125] Lee H, Tomar V. Understanding the influence of grain boundary thickness variation on the mechanical strength of a nickel-doped tungsten grain boundary. Int J Plast. 2014;53:135-47.

[126] Smith L, Farkas D. Non-planar grain boundary structures in fcc metals and their role in nano-scale deformation mechanisms. Philosophical Magazine. 2013;94:152-73.

[127] Özerinç S, Tai K, Vo NQ, Bellon P, Averback RS, King WP. Grain boundary doping strengthens nanocrystalline copper alloys. Scripta Mater. 2012;67:720-3.

[128] Tschopp MA, Spearot D, McDowell DL. Influence of Grain Boundary Structure on Dislocation Nucleation in FCC Metals. In: Hirth J, editor. Dislocation in Solids: Elsevier B. V.

[129] Fensin SJ, Escobedo-Diaz JP, Brandl C, Cerreta EK, Gray Iii GT, Germann TC, et al. Effect of loading direction on grain boundary failure under shock loading. Acta Mater. 2014;64:113-22.

[130] Jinyu GUO KW, Lei LU. tensile properties of Cu with Deformation Twins Induced by SMAT. Journal of Materials Science & Technology. 2006;22(6):789.

[131] Blonde R, Chan H-L, Allain-Bonasso N, Bolle B, Grosdidier T, Lu J. Evolution of texture and microstructure in pulsed electro-deposited Cu treated by Surface Mechanical

Attrition Treatment (SMAT). J Alloys Compd. 2010;504:S410-S3.

[132] Lu K, Lu J. Nanostructured surface layer on metallic materials induced by surface mechanical attrition treatment. Materials Science and Engineering: A. 2004;375–377:38-45.

[133] Wang ZB, Tao NR, Tong WP, Lu J, Lu K. Diffusion of chromium in nanocrystalline iron produced by means of surface mechanical attrition treatment. Acta Mater. 2003;51:4319-29.

[134] Liu XC, Zhang HW, Lu K. Strain-Induced Ultrahard and Ultrastable Nanolaminated Structure in Nickel. Science. 2013;342:337-40.

[135] Wang J, Zhou C, Beyerlein I, Shao S. Modeling Interface-Dominated Mechanical Behavior of Nanolayered Crystalline Composites. JOM. 2014;66:102-13.

[136] Shao S, Medyanik SN. Interaction of dislocations with incoherent interfaces in nanoscale FCC–BCC metallic bi-layers. Modell Simul Mater Sci Eng. 2010;18:055010.

[137] Mishin Y, Asta M, Li J. Atomistic modeling of interfaces and their impact on microstructure and properties. Acta Mater. 2010;58:1117-51.

[138] Wang J, Misra A. An overview of interface-dominated deformation mechanisms in metallic multilayers. Curr Opin Solid State Mater Sci. 2011;15:20-8.

[139] Misra A, Kung H, Embury JD. Preface to the viewpoint set on: deformation and stability of nanoscale metallic multilayers. Scripta Mater. 2004;50:707-10.

[140] Wang J, Hoagland RG, Misra A. Mechanics of nanoscale metallic multilayers: From atomic-scale to micro-scale. Scripta Mater. 2009;60:1067-72.

[141] Wei Y. Scaling of maximum strength with grain size in nanotwinned fcc metals. PHYsical Review B. 2011;83:132104.

[142] Li L, Ghoniem NM. Twin-size effects on the deformation of nanotwinned copper. Physical Review B. 2009;79:075444.

[143] Misra A, Hoagland RG. Plastic flow stability of metallic nanolaminate composites. J Mater Sci. 2007;42:1765-71.

[144] Anderson PM, Foecke T, Hazzledine PM. Dislocation-Based Deformation Mechanisms in Metallic Nanolaminates. MRS Bull. 1999;24:27-33.

[145] Zheng S, Wang J, Carpenter J, Mook W, Dickerson P, Mara N, et al. Plastic instability mechanisms in bimetallic nanolayered composites. Acta Mater. 2014;79:282-91.

[146] Carpenter JS, McCabe RJ, Zheng SJ, Wynn TA, Mara NA, Beyerlein IJ. Processing parameter influence on texture and microstructural evolution in Cu-Nb multilayer composites fabricated via accumulative roll bonding. Metall and Mat Trans A. 2014;45:2192-208.

[147] Wang J, Kang K, Zhang R, Zheng S, Beyerlein I, Mara N. Structure and property of interfaces in ARB Cu/Nb laminated composites. JOM. 2012;64:1208-17.

[148] Shahabi HS, Manesh HD. Micro-structural evaluation of Cu/Nb nano-layered composites produced by repeated press and rolling process. J Alloys Compd. 2009;482:526-34.

[149] Carpenter J, Vogel S, LeDonne J, Hammon D, Beyerlein I, Mara N. Bulk texture evolution of Cu–Nb nanolamellar composites during accumulative roll bonding. Acta Mater. 2012;60:1576-86.

[150] Zhou J, Averback R, Bellon P. Stability and amorphization of Cu–Nb interfaces during severe plastic deformation: Molecular dynamics simulations of simple shear. Acta Mater. 2014;73:116-27.

[151] Alizadeh M, Samiei M. Fabrication of nanostructured Al/Cu/Mn metallic multilayer composites by accumulative roll bonding process and investigation of their mechanical properties. Materials & Design. 2014;56:680-4.

[152] Li L, Nagai K, Yin F. Progress in cold roll bonding of metals. Science and Technology of advanced materials. 2008;9:023001.

[153] Zhang RF, German TC, Wang J, Liu X-Y, Beyerlein IJ. Role of interface structure on the plastic response of Cu/Nb nanolaminates under shock compression: Non-equilibrium molecular dynamics simulations. Scripta Mater. 2013;68:114-7.

[154] Zhang RF, Germann TC, Liu XY, Wang J, Beyerlein IJ. Layer size effect on the shock compression behavior of fcc–bcc nanolaminates. Acta Mater. 2014;79:74-83.

[155] Han WZ, Cerreta EK, Mara NA, Beyerlein IJ, Carpenter JS, Zheng SJ, et al. Deformation and failure of shocked bulk Cu-Nb nanolaminates. Acta Mater. 2014;63:150-61.

[156] Wang WH. The elastic properties, elastic models and elastic perspectives of metallic glasses. Prog Mater Sci. 2012;57:487-656.

[157] HS C. Glassy metals. Rep Prog Phys. 1980;43:353.

[158] AL G. Metallic glasses. Science. 1995;267:1947.

[159] FC F. Supercooling of liquids. Proc R Soc London Ser A. 1952;215:43.

[160] HS C. Thermodynamic considerations on the formation and stability of metallic glasses. Acta Metall. 1974;22:1505.

[161] Debenedetti PG, Stillinger FH. Supercooled liquids and the glass transition. Nature. 2001;410:259-67.

[162] JJ G. Mechanical behavior of metallic glasses. J Appl Phys. 1975;46:1625.

[163] Greer AL, Cheng YQ, Ma E. Shear bands in metallic glasses. Materials Science and Engineering: R: Reports. 2013;74:71-132.

[164] C M, A L. Universal breakdown of elasticity at the onset of material failure. Phys Rev Lett. 2004;93:195501.

[165] Johnson WL, Samwer K. A Universal Criterion for Plastic Yielding of Metallic Glasses with a (T/T_{g})^{2/3} Temperature Dependence. Phys Rev Lett. 2005;95:195501.

[166] DB M. A structural model for metallic glasses. Nat Mater. 2004;3:697.

[167] Wang G, Mattern N, Pauly S, Bednarčik J, Eckert J. Atomic structure evolution in bulk metallic glass under compressive stress. Appl Phys Lett. 2009;95:-.

[168] Cheng YQ, Ma E, Sheng HW. Atomic Level Structure in Multicomponent Bulk Metallic Glass. Phys Rev Lett. 2009;102:245501.

[169] Cheng YQ, Ma E. Atomic-level structure and structure–property relationship in metallic glasses. Prog Mater Sci. 2011;56:379-473.

[170] Peng HL, Li MZ, Wang WH. Structural Signature of Plastic Deformation in Metallic Glasses. Phys Rev Lett. 2011;106:135503.

[171] F S. A microscopic mechanism for steady state inhomogeneous flow in metallic glasses. Acta Metall. 1977;25:407.

[172] Spaepen F. Homogeneous flow of metallic glasses: A free volume perspective. Scripta Mater. 2006;54:363-7.

[173] AS A. Plastic deformation in metallic glasses. Acta Metall. 1979;27:47.

[174] JS L. Shear-transformation-zone theory of deformation in metallic glasses. Scr Mater. 2006;54:375.

[175] Shimizu F, Ogata S, Li J. Yield point of metallic glass. Acta Mater. 2006;54:4293-8.

[176] ML F, JS L, L P. Thermal effects in the shear-transformation-zone theory of amorphous plasticity: comparisons to metallic glass data. Phys Rev E. 2004;70:011507.

[177] M Z, K S, WL J, SG M. Plastic deformation of metallic glasses: size of shear transformation zones from molecular dynamics simulations. Phys Rev B. 2006;73:172203.

[178] H B, ZP L, EP G. Theoretical strength and the onset of plasticity in bulk metallic glasses investigated by nanoindentation with a spherical indenter. Phys Rev Lett. 2004;93:125504.

[179] Mayr SG. Activation Energy of Shear Transformation Zones: A Key for Understanding Rheology of Glasses and Liquids. Phys Rev Lett. 2006;97:195501.

[180] Jang D, Greer JR. Transition from a strong-yet-brittle to a stronger-and-ductile state by size reduction of metallic glasses. Nat Mater. 2010;9:215-9.

[181] MW C, A I, W Z, T S. Extraordinary plasticity of ductile bulk metallic glasses. Phys Rev Lett. 2006;96:245502.

[182] Das J, Tang MB, Kim KB, Theissmann R, Baier F, Wang WH, et al. “Work-Hardenable” Ductile Bulk Metallic Glass. Phys Rev Lett. 2005;94:205501.

[183] Schroers J, Johnson WL. Ductile Bulk Metallic Glass. Phys Rev Lett. 2004;93:255506.

[184] Kim J-Y, Jang D, Greer JR. Nanolaminates Utilizing Size-Dependent Homogeneous

Plasticity of Metallic Glasses. Adv Funct Mater. 2011;21:4550-4.

[185] Donohue A, Spaepen F, Hoagland RG, Misra A. Suppression of the shear band instability during plastic flow of nanometer-scale confined metallic glasses. Appl Phys Lett. 2007;91:-.

[186] Ogata S, Shimizu F, Li J, Wakeda M, Shibutani Y. Atomistic simulation of shear localization in Cu–Zr bulk metallic glass. Intermetallics. 2006;14:1033-7.

[187] Shan ZW, Li J, Cheng YQ, Minor AM, Syed Asif SA, Warren OL, et al. Plastic flow and failure resistance of metallic glass: Insight from <i>in situ</i> compression of nanopillars. Physical Review B. 2008;77:155419.

[188] Volkert CA, Donohue A, Spaepen F. Effect of sample size on deformation in amorphous metals. J Appl Phys. 2008;103:-.

[189] Qiao JW, Zhang T, Yang FQ, Liaw PK, Pauly S, Xu BS. A Tensile Deformation Model for In-situ Dendrite/Metallic Glass Matrix Composites. Sci Rep. 2013;3.

[190] Hofmann DC, Suh J-Y, Wiest A, Duan G, Lind M-L, Demetriou MD, et al. Designing metallic glass matrix composites with high toughness and tensile ductility. Nature. 2008;451:1085-9.

[191] Wu Y, Zhou DQ, Song WL, Wang H, Zhang ZY, Ma D, et al. Ductilizing Bulk Metallic Glass Composite by Tailoring Stacking Fault Energy. Phys Rev Lett. 2012;109:245506.

[192] J E, J D, S P, C D. Processing routes, microstructure and mechanical properties of metallic glasses and their composites. Adv Eng Mater. 2007;9:443.

[193] Qiao JW, Sun AC, Huang EW, Zhang Y, Liaw PK, Chuang CP. Tensile deformation micromechanisms for bulk metallic glass matrix composites: From work-hardening to softening. Acta Mater. 2011;59:4126-37.

[194] Wang Y, Li J, Hamza AV, Barbee TW. Ductile crystalline–amorphous nanolaminates. Proceedings of the National Academy of Sciences. 2007;104:11155-60.

[195] Brandl C, Germann TC, Misra A. Structure and shear deformation of metallic crystalline–amorphous interfaces. Acta Mater. 2013;61:3600-11.

[196] Fratzl P, Gupta HS, Fischer FD, Kolednik O. Hindered Crack Propagation in Materials with Periodically Varying Young's Modulus—Lessons from Biological Materials. Adv Mater. 2007;19:2657-61.

[197] Gao H, Ji B, Jäger IL, Arzt E, Fratzl P. Materials become insensitive to flaws at nanoscale: Lessons from nature. Proceedings of the National Academy of Sciences. 2003;100:5597-600.

[198] Bonderer LJ, Studart AR, Gauckler LJ. Bioinspired Design and Assembly of Platelet Reinforced Polymer Films. Science. 2008;319:1069-73.

[199] Fratzl P, Gupta HS, Paschalis EP, Roschger P. Structure and mechanical quality of the collagen-mineral nano-composite in bone. J Mater Chem. 2004;14:2115-23.

[200] Barthelat F, Tang H, Zavattieri PD, Li CM, Espinosa HD. On the mechanics of mother-of-pearl: A key feature in the material hierarchical structure. Journal of the Mechanics and Physics of Solids. 2007;55:306-37.

[201] Luz GM, Mano JF. Biomimetic design of materials and biomaterials inspired by the structure of nacre. Philosophical Transactions of the Royal Society A: Mathematical, Physical and Engineering Sciences. 2009;367:1587-605.

[202] Fratzl P, Weinkamer R. Nature's hierarchical materials. Prog Mater Sci. 2007;52:1263-334.

[203] Launey ME, Buehler MJ, Ritchie RO. On the Mechanistic Origins of Toughness in Bone. Annual Review of Materials Research. 2010;40:25-53.

[204] Chen QZ, Wong CT, Lu WW, Cheung KMC, Leong JCY, Luk KDK. Strengthening mechanisms of bone bonding to crystalline hydroxyapatite in vivo. Biomaterials. 2004;25:4243-54.

[205] Meyers MA, McKittrick J, Chen P-Y. Structural Biological Materials: Critical Mechanics-Materials Connections. Science. 2013;339:773-9.

[206] Meyers MA, Chen P-Y, Lin AY-M, Seki Y. Biological materials: Structure and mechanical properties. Prog Mater Sci. 2008;53:1-206.

[207] Raabe D, Sachs C, Romano P. The crustacean exoskeleton as an example of a structurally and mechanically graded biological nanocomposite material. Acta Mater. 2005;53:4281-92.

[208] Gupta HS, Wagermaier W, Zickler GA, Raz-Ben Aroush D, Funari SS, Roschger P, et al. Nanoscale Deformation Mechanisms in Bone. Nano Lett. 2005;5:2108-11.

[209] Li X, Xu Z-H, Wang R. In Situ Observation of Nanograin Rotation and Deformation in Nacre. Nano Lett. 2006;6:2301-4.

[210] Gupta HS, Seto J, Wagermaier W, Zaslansky P, Boesecke P, Fratzl P. Cooperative deformation of mineral and collagen in bone at the nanoscale. Proceedings of the National Academy of Sciences. 2006;103:17741-6.

[211] Kassner ME, Nemat-Nasser S, Suo Z, Bao G, Barbour JC, Brinson LC, et al. New directions in mechanics. Mech Mater. 2005;37:231-59.

[212] Gao H, Yao H. Shape insensitive optimal adhesion of nanoscale fibrillar structures. Proceedings of the National Academy of Sciences of the United States of America. 2004;101:7851-6.

[213] Keren K, Berman RS, Buchstab E, Sivan U, Braun E. DNA-Templated Carbon

Nanotube Field-Effect Transistor. Science. 2003;302:1380-2.

[214] Tamerler C, Kacar T, Sahin D, Fong H, Sarikaya M. Genetically engineered polypeptides for inorganics: A utility in biological materials science and engineering. Materials Science and Engineering: C. 2007;27:558-64.

[215] Tamerler C, Sarikaya M. Molecular biomimetics: nanotechnology and bionanotechnology using genetically engineered peptides. Philosophical Transactions of the Royal Society A: Mathematical, Physical and Engineering Sciences. 2009;367:1705-26.

[216] Hnilova M, Karaca BT, Park J, Jia C, Wilson BR, Sarikaya M, et al. Fabrication of hierarchical hybrid structures using bio-enabled layer-by-layer self-assembly. Biotechnol Bioeng. 2012;109:1120-30.

[217] He Y, Ye T, Ribbe AE, Mao C. DNA-Templated Fabrication of Two-Dimensional Metallic Nanostructures by Thermal Evaporation Coating. J Am Chem Soc. 2011;133:1742-4.

[218] Fratzl P. Biomimetic materials research: what can we really learn from nature's structural materials? Journal of The Royal Society Interface. 2007;4:637-42.

[219] Bruet BJF, Song J, Boyce MC, Ortiz C. Materials design principles of ancient fish armour. Nat Mater. 2008;7:748-56.

[220] Bauer J, Hengsbach S, Tesari I, Schwaiger R, Kraft O. High-strength cellular ceramic composites with 3D microarchitecture. Proceedings of the National Academy of Sciences. 2014;111:2453-8.

Chapter 3: A brief introduction of molecular dynamics

Introduction

Molecular Dynamics (MD) is a typical atomistic simulation approach whose major purpose is to integrate Newton's motion for a set of atoms in a given system[1, 2]. MD is easy to implement and efficient for simulating massive systems (>10^{10} atoms)[3] with long-range interactions. In the context of statistics physics, MD is able to simulate thermodynamic ensembles, including canonical, micro canonical and grand canonical. The evolution of microstates of the given system allows MD to explore the whole system's potential energy surface (PES), providing insight into both equilibrium and non-equilibrium behavior of models. An advantage of MD simulation is that it's able to provide atomic resolution visualization of complex physical phenomena that are not accessible experimentally to date. With an appropriate potential function for describing atomic interactions, reliable physical quantities can be directly averaged from MD simulation results, allowing for comparison between experiments and simulations, and also guiding theory. Most importantly, MD provides boundless space for modeling systems which do not exist in nature, thereby assisting deep understanding of materials behavior and engineering.

This chapter will give an introduction of several of the essentials of MD simulation, including an introduction to atomic potential, MD implementation and evaluation of physical quantities. At the end of this chapter, an introduction to the construction of atomic configuration of typical nanoscale systems will be given.

3.1. Principles of Molecular Dynamics

3.1.1 Assumptions

Basically, classical MD simulations provide a highly simplified approach to cope with many body problem. Several assumptions, listed in the following, must be made in this approach [2, 4-6].

1. Classical MD simulations should follow Born-Oppenheimer approximation[7] in which motions of nucleus and electrons are isolated, implying a significant reduction of many body problem to many electrons problem. This approximation is widely valid in computer simulations, almost none of which can exactly obtain each electron’s current motion within a given system. Born-Oppenheimer approximation not only allows MD simulations to treat the motion of atoms as the motion of their nuclei, averaging electronic motion as atomic interaction, but also limits MD simulation to low temperature regimes (<~10^4K).
2. With the implementation of Born-Oppenheimer approximation, MD simulation treats atoms as rigid bodies without detailed structure. The information on spatial distribution of electrons is contained in a potential function, ψ. Atoms are simplified as rigid spheres interacting with each other via this potential function. Motion of rigid spheres in MD simulation follows Newton’s Law, with force evaluated from ψ. Coordinates and momentums of each sphere, $\{r_i, p_i\}$, constitutes a complete phase space which is explored by MD simulations.
3. Atomic interaction has a cutoff, beyond which the interaction is negligible. With this assumption, the computational consumption of

MD simulation is significantly reduced and high efficient parallelization of it becomes possible.

4. Atomic interactions in MD simulations must follow the linear superposition hypothesis, meaning that the potential energy from the interaction between *i* and *j*, ψ_{ij} is additive. This assumption allows the force exerted on atom *i* to be calculated as $F_i = \sum_{j=1}^{N} \nabla \psi_{ij}$ in which N is the number of neighboring atoms.

5. Generally speaking, MD simulation is an implementation of *importance sampling*, generating a time sequence of microstates of all atoms, $\{r_i, p_i\}$, in phase space. In equilibrium simulation, each microstate is considered as a representative of equilibrium ensemble. For non-equilibrium simulation, simulation volume can be divided into small volumes each of which is also considered as an equilibrium microstate. The equilibrium ensemble assumption allows direct calculation of thermodynamic observables from the microstates of atoms.

3.1.2 Equations in molecular dynamics

In MD simulations, time sequences of microstates are obtained via direct integration of Newton's second equation, $m_i a_i = \sum_{j=1}^{N} \nabla \psi_{ij}$. However, efficient exploration in phase space under a certain thermodynamic ensemble always requires other forms of Newton's law.

$$\begin{aligned} L &= \frac{1}{2}\sum_{i=1}^{n} m_i v_i^2 - \sum_{i<j} \Psi(r_{ij}) \\ \frac{d}{dt}\frac{\partial L}{\partial v_I} &- \frac{\partial L}{\partial r_i} = 0 \end{aligned} \qquad \text{Eq. 3.1}$$

The first of these forms is the Lagrangian equation, shown in Eq. 3.1, in which Ψ, L and n are potential function, Lagrangian and atom number of the given system, respectively. Integration of the Lagrangian equation provides advantages for solving atom velocity and position with external loading conditions such as boundary condition, constraints and exerted force. In practice, the solution of initial value problems for some specific system with external constraints and boundary conditions is achieved in Lagrangian form.

$$\begin{aligned} H &= \frac{1}{2}\sum_{i=1}^{n}\frac{P_i^2}{m_i} + \sum_{i<j}\Psi(r_{ij}) \\ \frac{dP_i}{dt} &= -\frac{\partial H}{\partial r_i} = -\frac{\partial \Psi}{\partial r_i} = F_i \end{aligned} \qquad \text{Eq. 3.2}$$

The second practical form of Newton's second law in MD simulation is the Hamiltonian canonical equation, as shown in Eq. 3.2. The Hamiltonian equation for a given system contains two terms, for kinetic energy and potential energy, respectively. Eq. 3.2 is suitable for determininging the dynamic evolution of a conservative system. It's convenient to add a friction term to the Hamiltonian equation from interaction with an external thermodynamic reservoir, allowing energy exchange to achieve different ensembles.

MD simulation is actually determinative. With given initial condition, potential function and motion equation, the dynamic evolution of the system is actually deterministic and predictive. The general procedure of MD simulation is as follows [6]:

1. Read the input of MD simulation, which includes atoms' positions, atom types, boundary conditions and potentials that describe atomic interactions.
2. Calculate forces exerted on each atom.

3. Solution of motion equation.
4. Calculate thermodynamic observables such as temperature, pressure.

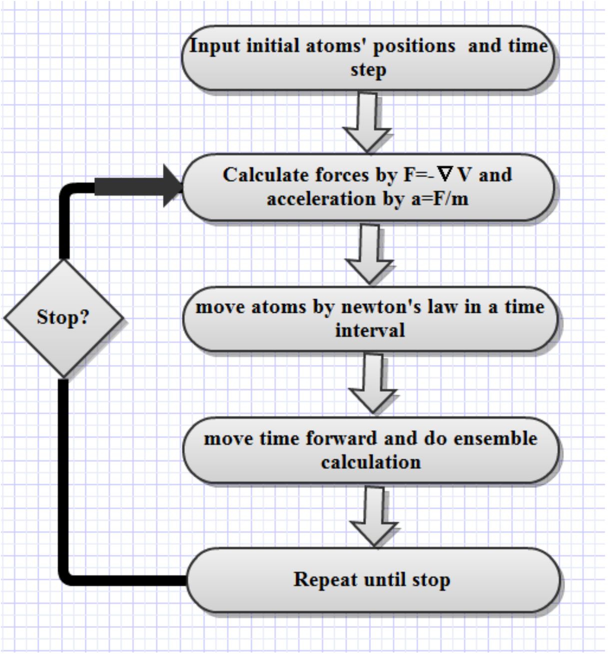

Figure 3.1. Simple description of Molecular Dynamics Simulation algorithm

From Fig. 3.1, it can be readily accepted that the key to MD simulation is the calculation of force and integration of the motion equation. It's found in practice that the force calculation is mostly computational. Without the third assumption, explained in section **3.1.1**, it's necessary to make $n(n-1)$ calculations to evaluate forces exerted on n atoms, implying computation complexity scales with n^2, which is not acceptable for massive atomistic simulations. With this assumption, evaluation of force exerted on an atom only requires the potential energy from interaction with its neighboring atoms within the cutoff. A neighbor-list algorithm is always employed to do the neighbor search. Its basic idea is to divide the three-dimensional simulation box into $N\times N\times N$ small boxes. Each box stores information about several atoms. Searching an atom's neighbors only requires iteration concerning atoms within the local box and its neighboring box. Thus, the computational complexity is reduced to scale with *nlog(n)*, which is practical and convenient for parallelization. A systematic numerical error is generated due to the cutoff assumption, since real atomic interaction is long range. A potential function with a bad tail approaching the cutoff (which is not smooth enough) will not be suitable for equilibrium MD simulation.

The solution of the motion equation is the core task of MD simulation. A simple algorithm is that of the finite difference method, which involves integrating a derivative equation by dividing time into discrete small intervals. If the interval is small enough, it's assumed that the force exerted on an atom remains invariant during the interval. For metallic systems, one femtosecond time interval is small enough. A successful algorithm should meet the following requirements [4, 6]:

1. Low computational consumption, low usage of memory.
2. Allows long time interval without significant systematic error.
3. The algorithm should be temporally reversible, since MD simulation is essentially deterministic.
4. It should be easily programmed.

In MD simulation, two simple integration algorithms are always utilized, the Verlet algorithm [8, 9] and the Predictor-corrector algorithm developed by Gear [10]. Here, we give a brief introduction to the Verlet algorithm. The mathematical basis of the Verlet algorithm is Taylor expansion of atomic displacements. Assuming the time interval is Δt, atom displacements at $t-\Delta t$ and $t+\Delta t$ are given by Eq. 3.3. Thus the atom displacement is explicitly expressed as Eq. 3.4; in contrast, atom velocity is implicitly expressed as Eq. 3.5.

$$\begin{aligned} r(t+\Delta t) &= r(t)+\Delta t v(t)+\frac{1}{2}\Delta t^{2}a(t)+... \\ r(t-\Delta t) &= r(t)-\Delta t v(t)+\frac{1}{2}\Delta t^{2}a(t)+... \end{aligned} \quad \text{Eq. 3.3}$$

$$r(t+\Delta t)=r(t)-r(t-\Delta t)+\Delta t^{2}a(t)+... \quad \text{Eq. 3.4}$$

$$v(t)=\frac{r(t)-r(t-\Delta t)}{2\Delta t} \quad \text{Eq. 3.5}$$

Eq 3.4 and Eq. 3.5 are differential equations of the Verlet algorithm. They are the differential accuracy of displacement and the velocity scale with Δt^2 and Δt^4, respectively. Advantages of Verlet algorithm include simple and direct implementation, low computational consumption and appropriate memory cost. The original Verlet differential equations Eq. 3.4 and 3.5 have several intrinsic disadvantages. First, they cannot be automatically activated at $t=0$ since new displacement calculation must require current and last time step displacement, according to Eq. 3.4. The second is that the accuracy of velocity is not high enough. To overcome these shortcomings, improved Verlet algorithms are presented (Leap-frog[6] and Velocity-Verlet[11]). Differential equations for Velocity-Verlet are shown in Eq. 3.6 in which only current displacement, velocity and acceleration are used, without loss of accuracy.

$$\begin{aligned} r(t+\Delta t) &= r(t)+\Delta t v(t)+\frac{1}{2}\Delta t^{2}a(t) \\ v(t+\Delta t) &= v(t)+\frac{1}{2}\Delta t[a(t)+a(t+\Delta t)] \end{aligned} \quad \text{Eq. 3.6}$$

A model in MD simulation should contain initial atomic coordinates, velocity and boundary conditions. Then the dynamic evolution of all atoms is obtained by integrating with the motion equation. Atom coordinates can be either set by mimicking realistic condensed matter or by artificially designing material structure. The initial velocity should be set to reflect certain physical requirements. A specific situation is the setup for temperature, setting initial velocity to follow the Maxwell-Boltzmann distribution. The boundary conditions of the simulation box can be set to be either periodic or free. For free boundary conditions, the simulation box suffers from free surface effect due to small sample size [5]. For periodic boundary conditions (PBC), the free surface effect is eliminated and the sample interacts with its own image across the boundary. PBC is widely used in atomistic simulation of condensed matter, allowing for simulating the behavior of infinite samples. However, PBC has an intrinsic disadvantage. If the sample size is small and contains defects, the interaction between defects and their images becomes significant during simulation. Sometimes these strong interactions induce confusion, especially when simulating dislocation behaviors of metallic systems [12]. If the sample size is large enough, the image effect is negligible.

Trade-off between sample size and simulation time must be made in MD simulation. The upper time limit for sample size in MD simulation is determined by the capability of the computation platform. For the simulations in this dissertation, when the sample size is increased, more computational time is needed to attain a certain strain level at an expected strain rate. Otherwise, one can increase the strain rate to achieve that certain strain level, but then the applied strain rate must be very large. This trade-off between sample size and strain rate is illustrated schematically in Fig. 3.2. Here the time domain is inversely related to the strain rate. So the upper time limit can be increased with decreasing strain rate and vice versa. If lower strain rates are desired, it is necessary to decrease the size of the atomic model because of the time needed to run the simulation.

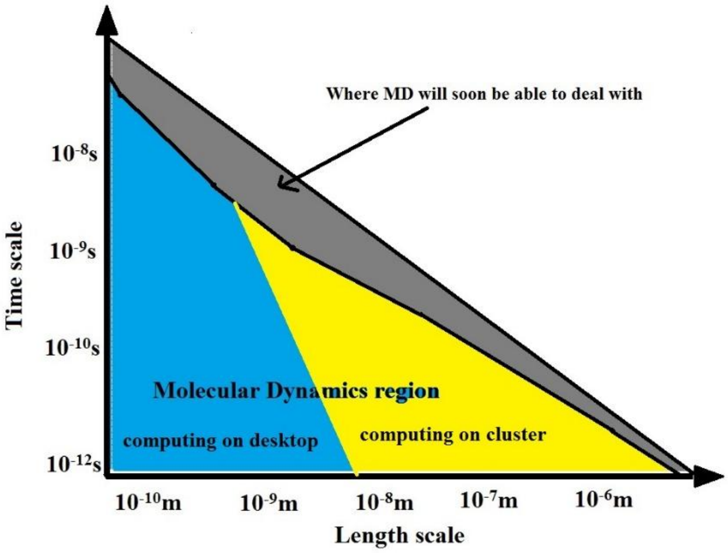

Figure 3.2. Trade-off between sample size and strain rate in MD simulation

3.1.3 Temperature and pressure control

For equilibrium simulation, it's necessary that several thermodynamic observables should be maintained invariant during simulation, such as energy, temperature, volume and pressure. Thus it's necessary that the Hamiltonian commutation of the invariant observables should be adjusted during simulation. For example, in MD simulation with constant pressure, the volume should be adjusted. Current MD simulation can achieve a wide range of thermodynamic ensembles, including NVE (micro canonical ensemble), NVT (canonical ensemble), NPH (constant enthalpy and pressure ensemble), NPT (constant pressure and temperature ensemble) and μVT (grand canonical ensemble). It's clear that temperature and pressure control play key roles in equilibrium MD simulation.

$$E_k = \frac{d}{2} N k_B T \qquad \text{Eq. 3.7}$$

In the context of statistical physics, the temperature of an equilibrium system is directly correlated with particles' kinetic energy, as shown in Eq. 3.7 in which d is the dimensionality of system, E_k is kinetic energy, T is temperature and k_B is the Boltzmann constant. Thus in MD simulation the control of temperature can be directly achieved via adjusting particles' velocities. Another approach to control temperature is achieved via conceptually contacting the simulation system to a thermodynamic isothermal bath. Constant system temperature is a natural result of integration of the motion equation with terms from interaction with the isothermal bath. Several typical isothermal bath is briefly described as following.

1. Berendsen isothermal bath [13]

The coupling between a system and a Berendsen bath is simply described as scaling particle velocity by a factor which is determined by the difference between system temperature and bath temperature. The scaling factor λ is given in Eq. 3.8 in which τ is the damping parameter controlling the fluctuation of the system's temperature.

$$\frac{\lambda^2 T - T}{\Delta t} = \frac{1}{\tau}(T_0 - T) \qquad \text{Eq. 3.8}$$

2. Andersen isothermal bath [14]

The coupling between system and an Andersen bath is described by adjusting the velocities of particles, which undergo random collision, to Maxwell-Boltzmann distribution, with an expected temperature. Coupling strength is determined by collision frequency. Energy exchange between the Andersen bath and the simulation system is also achieved via random collision. The random collisions make the trajectory in phase space become a Markov process, implying that an Anderson bath can indeed generate an equilibrium temperature in simulation.

3. Nose-Hoover isothermal bath [15]

Contacting the system with a Nose-Hoover isothermal bath is achieved via introducing an extra freedom *s* in the motion equation. The extra freedom *s* describes the coupling as friction. The extended motion equation is as shown in Eq. 3.9, which was developed by Hoover.

$$\begin{cases} \xi = \frac{1}{s}\frac{ds}{dt} \\ \frac{dr_i}{dt} = \frac{p_i}{m_i} \\ \frac{dp_i}{dt} = -\frac{\partial \Psi}{\partial r_i} - \xi p_i \\ \frac{d\xi}{dt} = \frac{1}{Q}[\Sigma \frac{p_i^2}{m_i} - 3Nk_B T] \end{cases} \qquad \text{Eq.3.9}$$

In Eq. 3.9, ζ is the friction factor, Q is the corresponding mass of extra freedom *s*. Q reflects the “thermodynamic inertia” of the Nose-Hoover isothermal bath. Thus the energy exchange rate between Nose-Hoover bath and simulation system decreases with increasing Q. Decreasing Q can reduce the time required to make the system achieve the expected temperature, but small Q will also decrease the friction effect to induce large fluctuations of the system’s temperature.

4. Langevin isothermal bath [16]

The Langevin isothermal bath is based on Langevin dynamics. By contacting the Langevin isothermal bath, particles within the system suffer from two extra forces, despite atomic interaction: the dissipative force and thermal noise. The equilibrium between dissipation and thermal noise induces a constant system temperature.

MD simulation controls pressure via adjusting volume. Like temperature, constant pressure can also be achieved via contacting the system to an isobaric bath. The coupling effect between system and isobaric bath induces rescale of system volume. Several typical isobaric bathes are briefly described below.

1. Berendsen isobaric bath [13]

The coupling between system and Berendsen isobaric bath is simply described as scaling system volume by a factor which is determined by the difference between system pressure P and bath pressure P_0. The scaling factor λ is given in Eq. 3.10 in which τ_P is the damping parameter, which controls the fluctuation of system's pressure; and κ is the adiabatic compression parameter. The new atomic configuration is obtained by rescaling atomic positions by a factor of $\lambda^{1/3}$. This approach allows the system to change scale separately along three individual dimensions to simulate uniaxial deformation. However, the Berendsen bath is not able to simulate shear deformation.

$$\lambda = 1 + \kappa \frac{\Delta t}{\tau_P}(P - P_0) \qquad \text{Eq. 3.10}$$

2. Andersen isobaric bath [14]

The coupling between Andersen isobaric bath and simulated system is treated by employing system volume as an extra freedom degree. The volume freedom is equal to a piston with mass of Q, kinetic energy of $Q(dV/dt)^2/2$, and potential energy of PV. Thus the new Hamiltonian is expressed as Eq. 3.11 in which P is expected pressure, V is volume, H_0 is original Hamiltonian, as shown in Eq. 3.2. The motion equation of the system in contact with the Anderson isobaric bath then can be readily evaluated by substituting Eq. 3.11 for Eq. 3.2. This approach can only be utilized for simulation of hydropressure loading, and the simulation box must be cubic during deformation.

$$H = H_0 + \frac{1}{2}(\frac{dV}{dt})^2 - PV \qquad \text{Eq. 3.11}$$

3. Parrinello-Rahman approach [17-19]

To achieve shear deformation in MD simulation, Parrinello and Rahman proposed a new approach which changes the shape as well as the size of the box during simulation. Unlike in the Anderson approach, six extra freedom degrees are employed in the Parrinello-Rahman approach (PR approach) to represent both shape and volume of simulation box, making simulation of shear deformation possible.

$$h = (a \quad b \quad c) = \begin{bmatrix} a_1 & b_1 & c_1 \\ a_2 & b_2 & c_2 \\ a_3 & b_3 & c_3 \end{bmatrix} \qquad \text{Eq. 3.12}$$

$$r_{ij}^2 = (s_i - s_j)^T G(s_i - s_j) \qquad \text{Eq. 3.13}$$

The PR approach employs a volume matrix *h* to represent the shape and volume of the simulation box. The expression of *h* is shown in Eq. 3. 12 in which vectors *a, b* and *c* are along three edges of the simulation box. The volume of the box is $V=det(h)$, and the real coordinates of atom *i* are $r_i=hs_i$ in which s_i is the scaled coordinates utilized in calculation. By defining $G=h^Th$ as scale tensor, the distance between atom *i* and *j* is expressed by Eq. 3.13, which can be used to evaluate potential energy and atomic force. Now for arbitrary stress loading, a new Lagrangian of the system should contain terms for extra freedoms for ‘potential energy’ and ‘kinetic energy’, which are the third and fourth terms on the right side of Eq. 3.14, in which *Q* is the box “mass” relating to extra freedoms, *P* is applied stress. It should be noted that all terms in Eq. 3.14 are further expressed in *h* and *s*. The derivative equations that determine evolution of *h* and *s* can be obtained from Eq. 3.14. It must be emphasized that the parameter Q controls the coupling strength between isobaric bath and system. Q should be carefully chosen. It should be small enough to make sure the system can undergo enough oscillations before it arrives at thermodynamic equilibrium. It should also be large enough to make sure the response is realistic. Due to the PR approach's advantage in controlling pressure, it is widely utilized in MD simulations.

$$L = \frac{1}{2}\sum_{i=1}^{n} m_i v_i^2 - \sum_{i<j} \Psi(r_{ij}) + \frac{1}{2} Q \sum_{\alpha}\sum_{\beta} \dot{h}_{\alpha\beta}^{2} - PV \qquad \text{Eq. 3.14}$$

3.1.4 Analysis and visualization of molecular dynamics simulation results

The elementary results of classical MD simulations are coordinates and velocities of atoms in the system. Atom potential energy can directly be obtained by substituting atomic coordinates for potential function. Analysis of big data obtained by MD simulation yields two types of results, thermodynamic observables and local structure. Because of the assumption that a microstate in equilibrium MD simulation can represent an ensemble, thermodynamic observables can be averaged over all atoms. These observables include energy, pressure, temperature and so on, all evaluated from coordinates, velocities and potential energy. Another major goal of MD simulation is to obtain the microstructural evolution of a given system, which first requires description of microstructure. Most structure analysis methods in MD simulation obtain local atomic structure as evaluated, mostly, from coordinates. Complete three-dimensional structure description, which may use atomic structure as input, remains quite simple. It is quite encouraging that both thermodynamic observables and structure obtained in MD simulation can be directly compared with experimental results. In some areas, MD simulations show identical atomic structure as observed by transmission electron microscopy (TEM). In the following, a brief introduction to the evaluation of typical thermodynamic observables (temperature, energy, pressure) and several typical structure analysis methods is given.

Temperature is quite easy to obtain, following Eq. 3.7. The total energy of a system includes the kinetic energy and potential energy of all atoms. It should be noted that this total energy is internal energy in thermodynamics. Enthalpy of the system can be obtained by adding *PV* to total energy. Another notation must be made: MD simulations cannot include entropy of the system because evaluation of entropy requires many sources relating to both atomic structure and chemical composition.

$$P = \frac{Nk_B T}{V} + \frac{\sum r_i \bullet F_i}{dV} \qquad \text{Eq. 3.15}$$

$$P_{\alpha\beta} = \frac{\sum m_i v_i^{\alpha} v_i^{\beta}}{V} + \frac{\sum r_i^{\alpha} F_i^{\beta}}{dV} \qquad \text{Eq. 3.16}$$

$$S_{\alpha\beta} = -[m v_{\alpha} v_{\beta} + \frac{1}{2} \sum_{n=1}^{N_{neighbor}} (r_{\alpha}^{1} F_{\beta}^{1} + r_{\alpha}^{2} F_{\beta}^{2}) + \ldots] \qquad \text{Eq. 3.17}$$

$$P_{\alpha\beta} = \frac{\sum S_{\alpha\beta}}{V} \qquad \text{Eq. 3.18}$$

The pressure within the system is computed by the formula shown in Eq. 3.15 in which *V* is the system volume, F_i is the force, and *d* is the dimensionality of the system [20-22]. The second term on the right side of Eq. 3.15 is the virial. A symmetric pressure tensor can be similarly computed with Eq. 3.15, using components of kinetic energy and virial as shown in Eq. 3.16. Another approach to obtaining pressure tensor is by averaging the atomic stress tensor over a given volume. The atomic stress tensor $S_{\alpha\beta}$ is computed following formula Eq. 3.17 in which the first term is from kinetic energy, the second term is from pairwise potential energy, and three-body, four-body… potential energy terms are ignored. It should be noted that the potential energy term is only from contributions of atoms within the potential function cutoff point. For arbitrary volume *V*, both pressure tensor and stress tensor can be calculated following Eq. 3.18. Averaging the atomic stress tensor is suitable for local stress analysis. It should be noted that if *V* is very small, containing only a few atoms, the stress calculation may not be reliable because it is quite hard to accurately obtain the volume of these atoms. From thermodynamics, the fluctuation of pressure and temperature is proportional to the square root of *1/N*. This also implies that computation of pressure and temperature is not reliable if the atom number *N* is small. Thus, massive MD simulation sometimes is necessary if we want to compare thermodynamics directly with experimental measurements.

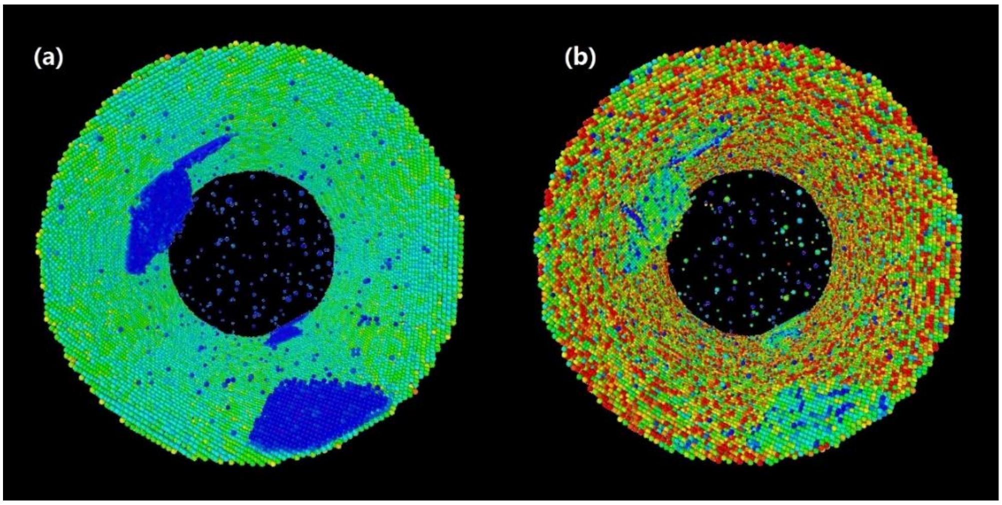

Figure 3.3. Top perspective view of copper nanowire. Crystal atoms are deleted, defect atoms are colored by (a) atomic potential energy and (b) atomic stress component S_{zz}.

One reason why MD simulation is so attractive in the research community is that it allows us direct visualization of the microstructure evolution of a given system, allowing three-dimensional description of materials' atomic structures. In contrast, current experimental technique can hardly do such things. A simple visualization approach is that of coloring atoms according to their atomic properties, such as stress and energy. Fig. 3.3 shows a perspective view of a copper nanowire from the top. Crystal atoms are deleted (having been identified by the Ackland method), so that only surface atoms and defect atoms within the nanowire are shown. Atoms are colored according to potential energy and atomic stress in Fig. 3.3(a) and Fig. 3.3(b), respectively. It is clear that on the nanowire's surface, the distribution of atomic potential energy has a pattern.

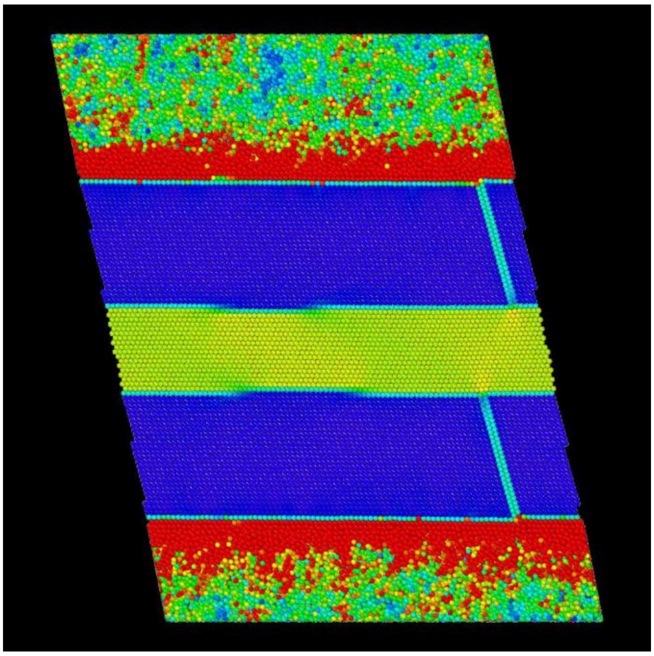

Figure 3.4. Atomic structure of amorphous/crystal nanolaminate, atoms colored according to Von Mises atomic shear strain. Top and bottom layers are amorphous, the rest are crystal.

Further structure visualizations of MD results can be based on mathematical operations on atomic coordinates, velocities, energies and other atomic properties at different simulation times. For example, atomic shear strain analyses[23] based on atom coordinates are always utilized to visualize atom deformation distribution. This method requires a current state and a reference state. Displacements between atom i and its neighbor j at the reference state and the current state are represented by d^0_{ij} and d_{ij}, respectively, which are related to each other by a deformation matrix J_i. For each atom i, J_i can be computed following a minimization procedure, as shown in Eq. 3. 19. Then atomic Lagrangian deformation matrix η_i is computed from J_i as Eq.3.20. η_i stores the deformation information of atoms. A good parameter for measuring the magnitude of plastic deformation, the Von Mises atomic shear strain, η^{mises} , is evaluated from components η_i, following formula Eq. 3.21. Fig. 3.4 shows Von Mises atomic shear strain map of amorphous/crystal nanolaminate during shear deformation. It's quite clear that shear localization occurs at amorphous/crystal interface.

$$\min\{\sum_{j}^{neighbor} |d_{ij}^{0}J_i - d_{ij}|^2\} \rightarrow J_i = (\sum_{j}^{neighbor} d_{ij}^{0T} d_{ij}^{0})^{-1}(\sum_{j}^{neighbor} d_{ij}^{0T} d_{ij})^{-1} \qquad \text{Eq. 3.19}$$

$$\eta_i = \frac{1}{2}(J_i J_i^T - I) \qquad \text{Eq. 3.20}$$

$$\eta^{mises} = \sqrt{\eta_{yz}^2 + \eta_{xz}^2 + \eta_{xy}^2 + \frac{(\eta_{xx}-\eta_{yy})^2 + (\eta_{xx}-\eta_{zz})^2 + (\eta_{zz}-\eta_{yy})^2}{6}} \qquad \text{Eq. 3.21}$$

3.1.5 Structure analysis methods

The description of atomic structure plays an important role in MD simulation. It can provide knowledge of how materials' microstructures respond to external loading. For example, structure analysis can produce a direct picture of grain boundary structure and nucleation, as well as the propagation of dislocations. The core task of structure analysis is to group atoms according to different structure types, *e.g.,* body center cubic (BCC), face center cubic (FCC), hexagonal close packing (HCP) and icosahedron (IC). In this section, we will, in sequence, introduce three typical atom structure analysis methods - the coordination number method (CN), common neighbor analysis (CNA) [24] and the Ackland method [25].

The CN method is quite simple and has wide application. It uses the coordination number, which is the number of neighboring atoms within bonding distance, to group atoms. For example, the CN of an atom in BCC is eight, while the CN of an atom in FCC and HCP structures is twelve. It’s clear that the CN method cannot tell FCC from HCP. It should be noted that the CN of an IC, which is not a lattice structure, is also twelve, so that the CN method cannot effectively distinguish a lattice atom from a defect atom. Fig. 3. 5(a) is an example of CN analysis, showing the coordination number distribution pattern on a copper nanowire’s surface.

The CNA method[24], also known as pair analysis, groups atoms by their bonding conditions with their neighbors. The bonding between atom and one of its nearest neighbors is described by three integers {i, j, k}. The first integer is the number of common neighbors of the two atoms forming the bonding. The second integer is the number of pair bondings among these common neighbors. Bonding exists only if the distance between two atoms is smaller than a given bond length. Generally speaking, bond length is constant when strain is not great, but adaptive bond length must be employed when strain is great. The third integer is the number of continuous bonding chains among these common neighbors. If an atom has twelve nearest neighbors and twelve bonds, it may be an FCC, an HCP or an IC atom. By employing the CNA method, these twelve bonds can be grouped. If all bonds are {4, 2, 1}, the atom is FCC. If the number of {4, 2, 1} bonds equals to that of {4, 2, 2} bonds, the atom is FCC. If there are {5, 5, 5} bonds, the atom is IC. In general, the CNA method is able to group atoms into BCC, FCC, HCP, IC and UNKNOWN. Fig. 3. 5(b) shows atomic structure of copper nanowire without FCC atoms. Stacking of fault atoms (HCP atomic planes) can be clearly seen within the nanowire.

The CN and CNA methods both have the same disadvantage – they are not able to identify highly distorted lattices which may be generated during large deformation under high temperature. To assign local crystal structure more efficiently and accurately, Ackland proposed a new method[25], which uses the angular distribution function of bonds as input. For atom i, eight numbers χ_k are computed to reflect the distribution of $cos(\theta_{ijk})$ in which θ_{ijk} represents the angle between two bonds ij and ik. Each χ_k is the total count number for that $cos(\theta_{ijk})$ that falls into a predefined range. In the simplest situation, χ_0 =7, 6, 3 represents BCC, FCC and HCP, respectively. For a distorted lattice, combinations of several χ_k are defined to indicate different lattice structures. For example, $0.61(|\chi_0 +\chi_1 -6|+\chi_2)/6$ and $(|\chi_0 -3|+|\chi_0 +\chi_1 +\chi_2 +\chi_3 -9|)/12$ are used as indicators of FCC and HCP structures, respectively. The Ackland method shows significant advantage over CN and the CNA method, as it can identify highly distorted lattices. It's faster and more reliable than previous atomic structure analysis methods. Fig. 3. 5(c) shows the atomic structure of copper nanowire, with FCC atoms deleted.

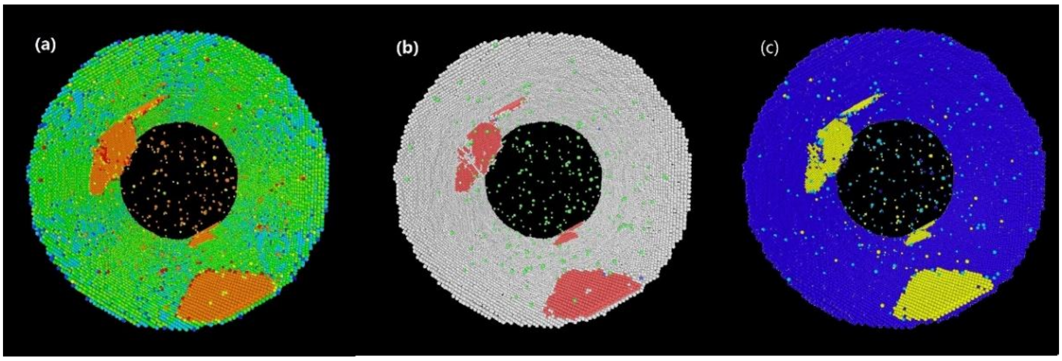

Figure 3.5. Top perspective view of copper nanowire. Crystal atoms are deleted, defect atoms are colored according to (a) coordination number, (b) common neighbor analysis and (c) Ackland method.

3.2. Potential functions

It can be clearly deduced from the discussion above that it is the accuracy of potential function that determines whether an MD simulation is successful or not. Potential functions reflect the intrinsic physics of interatomic interactions in condensed matter systems. With classical MD simulation, potential functions are approximations that are highly simplified representations of real interatomic interactions. Most potential functions' mathematical forms strongly depend on the distribution of electrons among nuclei. Dynamics and band structures of electrons are normally ignored. Basically, potential functions are static and only vary with atomic coordinates. The effects of particle velocity and quantum effects are not taken into account in classical MD simulations. However, potential functions are still able to describe numerous systems due to the universal applicability of Born-Oppenheimer approximations for low temperature regions (<~10^4K). Indeed, it's necessary to test some physical properties to determine the applicability of a potential function for considering problems. For example, to study a mechanical problem requires direct comparison between simulated and experimentally measured elastic modulus and defect energy. There are some properties which must be tested before a potential is utilized, including cohesion energy, heat capacity, expansion coefficient and diffusivity. Thus the reliability of potential functions can be partially determined in advance from the differences between experiments and MD simulations for obtaining these quantities. In this section, we will introduce two commonly used potentials, pairwise potentials and potentials obtained by the embedded atom method (EAM).

3.2.1 Pairwise potential functions

Pairwise potentials [4] are simplest in form, as only two atoms form an interatomic bond. Normally a pairwise potential function has two terms. The first term in a pairwise potential reflects the increasing repulsive force between two atoms as the separation between them decreases. The second term reflects the decreasing attractive force between two atoms as the separation between them increases. The Lennard-Jones (LJ) potential, the Mores potential and the Born-Mayer potential are widely used in MD simulations.

$$\psi_{ij}(r_{ij}) = 4\varepsilon_0[(\frac{\sigma_0}{r_{ij}})^{12} - (\frac{\sigma_0}{r_{ij}})^{6}] \qquad \text{Eq. 3.22}$$

$$\psi_{ij}(r_{ij}) = D\{1-\exp[-\beta(r_{ij} - r_0)]\}^2 \qquad \text{Eq. 3.23}$$

$$\Psi = \sum_{i<j}\psi_{ij}(r_{ij}) \qquad \text{Eq. 3.24}$$

A popular form of LJ potential is shown in Eq. 3.22 in which ε_0 is cohesion energy, $2^{1/6}\sigma_0$ is the distance at which attractive force equals repulsive force. An illustration of LJ potential and its derivative is that in Fig. 3.6, which shows rapidly decreasing magnitude of interatomic force with increasing distance. A form of the Morse potential function is Eq. 3.23 in which r_0 is equilibrium interatomic separation, D and β are fitting parameters. Curves showing Eq. 3.23 and its derivative form should have the same morphologies as that in Fig. 3.6. It’s quite clear that the Morse potential is a bit more computational than the LJ potential.

It has been confirmed that pairwise potentials are suitable for simulation of inert gases and simple metals even though they have very few fitting parameters. However, for the simulation of metallic materials, the yielding of Cauchy relation, $c_{12}=c_{44}$, is unavoidable. Because of the anisotropic mechanical properties of most single crystal metals, pairwise potential functions don't work for simulating mechanical problems.

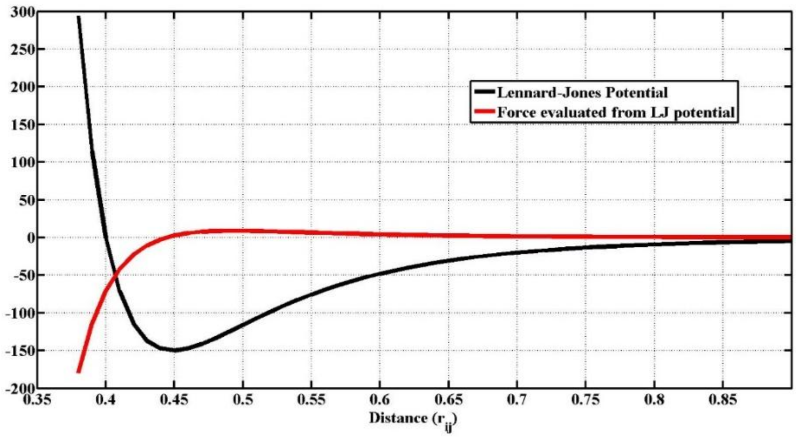

Figure 3.6. An illustration of the Lennard-Jones potential and related force

3.2.2 EAM potential functions

The coexistence of metallic bonding and covalent bonding components in transitional metallic systems has finally been described in recent decades. According to density function theory (DFT), interatomic force depends on local electronic density, which is determined by the surrounding environment of nucleuses.

$$\Psi = \sum_{i} F_i(\rho_i) + \sum_{i<j} \psi_{ij}(r_{ij}) \qquad \text{Eq. 3.25}$$

From this knowledge, a number of homogeneous many-body potential functions have been developed, including the Second moment model by Cyrot and Lackmann [26], the effective medium theory by Norskove and Lang [27], EAM by Daw and Baskes [28], the glue model by Ercolessi [29], the Finnis-Sinclair model [30] and so on. Total internal energy in these many-body potentials can all be expressed as Eq. 3.25 in which the first term represents "embedded energy" induced by embedding an atom in an electron cloud with density ρ_i, the second term is the pairwise energy part.

Daw and Baskes [28] made three assumptions in evaluating the mathematical form of the first term in Eq. 3.25. The first is that “embedded energy” is a function of local electron density and its derivatives. The second is that electron density induced by a single atom in solids has spherical symmetry. The third is that local electron density is a linear combination of that induced by all atoms within a cutoff point. Functions, $F(\rho)$ and $\rho(r)$, are fitted from lattice constant, elastic modulus, vacancy energy, heat capacity and so on. EAM potential is suitable for MD simulations in problems such as those of amorphous structure, interfacial plasticity, and dislocation core structure and so on in metals.

EAM potential has its disadvantages. For example, significant deviation from the real physical picture can be induced by the simple spherical electron density assumption. Thus it cannot deal with directional atom bonding. EAM potential cannot describe systems with covalent bonding, nor semiconductors. Several improvements have been made on the primitive EAM model. Readers can refer to a review paper by Daw and Baskes for more details [31].

3.3 Construction of polycrystalline nanomaterial models

In this dissertation, four nanoscale systems are constructed, including nanocrystalline copper, nanotwinned single crystal copper, amorphous/crystal nanolaminates and amorphous coated nanowire. This section will only discuss how to model the atomic structure of polycrystalline nanomaterials; construction of the others can be found in the following chapters.

Cluster compaction, quenching from melts and the Voronoi method have all been employed to obtain stable atomic configurations of nanocrystalline metals [32]. However, for systems with millions of atoms, cluster compaction and quenching from metals consume too much computational time, being hardly possible with current computational capability. In our work, the Voronoi method was adopted to generate the initial unstable energetic atomic structure of nanocrystalline metal [33]. Four construction steps are described.

(1) As shown in Fig. 3.7, a cubic block is used to represent a piece of nanocrystal, subdivided into N×N×N small cubic blocks of size L_2. Then smaller cubic blocks of size L_1 are placed in the center of each block, of size L_2 ($L_1 < L_2$). The L_1 blocks are chosen to be the nucleus distribution areas of the crystal seeds corresponding to the L_2 blocks.

(2) Within each L_1 block, a randomly positioned point is selected as the site of a crystal nucleation seed (as point "O" in Fig. 3.1). For each randomly placed point, a polyhedral is created, within which a nanosized grain is placed. These polyhedrals are composed of the equally-divided perpendicular planes of the lines joining each point and its 26 nearest-neighboring points. The random distribution of the nucleus results in irregular and randomly-shaped polyhedrals, i.e. the shapes of the grains.

(3) Starting from the center point of each polyhedron where the nucleus of this grain is supposed to be, atoms with crystalline periodicity are filled into the polyhedron until the distance between the atom and the edge plane of a polyhedron is smaller than kR_0 (k is a positive constant, R_0 is the smallest distance between atoms in lattice). The orientation of each grain is also randomly selected by setting its rotation axis and angle at a random number. In this work, [001], [010] and [100] are randomly chosen as rotation axes. Atoms are supposed to be hard spheres in MD simulations. The nearest distance between two atoms in two neighboring polyhedrons is set to be less than the diameter of an atom.

(4) For the bulk simulated, a three-dimensional periodic boundary condition is adopted, which makes the block effectively infinite and eliminates the influence of the boundary on the simulation results.

With the Voronoi method proposed above, an unrelaxed nanocrystalline metal model with high internal energy and stress can be constructed. The average grain size is decided by L_2. The ratio between L_1 and L_2 controls the random characteristics of the size and the shape of grains. Another controllable variable in this method, kr_0, is defined as the boundary displacement variable, which determines the magnitude of the allowed maximum displacement normal at the edges of polyhedra atoms in the boundary area. The variables, including L_1/L_2 and kr_0, should be carefully selected for analyzing the different structures. In this work, L_1/L_2 and k are fixed to be 0.7 and 1.0 respectively for the reason that internal stress after relaxation should be as small as possible.

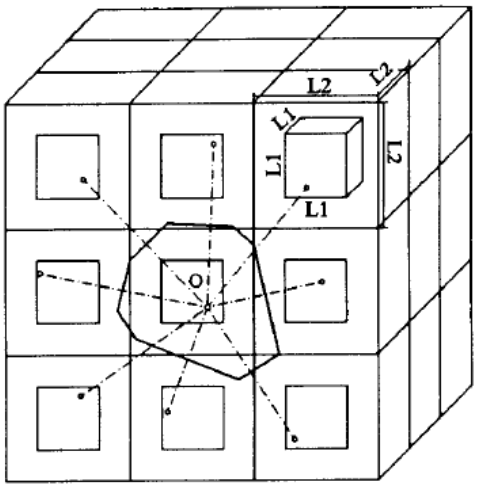

Figure 3.7. Schematic view of a block to construct the nanocrystalline metal. The polyhedron represents a grain with point "O" as the nucleation site. Reprinted from Ref[33].

Reference

[1] Hoffmann KH, Schreiber M. Computational physics: China Science Press; 2001.

[2] Leach AR. Molecular modelling: principles and applications: Pearson Education; 2001.

[3] KADAU K, GERMANN TC, LOMDAHL PS. Large-scale molecular-dynamics simulation of 19 billion particles. International Journal of Modern Physics C. 2004;15:193-201.

[4] Allen M, Tildesley D. Computer simulation of liquids, 1987. New York: Oxford. 1989;385.

[5] Rapaport DC. The art of molecular dynamics simulation: Cambridge university press; 2004.

[6] Frenkel D, Smit B. Understanding molecular simulation: from algorithms to applications: Academic press; 2001.

[7] Born M, Huang K, Lax M. Dynamical theory of crystal lattices. American Journal of Physics. 1955;23:474-.

[8] Verlet L. Computer" experiments" on classical fluids. I. Thermodynamical properties of Lennard-Jones molecules. Physical review. 1967;159:98.

[9] Verlet L. Computer" experiments" on classical fluids. ii. equilibrium correlation functions. Physical Review. 1968;165:201.

[10] Gear CW, Gear CW. Numerical initial value problems in ordinary differential equations: Prentice-Hall Englewood Cliffs, NJ; 1971.

[11] Swope WC, Andersen HC, Berens PH, Wilson KR. A computer simulation method for the calculation of equilibrium constants for the formation of physical clusters of molecules: Application to small water clusters. The Journal of Chemical Physics. 1982;76:637-49.

[12] Bulatov V, Cai W. Computer simulations of dislocations: Oxford University Press; 2006.

[13] Berendsen HJ, Postma JPM, van Gunsteren WF, DiNola A, Haak J. Molecular dynamics with coupling to an external bath. The Journal of chemical physics. 1984;81:3684-90.

[14] Andersen HC. Molecular dynamics simulations at constant pressure and/or temperature. The Journal of chemical physics. 1980;72:2384-93.

[15] Nosé S, Yonezawa F. Isothermal–isobaric computer simulations of melting and crystallization of a Lennard‐Jones system. The Journal of chemical physics. 1986;84:1803-14.

[16] Schneider T, Stoll E. Molecular-dynamics study of a three-dimensional one-component model for distortive phase transitions. Physical Review B. 1978;17:1302.

[17] Parrinello M, Rahman A. Crystal structure and pair potentials: A molecular-dynamics study. Phys Rev Lett. 1980;45:1196.

[18] Parrinello M, Rahman A. Polymorphic transitions in single crystals: A new molecular dynamics method. J Appl Phys. 1981;52:7182-90.

[19] Parrinello M, Rahman A. Strain fluctuations and elastic constants. The Journal of Chemical Physics. 1982;76:2662-6.

[20] Lutsko J. Stress and elastic constants in anisotropic solids: molecular dynamics techniques. J Appl Phys. 1988;64:1152-4.

[21] Cormier J, Rickman J, Delph T. Stress calculation in atomistic simulations of perfect and imperfect solids. J Appl Phys. 2001;89:99-104.

[22] Zimmerman J, WebbIII E, Hoyt J, Jones R, Klein P, Bammann D. Calculation of stress in atomistic simulation. Modell Simul Mater Sci Eng. 2004;12:S319.

[23] Shimizu F, Ogata S, Li J. Theory of Shear Banding in Metallic Glasses and Molecular Dynamics Calculations. MATERIALS TRANSACTIONS. 2007;48:2923.

[24] Honeycutt JD, Andersen HC. Molecular dynamics study of melting and freezing of small Lennard-Jones clusters. J Phys Chem. 1987;91:4950-63.

[25] Ackland GJ, Jones AP. Applications of local crystal structure measures in experiment and simulation. PHYsical Review B. 2006;73:054104.

[26] Cyrot-Lackmann F. On the electronic structure of liquid transitional metals. Advances in Physics. 1967;16:393-400.

[27] Nørskov J, Lang N. Effective-medium theory of chemical binding: Application to chemisorption. Physical Review B. 1980;21:2131.

[28] Daw MS, Baskes M. Semiempirical, quantum mechanical calculation of hydrogen embrittlement in metals. Phys Rev Lett. 1983;50:1285.

[29] Ercolessi F, Tosatti E, Parrinello M. Au (100) surface reconstruction. Phys Rev Lett. 1986;57:719.

[30] Finnis M, Sinclair J. A simple empirical N-body potential for transition metals. Philos Mag A. 1984;50:45-55.

[31] Daw MS, Foiles SM, Baskes MI. The embedded-atom method: a review of theory and applications. Materials Science Reports. 1993;9:251-310.

[32] Van Swygenhoven H. Polycrystalline materials - Grain boundaries and dislocations. Science. 2002;296:66-7.

[33] Da C. Structural modeling of nanocrystalline materials. Computational Materials Science. 1995;3:327-33.

Chapter 4: Deformation twins induced by multi-mode deformation in nanocrystalline copper

4.1 Introduction

Continuous efforts have been made for centuries to improve simultaneously both the strength and the ductility of structural materials made from metals and alloys. It is widely accepted that the generation of defects and the interaction among them, control materials' the mechanical properties of materials. Such defects include atomic vacancies and interstitials, dislocations, grain and interface boundaries, stack faults, solute atoms etc. Recently, nanoscale twin boundaries (TBs) have attracted interests following Lu’s work [1, 2] on pulsed electro-deposited nanotwinned copper. Copper with nanotwin boundaries (twin spacing less than 100nm) and ultrafine grain size (submicrometer), showed a significantly higher strength with good ductility [2-5] than its ultrafine counterpart. The deformation mechanism of nanocrystalline (NC) metals with preformed nanotwins has been investigated by molecular dynamic (MD) simulations [6-8]. These simulations showed that the impediment to dislocation slip by TBs results in an enhancement of strength, while the accommodation of dislocation slip along TBs provides considerable ductility.

As nanotwins provide materials with a combination of high strength and considerable ductility, scientists are seeking for alternative methods of producing nanotwinned ultrafine and NC metals other than electro-deposition because the later can only produce thin films. Severe plastic deformation (SPD) at high strain rate and very low temperatures has been recently investigated and shown to be able to produce bulk materials with nanoscale twins [9, 10].

A classic model [11] suggests that low temperature, high strain rate, and low stacking fault energy (SFE) help the nucleation of deformation twins (DTs) during plastic deformation and could explain the experimental results. This model also gives an inverse relationship between DT nucleation stress and grain size, which suggests that DT nucleation stress is very high when the grain size is less than 100nm. For FCC metals with medium and high SFE, it has generally been believed that the nucleation of DTs is impossible when the grain size is smaller than 1 μm. However, through the development of NC metals synthesis technology in recent years, the formation of DTs has been found to be a possible plastic deformation mechanism in NC metals after a MD prediction of DT nucleation in NC aluminum [12] with very high SFE. Recently, nanotwinning was observed in the NC structure of copper treated by surface mechanical attrition treatment (SMAT) [13]. A key feature of SMAT is that the surface of a material is mechanically deformed under high-speed impacts from random directions.

MD simulation has been widely used in investigating deformation mechanisms in NC metals. In a MD simulation, whether the deformation mechanism is dominated by a partial/full dislocation travelling through grains or by the generation of DT, may be understood on the basis of generalized planar fault energy curve (GPFE) [14]. For aluminum, with a very high SFE but a low ratio of unstable twin fault (UTF) energy barrier to SFE, formation of DTs is always observed in MD simulations. However for copper, with a much lower SFE and a much higher ratio of UTF energy barrier to SFE, formation of DTs was not expected and rarely observed in MD simulations. Several models [15-17] have been established to predict the critical stress for DT formation in NC FCC metals and to explain the competing relationship between dislocation slip and deformation twinning. Only by carefully designing the orientation of grains in a NC copper sample, can a high enough shear stress along the slip direction overcome the unstable barrier for DT nucleation [18]. In our work, a multi-mode deformation model is used in a MD simulation to generate DTs in copper with an average grain size of about 10nm. Our results show that shearing an appropriately pre-deformed NC sample could generate abundant nanotwins.

4.2 Model

A 3D NC copper sample was created by a modified Voronoi construction method developed by Chen [19]. Details of this method can be found in Section 3.3 in this dissertation. The sample contains eight grains in a 20nm×20nm×20nm cube filled with 690,000 atoms. The average grain size is 10nm and the orientations of all grains are randomly determined with no texture. In order to eliminate high internal stress and the energy of sample, an initial non-equilibrium sample was relaxed thermally to a minimum energy state with nearly no internal stress. LAMMPS was chosen as the simulation tool. The interaction between copper atoms was described by Mishin's embedded atom potential [20] which gives a SFE of 45mJ/m^2. Periodic boundary conditions were applied along all directions and the time step is set to 1fs during the whole simulation. Before applying multi-mode deformation, uniaxial compression simulations were carried out along *x*, *y* and *z* directions. From these compression tests, the highest Von Mises stress in all directions occurred at a strain of ε=4.28%, which may be considered as the elastic limit of our sample. Then the sample was compressed uniaxially at the same strain rate 10^9/s along *x*, *y* and *z* directions respectively and for each direction three different compression strains (ε =2.5, 4.28 and 5.0%) were reached. Finally, a shearing deformation of ε =30% was applied to the compressed sample along a direction orthogonal to the compression direction for 50ps. All deformations in our simulation were conducted under NVE instead of NVT ensembles and a temperature increase was observed. The microstructure of NC copper was analyzed by the common neighbor analysis method [21], which can distinguish FCC, HCP and BCC. Two adjacent HCP planes in an FCC crystal represent a partial dislocation loop confining a stacking fault while one single HCP plane represents a twin boundary. The initial atomic structure is shown in Fig. 4.1 in which grey balls represent atoms with FCC structure and black balls represent atoms with non-FCC structure such as at grain boundaries (GB).

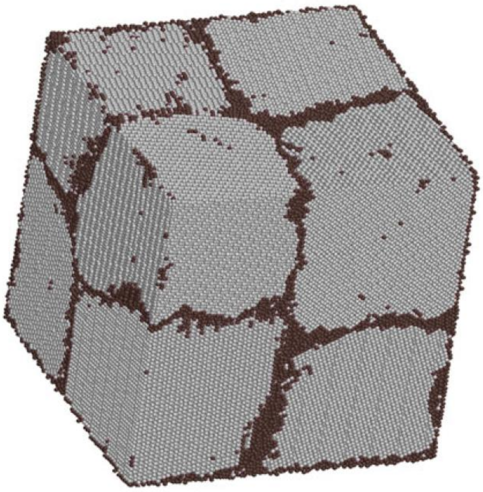

Figure 4.1. Cross-sectional view of atomic structure after thermal relaxation. Grey balls are atoms in an FCC structure and black balls are atoms in a non-FCC structure such as atoms in GBs.

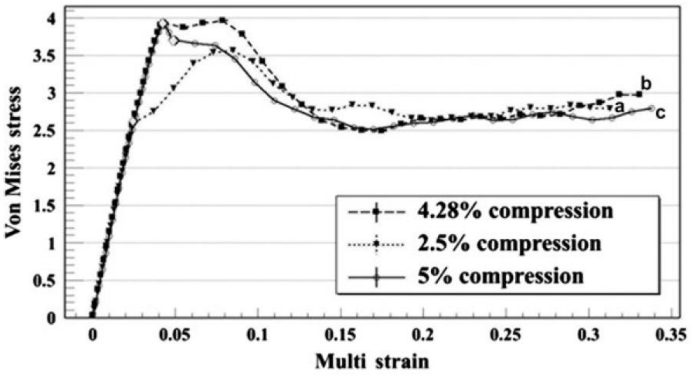

Figure 4.2. Von Mises stress versus strain curve during deformation: (a) shearing after elastic compression up to 2.5% of strain; (b) shearing after a pre-compression up to the elastic limit of 4.28%; (c) shearing after plastic compression up to 5% of strain (plastic deformation occurred). Diamond symbols indicate the start of shearing mode.

4.3 Results and Discussion

All simulations started from a uniaxial compression mode, followed by a shear mode. The von Mises stress of the sample was monitored during multi-mode deformation. The maximum value of von Mises stress at 4.28% compressive strain suggests the start of yielding and nucleation of dislocations. This critical value is generally considered as the yield strength because there is no dislocation formed before this point. Von Mises stresses as a function of strains are illustrated in Fig. 4.2, in which small diamond symbols indicate the end of the compression mode and the beginning of the shear mode. Multi-strain here is defined as the sum of the initial compression strain and the final shear strain. Shear strain is applied along a direction perpendicular to the direction of compression. Fig. 4. 2 clearly shows that the von Mises stress maintained at very high level for a while if shear deformation begins at the elastic limit; see curve (b). If the shear mode starts after yielding (curve (c)), the von Mises stress can still keep at high level for a short while. For curve (a) in which the shear mode starts after elastic compression, the von Mises stress reached a lower level after yielding as compared to other two cases. The areas under each curve represent strain energy density in the sample. It is clear that curve (b) indicates the highest strain energy stored inside the sample, followed by curve (c).

Fig. 4.3 provides a cross-section view of microstructures of the deformed samples. The sample in Fig. 4.3(a) was elastically compressed before shearing and the corresponding von Mises stress is shown as curve (a) in Fig. 4.2. Only partial dislocations were observable in this deformed sample and no DTs were found in any grains. This simulation was repeated in different directions and no DTs were formed under such multi-mode deformations. Partial dislocations were emitted from, and annihilated at, GB. GB sliding was also observed as one of the deformation mechanisms, which is similar to the observations in simple tension simulation reported previously [22].

Fig. 4.3(b) illustrates that abundant DTs were generated in a sample that was uniaxially compressed to the elastic limit and then sheared. The von Mises stress for this case is given as curve (b) in Fig. 4.2. Dense DTs with a width of one or two atomic layers were found in all grains. The same phenomenon was also found in all other samples with the same multi-mode deformation, but along different directions. The higher quantity of DTs compared to that of partials suggests that their formation was the primary deformation mechanism in this multi-mode deformation. Since the samples were prepared randomly with no texture and since simulations along different directions showed similar results, the reason for DT nucleation in Fig. 4.3(b) should not be the Schmid factor of grains. As a test, pure compression and pure shear along different directions were also simulated on the same sample and no formation of DTs was observed in each simulation as predicted by the GPFE model. Based on the behavior of von Mises stress in Fig. 4.2, one might suggest that the high elastic distortion energy and high level of von Mises stress can help to overcome the barrier of nucleation of DTs as described in the GPFE model.

Fig. 4.3(c) shows a part of the cross-section of a deformed sample that was uniaxially compressed to a yielding state followed by shearing. The corresponding von Mises stress is shown as curve (c) in Fig. 4.2. This figure indicates that some twin lamellae, as marked, were formed in the sample. Only three twin lamellae in total were found in two different grains by a detailed examination. In this case, the sample was deformed by partial dislocation movement, GB sliding and DT generation. However, DTs were not observed in a sample deformed along a different direction under the same multi-mode, indicating that DT formation may not be a primary deformation mechanism in this situation. It is quite clear that the different levels of the strain energy density immediately after the yielding point induced by different multi-mode deformations lead to different deformation mechanisms. When the strain energy density is lower, such as in case (a) in Fig. 4.2 and 4.3, the primary deformation mechanism is partial dislocation generation and GB sliding. For an intermediate level of strain energy density, such as case (c) in Fig. 4.2 and 4.3, a few DTs may be generated together with partial dislocations and GB sliding. For case (a) and (c), flow stress quickly relaxed after the yielding point because the deformation mode did not change at this moment. If the strain energy density can be maintained at a high level for a while, by changing the deformation mode at the yielding point, such as in case (b) in Fig. 4.2 and 4.3, massive amount of DTs can be generated in NC copper.

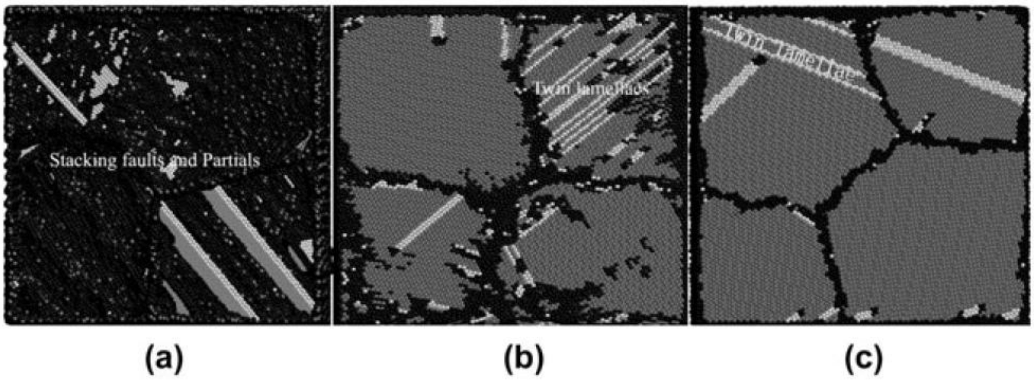

Figure 4.3. Cross-sectional views of atomic structures after multi-mode deformation. While balls represent HCP atoms, grey balls represent FCC atoms: (a) shearing after elastic compression up to 2.5% of strain; (b) shearing after a compression up to the elastic limit of 4.28%; c. shearing after plastic compression up to 5% of strain.

Our simulation results agree well with HRTEM images of SMAT-treated copper [13]. They show that a high density of DTs was formed in the NC copper after ball impacts along random directions. The strain fields generated in our MD simulations are similar to that generated under SMAT, according to a finite-element study. During SMAT, a surface element may experience both compression strain and shear strain, often not at the same time. Given enough time for deformation during SMAT, conditions may be satisfied for DT generation.

There is a question about the ensemble used in our MD simulation. Thermal equilibrium is always maintained for the NVT ensemble, which induces heat exchange with the environment and keeps system temperature constant. However, for a short time duration in the dynamic process such as SMAT, the strain rate is high (~10^4/s), and heat transfer to the environment is relatively small. The temperature of the samples under SMAT can rise by over 100K in FEM simulation and in experiments. Our MD simulation was conducted at 0K for the NVE ensemble and the sample temperature increased by about 120K. Our simulations indicate that compression up to the elastic limit followed by a large shear could be the reason for DT generation in NC copper under SMAT.

DTs are usually nucleated in NC FCC metal via a mechanism different from that proposed for their coarse-grain counterparts. Coherent twin pairs as marked in Fig. 4.3(b) are observed frequently in HRTEM observations [13] and our simulations. Several mechanisms have been proposed for twin lamellae nucleation, including the RAP mechanism [23], the dislocation rebound mechanism [24] and the self-partial multiplication mechanism [24, 25]. In our simulations, DTs as twin lamellae, which are one or two atomic layers apart, are formed via partial emissions from GBs. Two different partial-mediated mechanisms were observed in our simulation: one involves two partial dislocation slippings on adjacent close-packed planes and the other involves three non-neighboring partial slips.

Fig. 4.4 clarifies the microstructure evolution of a grain in Fig. 4.3(c) and depicts a mechanism via three partial slips. The stacking sequence evolution is illustrated in Table 4.1. Firstly, a Shockley partial dislocation, marked as A in Fig. 4.4(a), on the glide plane (111) was emitted from a GB and then ended at the opposite GB leaving an extended partial dislocation ending on either side of the grain. The original plane sequence along the orthogonal direction of the glide plane (ABCABCAB) was changed to a faulted sequence of CABABCAB; see the column for the first slip in Table 4.1. As deformation continued, another Shockley partial, marked as partial C in Fig. 4(a) was emitted from the same grain boundary. Partial A and Partial C glided parallel to each other but separated by two (111) planes. Four neighboring faulted atomic layers were formed by partial A and C, see the column for the second slip in Table 4.1. The partial B was emitted from another GB, gliding on a different slip plane and intersecting at the partial A. A full dislocation loop was formed from the junction between A and B. The full dislocation loop then split into two partial dislocations inside the faulted four HCP planes. These two partial slips, within the faulted four planes (one slip to the left and one slip to the right), transforms the faulted planes sequence from CABABABC to BCACBABAB; see the column for the third slip in Table 4.1. Finally, a twin lamella separated by two atomic layers was formed and extended across the whole grain as depicted in Fig. 4.4(d).

Table 4.1. Illustration of plane sequence evolution for a three-slip mechanism.

Original sequence	First slip	Second slip	Third slip
A	C	C	B
B	A	A	C
C	**B**	**B**	**A** TB
A	**A**	**A**	C
B	B	**B**	B
C	C	**A**	**A** TB
A	A	B	B
B	B	C	C

However, the 3-slip mechanism was observed only in deformed sample within the shear region after compression to the plastic region; it was not observed in the sample deformed to the elastic limit followed by shearing. For the latter case, a DT was formed by the glide of two partials with the same Burgers vector from the same GB on two adjacent (111) planes. This mechanism needs only two partial slips and has been proposed in previous studies. Dislocation-TB interaction, which generates mobile or sessile dislocation either in the neighboring domains or at TBs, accounts for enhancement of the strength of nanotwinned materials without significant loss of ductility.

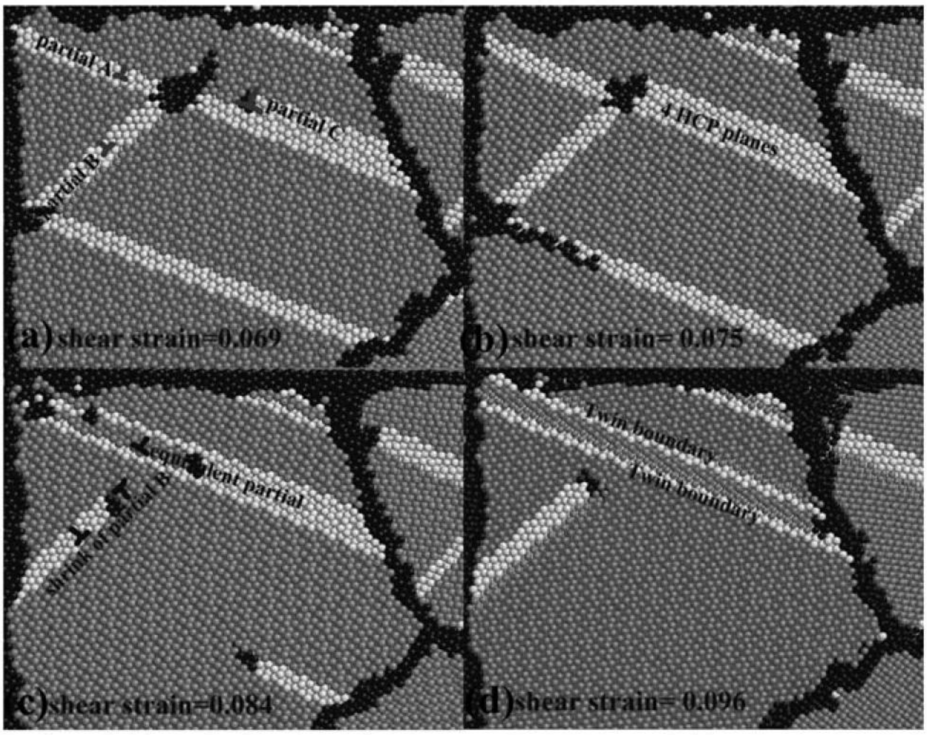

Figure 4.4. Three-step mechanism of nucleation of a twin pair via partial emissions. Grey balls represent FCC atoms, white balls represent HCP atoms and black balls represent atoms with other structure.

4. 4 Conclusion

MD simulations have confirmed that appropriate multi-mode deformation can generate a high density of nanotwins in NC copper. Shearing after compression, to the elastic limit provides the best formation condition for DT nucleation. DTs were observed to nucleate through two different mechanisms: one needs two Shockley partial glide on neighboring (111) planes and the other needs three slips. The whole process from DT nucleation to DT interaction with Shockley partials was observed in our simulation.

Reference

[1] Lu K, Lu L, Suresh S. Strengthening Materials by Engineering Coherent Internal Boundaries at the Nanoscale. Science. 2009;324:349-52.

[2] Lu L, Chen X, Huang X, Lu K. Revealing the Maximum Strength in Nanotwinned Copper. Science. 2009;323:607-10.

[3] Dao M, Lu L, Shen YF, Suresh S. Strength, strain-rate sensitivity and ductility of copper with nanoscale twins. Acta Mater. 2006;54:5421-32.

[4] Shen YF, Lu L, Lu QH, Jin ZH, Lu K. Tensile properties of copper with nano-scale twins. Scripta Mater. 2005;52:989-94.

[5] Chen XH, Lu L, Lu K. Grain size dependence of tensile properties in ultrafine-grained Cu with nanoscale twins. Scripta Mater. 2010;64:311-4.

[6] Wu ZX, Zhang YW, Srolovitz DJ. Dislocation-twin interaction mechanisms for ultrahigh strength and ductility in nanotwinned metals. Acta Mater. 2009;57:4508-18.

[7] Shabib I, Miller RE. A molecular dynamics study of twin width, grain size and temperature effects on the toughness of 2D-columnar nanotwinned copper. Modell Simul Mater Sci Eng. 2009;17:055009.

[8] Yu Q, Shan ZW, Li J, Huang XX, Xiao L, Sun J, et al. Strong crystal size effect on deformation twinning. Nature. 2010;463:335-8.

[9] Hong CS, Tao NR, Lu K, Huang X. Grain orientation dependence of deformation twinning in pure Cu subjected to dynamic plastic deformation. Scripta Mater. 2009;61:289-92.

[10] Zhao WS, Tao NR, Guo JY, Lu QH, Lu K. High density nano-scale twins in Cu induced by dynamic plastic deformation. Scripta Mater. 2005;53:745-9.

[11] Meyers MA, Vohringer O, Lubarda VA. The onset of twinning in metals: A constitutive description. Acta Mater. 2001;49:4025-39.

[12] Yamakov V, Wolf D, Phillpot SR, Gleiter H. Deformation twinning in nanocrystalline Al by molecular dynamics simulation. Acta Mater. 2002;50:5005-20.

[13] Wang K, Tao NR, Liu G, Lu J, Lu K. Plastic strain-induced grain refinement at the nanometer scale in copper. Acta Mater. 2006;54:5281-91.

[14] H. VAN SWYGENHOVEN PMDAAGF. Stacking fault energies and slip in nanocrystalline metals. Nat Mat. 2004;3:399.

[15] Kibey S, Liu JB, Johnson DD, Sehitoglu H. Predicting twinning stress in fcc metals:

Linking twin-energy pathways to twin nucleation. Acta Mater. 2007;55:6843-51.

[16] Zhu YT, Liao XZ, Srinivasan SG, Zhao YH, Baskes MI, Zhou F, et al. Nucleation and growth of deformation twins in nanocrystalline aluminum. Appl Phys Lett. 2004;85:5049-51.

[17] Zhu T, Li J. Ultra-strength materials. Prog Mater Sci. 2010;55:710-57.

[18] Wang J, Huang HC. Shockley partial dislocations to twin: Another formation mechanism and generic driving force. Appl Phys Lett. 2004;85:5983-5.

[19] Chen D. Structural modeling of nanocrystalline materials. Computational Materials Science. 1995;3:327-33.

[20] Mishin Y, Mehl M, Papaconstantopoulos D, Voter A, Kress J. Structural stability and lattice defects in copper: Ab initio, tight-binding, and embedded-atom calculations. Physical Review B. 2001;63:224106.

[21] Clarke AS, Jónsson H. Structural changes accompanying densification of random hard-sphere packings. Physical Review E. 1993;47:3975.

[22] Van Swygenhoven H, Derlet PM. Grain-boundary sliding in nanocrystalline fcc metals. Physical Review B. 2001;64:224105.

[23] X. L. Wu XZL, S. G. Srinivasan, F. Zhou, E. J. Lavernia, R. Z. Valiev, Y. T. Zhu. New Deformation Twinning Mechanism Generates Zero Macroscopic Strain in Nanocrystalline Metals. Phys Rev Lett. 2008;100:095701.

[24] Zhu YT, Narayan J, Hirth JP, Mahajan S, Wu XL, Liao XZ. Formation of single and multiple deformation twins in nanocrystalline fcc metals. Acta Mater. 2009;57:3763-70.

[25] Y. T. Zhu XLW, X. Z. Liao, J. Narayan, S. N. Mathaudhu, and L. J. Kecskés. Twinning partial multiplication at grain boundary in nanocrystalline fcc metals. Appl Phys Lett. 2009;95:031909.

Chapter 5 : Tensile deformation properties of single crystal copper with nanotwins

5.1 Introduction

Ultrafine-grained copper with embedded nano scale twins (nt copper) has attracted strong attention due to its unusually high strength compared with its conventional coarse-grained counterpart, and its better ductility and electric conductivity compared with its nanocrystalline counterpart without nano twins [1, 2]. It is well accepted that the yield strength of conventional metals increases with decreasing grain size, which is known as the Hall-Petch effect. This scaling phenomenon can be interpreted as the result of the grain boundary (GB) blocking the dislocation motion. A potential approach to the production of metals and alloys with ultrahigh strength is to reduce the grain size to nanometer scale [3, 4]. However, nanocrystalline metals produced by plastic deformation usually have very low ductility compared with their coarse-grained counterparts [4]. Research has shown that a high strength and high ductility can be achieved simultaneously by introducing twin boundaries to nanocrystalline copper [5, 6].

It has been confirmed both experimentally [5-7] and theoretically [8-13] that twin boundaries, as a special type of grain boundary, provide obstacles to dislocation motion and therefore strengthen nt copper. Unlike conventional grain boundaries, where dislocation pile-ups form, twin boundaries can react with dislocations and allow them to move through under high stress [6, 7, 9, 11, 12]. The interaction between dislocation and twin boundaries is classified by the energy barrier [11]. For a low driven force, the resultant sessile stair-rod dislocation lying on the twin boundary plane impedes further slips from dislocation. At a high driven force, stair-rod dislocation can further dissociate into partial dislocations, some of which can move away from the twin boundaries, resulting in considerable ductility in nt copper.

The fact that the plastic deformation of nt copper involves both grain boundaries and twin boundaries suggests that the strength of nt copper relies on both grain size and twin spacing (d) that represents the average distance between two neighboring twin boundaries. Similar to conventional coarse-grained copper, the strength of nt copper versus grain size follows the classical Hall-Petch relation down to a critical grain size (usually 15 nm), and then reverses (softens) when the grain size is smaller than the critical size [1, 2, 14, 15]. This phenomenon has been explained by the transition of the plastic deformation mechanism from a dislocation-based mechanism to a grain boundary based mechanism in nanocrystalline metals [4, 16-19]. The strength of nt copper with a fixed grain size has been revealed to scale with twin spacing [1, 2, 8, 14, 15]. Beyond a critical twin spacing, the strength decreases with increasing twin spacing, whereas below the critical twin spacing, nt copper softens. Molecular dynamics (MD) simulation conducted by Gao’s group [8] revealed that at this critical twin spacing, the strengthening mechanism by which twin boundaries impede dislocation motion switches to a dislocation-nucleation-controlled softening mechanism, with twin boundary migration resulting from the nucleation and motion of partial dislocations parallel to the twin boundary planes. The critical twin spacing at which the strength of nt copper reaches its maximum depends on the average grain size [20, 21].

What happens to a structure in which the average grain size is very large but the twin boundary spacing is relatively small is still unknown. This situation can occur when twin boundaries are generated by rapid deformation under suitable conditions. In this study, MD simulations were conducted on a single crystal copper with preformed twin boundaries.

The remainder of this chapter is organized as follows. The simulation method is described in section 5.2. Section 5.3 discusses the results of the simulations in detail. Section 5.4 provides some conclusions from the results.

Table 5.1. Sample lengths (z) along the z direction, twin spacings (d), and number of atoms (N)

Sample #	1	2	3	4	5	6	7	8
z(nm)	49.99	45.81	46.65	47.03	38.72	48.26	65.01	58.33
d (nm)	1.25	2.30	3.34	3.97	4.38	4.80	5.42	5.84
N (10^3)	300	275	280	285	232.5	287.5	390	350
Sample #	9	10	11	12	13	14	15	16
z(nm)	39.0	51.61	42.47	63.77	42.06	84.32	126.27	168.2
d (nm)	6.47	8.56	10.64	14.82	21.08	41.95	62.82	83.69
N (10^3)	232.5	307.5	255	380	252.5	321.6	481.6	641.6

5.2. Methodology

Samples with only twin boundaries are constructed as follows. The *x*, *y*, and *z* directions of the samples are along <110>, <$\bar{1}$12>, and <1$\bar{1}$1>, respectively, and *z* is the tensile loading direction. Three dimensional copper samples are generated by a periodically arranged <111> plane sequence along the z-direction. A standard (111) plane placed without any displacement along the y-direction is denoted as "A", a shift along the *y*-direction of plane "A" by a distance $\sqrt{6}a/6$ (*a* is the lattice constant of copper) is denoted as "B", and a plane with a displacement of $\sqrt{6}a/3$ along the *y*-direction is denoted as "C". A perfect single crystal of copper has a plane stacking sequence of ...ABCABCABC... along the *z*-direction and a single crystal of copper with two twin boundaries has the sequence...AB**C**BACBA**C**ABC..., in which the bold underlined "**C**" represent the twin boundaries. A total of 16 samples with twin spacing ranging from 1.25 nm to 83.7 nm are constructed. The lengths along the *x*- and *y*-directions for samples #1~13 are 11.07 nm and 6.36 nm, respectively, and for samples #14~16 are reduced to 8.89 nm and 5.14 nm, respectively. The sample lengths along the *z*-direction, the twin spacing, and the number of atoms are listed in Table 5.1. The periodic condition is applied to all directions.

The embedded atom model (EAM) potential [22] is applied to describe the atomic interactions in the copper. The samples are thermally relaxed first so that all of the stress components except for the shear component in the *xy*-plane reach values very close to zero. The considerable shear component (τ_{xy}) suggests that the twin boundaries can induce pure shear back stress in the samples. The Large-scale Atomic/Molecular Massively Parallel Simulator (LAMMPS) developed by Sandia is used for the simulation [23]. The uniaxial tensile along the *z*-direction is simulated for 300 ps at a strain rate of 10^9/s by means of rescaling the box size every 0.4 ps and maintaining the temperature of the system at 300 K. The microstructure of the samples is analyzed by the Ackland method [24]. This method can distinguish the FCC, HCP, BCC, and other relatively close-packed structures. Two typical defects in twinned single crystal copper are examined: stacking faults (two adjacent HCP planes in an FCC structure) and twin boundaries (a single HCP plane in an FCC structure).

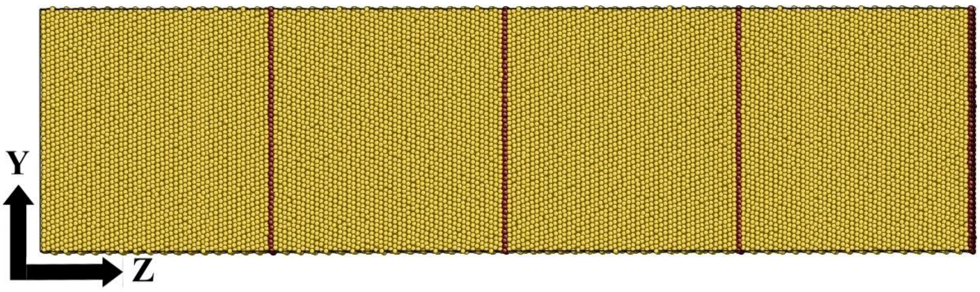

Figure 5.1. Cross-section of nano twinned single copper with a twin spacing of 10.65nm: the yellow dots represent the FCC atoms and the red dots represent the HCP atoms.

5.3. Results and discussion

5.3.1 Initial stage of plastic deformation

In real experiments, dislocation can be generated from sample free surfaces or other defects such as incoherent grain boundaries and inclusions. In this simulation, the only pre-existing defect is the coherent twin boundary with periodic boundary condition in all three directions. Our simulations demonstrated that in this ideal situation, dislocations cannot nucleate at the coherent twin boundary. Dislocation loop were formed through point defect clustering.

Fig. 5.1 shows a cross-sectional view of the relaxed structure of a nanotwinned sample with a twin spacing of 10.64 nm. The lines formed by the red dots in Fig. 5.1 are the twin boundaries on the *yz*-plane. The atoms on the twin boundaries form an HCP-like structure. Perfect FCC crystals without defects are confined by the twin boundaries and have mirror symmetry with respect to the twin boundaries. Tensile forces are applied at a constant temperature of 300 K along the z-direction, which is perpendicular to the twin boundaries. In all of the simulations, the observed plasticity consists of dislocation nucleation and motion, the generation of deformation twins, and twin boundary migration as a result of dislocation interaction.

To monitor the dislocation nucleation process, a detailed microstructure analysis is conducted every picosecond on the structural configuration around each atom. By removing the FCC structured atoms from the crystal, the evolution of all of the defective atoms (atoms that do not have an FCC structure symmetry) can be seen at each stage of the deformation.

At an early stage, randomly distributed defective atoms appear in the bulk between the two twin boundaries for all of the samples with different twin spacings. Each defective atom induces local displacements of neighboring atoms along the <112> crystal direction. Such displacements from the equilibrium positions change the local structure from FCC- to HCP-like. Thus, in the following, we call these defective atoms HCP atoms.

Assuming that the formation energy of such HCP atoms is Q, one can express the concentration (atomic fraction) of such defects using an Arrhenius-like relation (see Eq. 5.1). Here, the energy barrier of the formation is reduced by the applied strain energy:

$$c = \frac{n}{N} = \eta \exp\left(-\frac{Q - \sigma V^*}{kT}\right) \qquad \text{Eq. 5.1}$$

where n is the number of HCP atoms and N is the total number of atoms, η is a pre-exponential factor, V^* is the activation volume of one defect, and σ is the applied hydrostatic stress. We approximate the applied hydrostatic stress by the flow stress calculated from the simulations. Fig. 5.2 shows the von Mises stress as a function of strain from a typical MD simulation. The relationship between the von Mises stress and strain remains quite linear in the elastic regime up to a maximum value before a sudden drop. Also shown in this figure is the population of HCP defects as a function of the strain. We do not include these initial HCP atoms in the twin boundaries. The relationship given in Eq. 5.1 is most suitable for the portion of the concentration curve from A to B. The flat region of the curve before point A is determined by $1/N$ (where N is the total atoms number). By fitting Eq. 5.1 to the line AB on the concentration curve, we can determine the constants η, V^*, and Q, respectively.

The Arrhenius relation 5.1 is only good until a maximum strain of about 7.4% (point B on the AB line in Fig. 5.2). During this period of deformation, there is no dislocation being created, as can be seen in Fig. 5.3(a) and (b). A detailed microstructure analysis at point B shows that HCP atom-pairs start to appear. A rapid increase in the concentration of the HCP atoms is observed from 7.4% to 7.8%, and at the end of this increase small HCP “plates” are formed inside single crystals between the twin boundaries as a result of the clustering of the HCP atoms (see Fig. 5.3(c)). These “plates” are stacking faults enclosed by partial dislocations, and are called dislocation loops. Once the dislocation loops are formed and grow, the von Mises stress quickly drops beyond a strain of 7.8%. The peak stress in Fig. 2 can be considered the ideal yield strength for pure single crystals of copper, which agrees well with ab initio prediction [25].

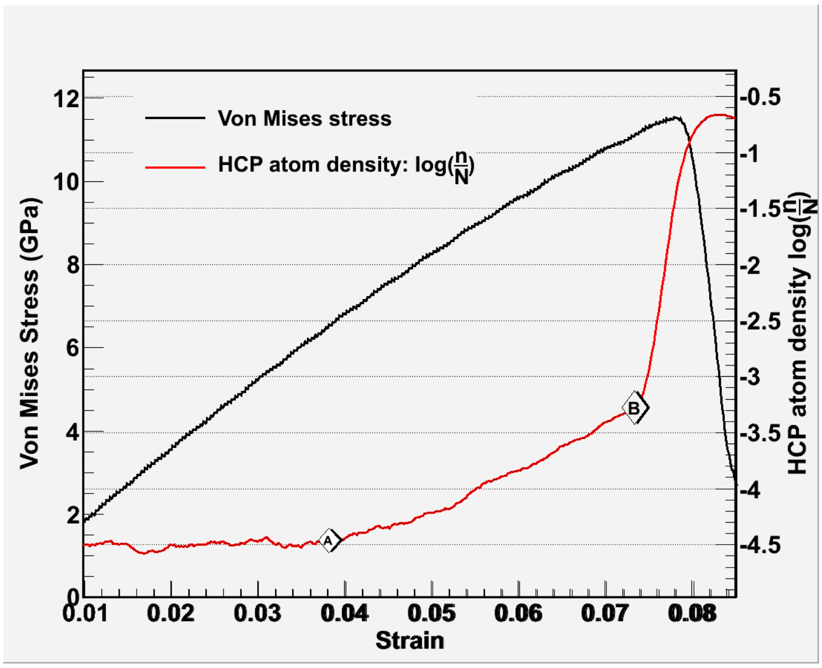

Figure 5.2. Von Mises stress and HCP atom concentration as a function of strain in nanotwinned single crystal copper with a twin spacing of 21.08 nm.

This observation suggests that perfect twin boundaries do not generate very high stress concentrations nearby due to their rather low excess energy compared with normal grain boundaries. Because we start the simulation with nearly perfect crystals, the dislocation loops can only be generated by a homogeneous nucleation process that involves point defect clustering, which is a much more difficult process than in real crystals, in which crystal defects are often present. It is observed in this work that dislocation loops are often created in close vicinity, such that they grow into intercepting loop clusters. Fig. 5.3(d) shows that multiple dislocation loops intercept each other during their growth.

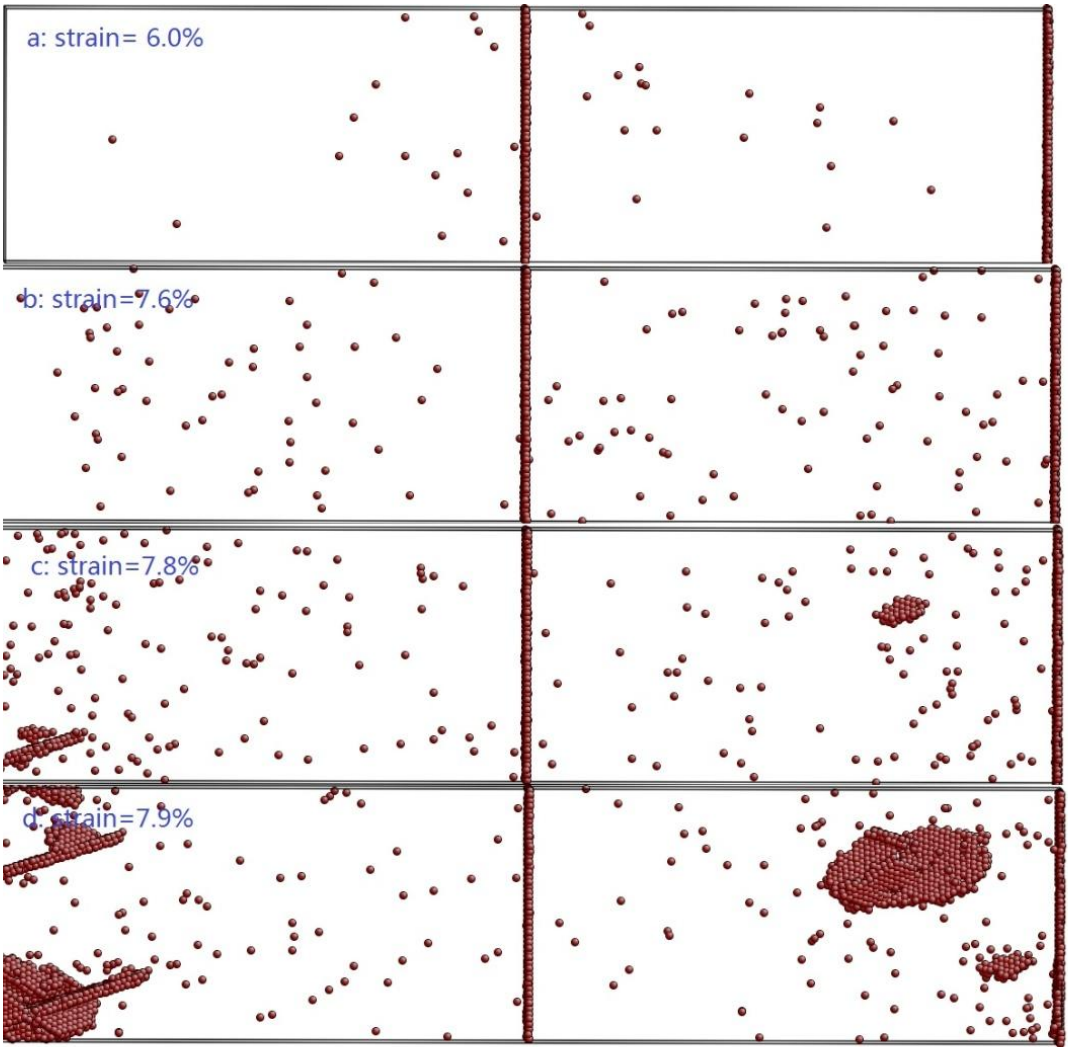

Figure 5.3. HCP defective atoms in nano twinned single crystal copper with a twin spacing of 21.08 nm at different strains: (a) 6.0%; (b) 7.6%; (c) 7.8%; (d) 7.9%.

5.3.2 Plastic deformation

After the nucleation of the dislocation loops, the microstructure evolution involves the slip of partial dislocations (loop growth), interaction between dislocation loops, and interaction between loops and twin boundaries. To illustrate the slip systems in the nano twinned structure, Thompson tetrahedrons are shown in Fig. 5.4.

Fig. 5.4 shows a pair of Thompson tetrahedrons that correspond to the original FCC structure and twinned FCC structure, respectively. The four vertices of the upper tetrahedron are labeled A, B, C, and D. The middle points of the triangles are denoted α, β, γ, and δ, respectively. Symbols with the superscript T represent points on the twinned FCC structure. The ACB plane is the twin boundary. The upper and lower Thompson tetrahedrons ABCD and $A^TB^TC^TD^T$ illustrate the slip systems of crystals on both sides of the twin boundaries. The four (111) slip planes in the upper tetrahedron are defined as BCD, CAD, ABD, and ACB. Similarly, in the lower tetrahedron $A^TB^TC^TD^T$, there are four slip planes that are the mirror planes of those in the upper tetrahedron, for example, $B^TC^TD^T$ is the mirror plane of BCD, and so on. Taking plane BCD as an example, three Shockley partials are denoted αB, αC, and αD, respectively. Two Shockley partials react to form a full dislocation by following reaction $\alpha B + C\alpha = CB$, in which CB denotes a full dislocation.

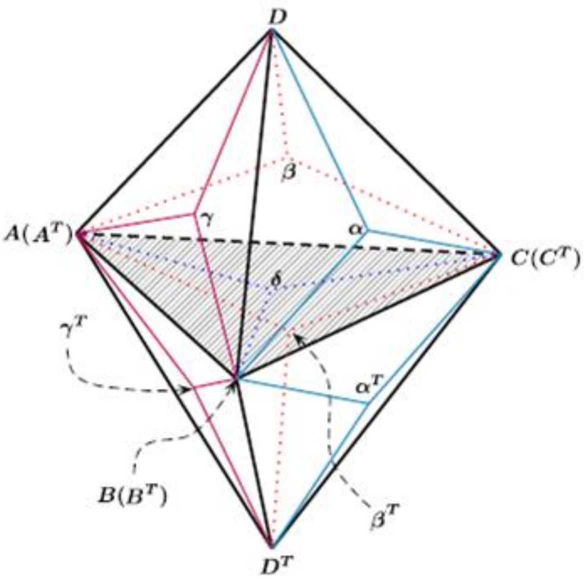

Figure 5.4. FCC twin octahedron formed by two Thompson tetrahedrons.

In this work, twin boundaries are created parallel to the plane ABC in Fig. 5.4, and the loading direction is perpendicular to this plane. The dislocation nucleation mechanism is examined by the ACLAND method [24]. Previous studies indicate that randomly generated HCP atom clusters create “seeds” of dislocation loops. For small twin spacings, one side of the loops reaches a twin boundary very soon, leaving behind half loops that enclose stacking faults. Fig. 5.5 shows one Shockley partial dislocation loop (two half loops) confining a stacking fault area. The edge of the stacking fault is the curved partial dislocation line. A similar half loop-stacking fault configuration has also been found in nanocrystalline MD simulations [26], in which it is very hard to find a full partial dislocation loop inside a nano-sized grain. The difference in nanocrystalline copper compared with a nanotwin structure is that the partial dislocations are nucleated at the grain boundaries rather than inside the grains. When the twin spacing is large (or the grain size is large) the chance of creating a full partial dislocation loop or a leading partial followed by a trailing partial is increased.

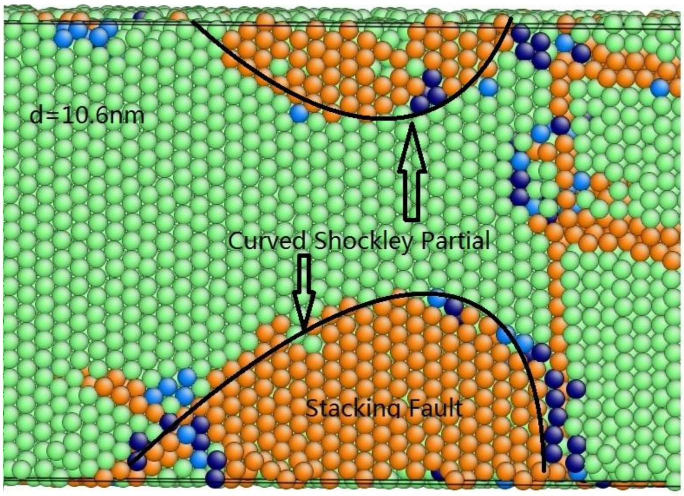

Figure 5.5. Stacking faults and Shockley partial dislocations in nano twinned single crystal copper.

Fig. 5.6 compares the dislocation configurations for different twin spacings. It can be seen that at small twin spacings (such as d = 5.42 nm), most partial dislocation loops run across the whole grain and stop at the two twin boundaries. Most of the partials connect with stacking faults. Deformation twins (a single atomic plane with an HCP configuration) are rare. In contrast, at large twin spacings (such as d = 84 nm), some partials have not yet reached the twin boundaries, and deformation twins are clearly visible.

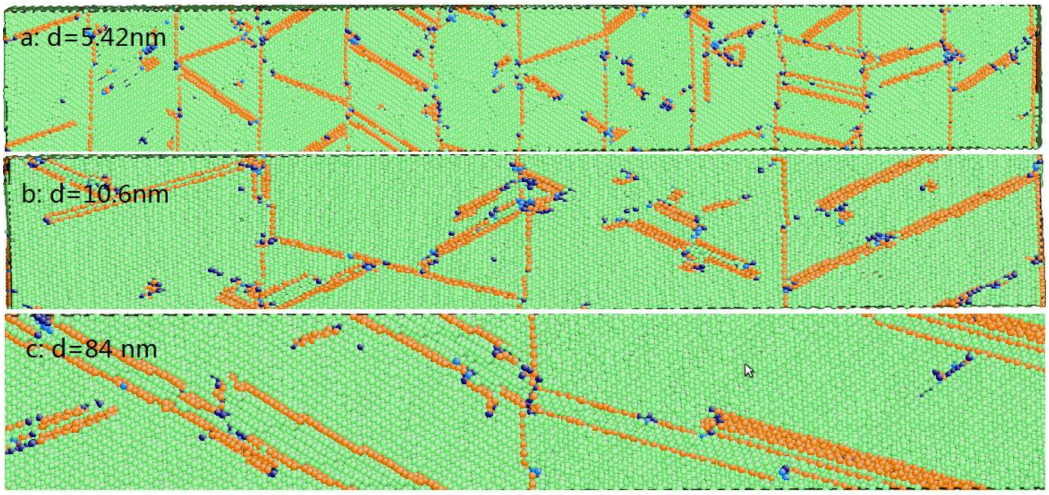

Figure 5.6. Cross-sectional views of the microstructure of nano twinned single crystal copper with different twin spacings (the three crystals are not at the same length scale). Green represents the FCC structure and brown represents the HCP structure. One atomic plane in brown represents the deformation twins and twin boundaries.

The reaction between a partial dislocation and a twin boundary can be depicted by a Thompson tetrahedron, as shown in Fig. 5.4. For instance, a 90^{o} partial dislocation $D\gamma$ (in our simulation, all of the partials are along the direction perpendicular to the intersection line between the glide plane and the twin boundary) in the upper tetrahedron glides on the slip plane DAB toward twin boundary ABC. When $D\gamma$ on plane DAB reaches ABC, the cross-slip of $D\gamma$ becomes possible and produces a partial slip on plane ABC, which induces the migration of twin boundary ABC. In our simulation, it is quite frequent to observe steps on the twin boundaries and twin boundary migration. However, the transmission of a partial $D\gamma$ needs to overcome a higher energy barrier, because the process requires $D\gamma$ to be dissociated into a full dislocation DB and another partial dislocation $B\gamma$ according to

$$D\gamma = DB + B\gamma \qquad \text{Eq. 5.2}$$

The energy barrier for Eq. 5.2 is proportional to $3b^2$, where b is the Burgs vector of a Shockley partial, which is rather high. Thus, the twin boundary effectively stops the movement of the dislocations, resulting in an ultra high flow strength of nano twinned copper. The second step of the transmission of a partial $D\gamma$ across twin boundary ABC is described by Eq. 5.3, the energy barrier of which is only a third that of Eq. 5.2.

$$DB = C^T D^T + A\delta \qquad \text{Eq. 5.3}$$

This reaction induces a partial dislocation $A\delta$ on twin boundary ABC and a full dislocation C^TD^T in the lower tetrahedron in Fig. 5.4. The partial $A\delta$ on the twin boundary also results in a one-atom layer migration of the twin boundary. The energy barrier for this reaction is proportional to b^2 with the same parameters as in Eq. 5.2. When the new full dislocation starts to move in the bulk, it spontaneously dissociates into two Shockley partial dislocations on plane $\mathrm{B^TC^TD^T}$. The whole process of partial dislocation transmission through the twin boundary requires a high energy in proportion to $4b^2$.

As shown in Fig. 5.6, new twin boundaries represented by a single HCP atom plane are observed in samples with d=10.6 nm and 84 nm. It is well known that deformation twinning and dislocation are competitive plastic deformation mechanisms in copper. MD simulations [27] have revealed that deformation twinning via partials emitted from the grain boundary is not favored in nc copper. However, as discussed in section 5.3.1, the nucleation of the dislocation in our samples is different from that in nc copper. Rather than being emitted from the boundaries, dislocations are formed in the bulk of our samples right at the yielding point. The dislocations in the bulk do not glide on all of the parallel {111} planes. It is possible for dislocations to react with another dislocation on an inclined slip plane in the bulk. Thus, deformation twinning may be formed through a dislocation rebound mechanism. Fig. 5.7 shows the formation of twin lamella through a dislocation rebound mechanism.

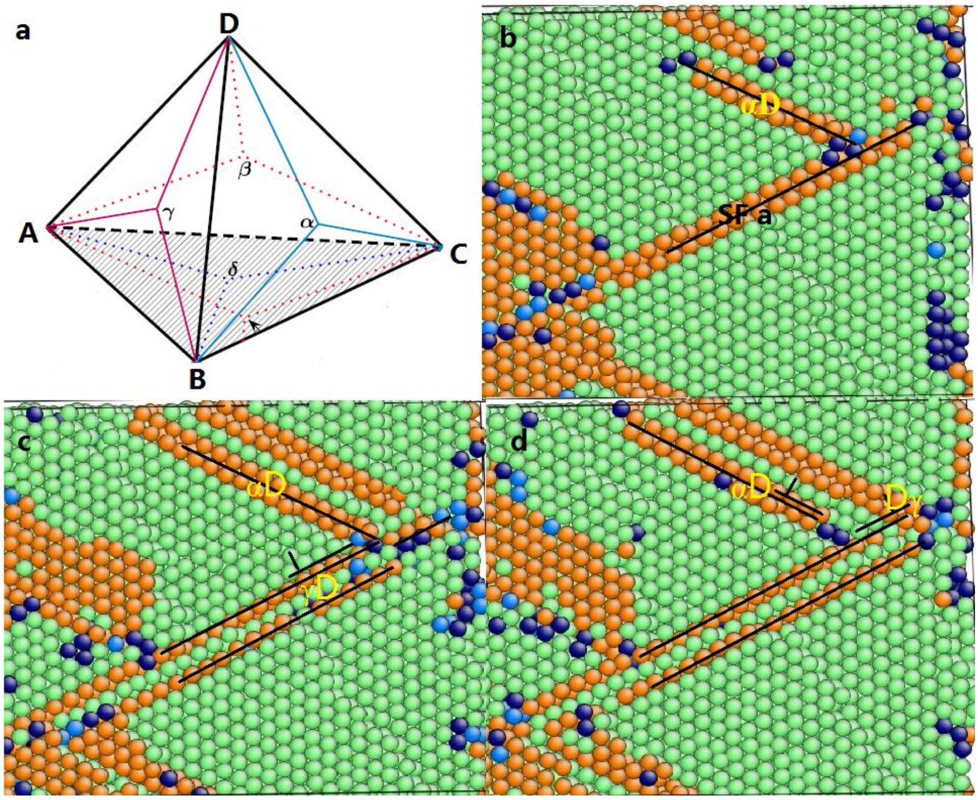

Figure 5.7. Deformation twinning process in a sample with d=10.6nm. (a) Thompson tetrahedron; (b) a partial meets a stacking fault 'a'; (c) $\alpha D=\alpha\gamma+\gamma D$; (d) $\alpha\gamma=\alpha D+D\gamma$.

In Fig. 5.7(b), the Shockley partial αD glides toward stacking fault “a”. A reaction then takes place to generate a stair-rod dislocation and another Shockley partial γD:

$$\alpha D = \alpha\gamma + \gamma D \quad \text{Eq. 5.4}$$

The energy barrier for this reaction is proportional to b^2. After this reaction, γD glides on stacking fault "a", inducing the formation of a twin lamella with a width of one atomic layer, as illustrated in Fig. 5.7(b). The stair-rod dislocation αγ can be further dissociated into two Shockley partials as in Eq. 5.5:

$$\alpha\gamma = \alpha D + D\gamma \quad \text{Eq. 5.5}$$

Here new "αD" pushes the old "αD" back, as indicated in Fig. 5.7(c) and (d). The required twinning stress for this reaction is obtained from energy balance during the slip of the twin partial $D\gamma$:

$$\tau_T = \tau_0 + \frac{Gb^2}{6\pi(1-v)bd}\ln(\frac{d\sqrt{2}}{a}) \quad \text{Eq. 5.6}$$

in which G is the shear module, b is the Burgs vector for a Shockley partial of copper, d is the twin spacing, a is a lattice constant, and v is the Poisson's ratio. Eq. 6 indicates that the twin stress decreases with increasing twin spacing d. The deformation twinning should prevail in the samples with a large twin spacing. The stacking fault area and twin boundary area per unit volume are counted in several samples with different twin spacings. A stacking fault consists of two HCP atomic layers, and each atom in a stacking fault has six neighboring HCP atoms. The twin boundaries consist of only one HCP atomic layer confined by FCC atoms, and each atom in a twin boundary has only three neighboring atoms with the HCP structure. Thus, the areas of the stacking fault and twin boundaries are obtained and time-averaged after yielding. Fig. 5.8 shows that the area of the twin boundaries increases with increasing twin spacing. For d<5.42nm, the average new twin boundary area is zero, therefore, those data points are not added in Fig. 5.8. In fact, when d<8nm, no stable deformation twin was observed. This observation agrees well with our earlier discussions.

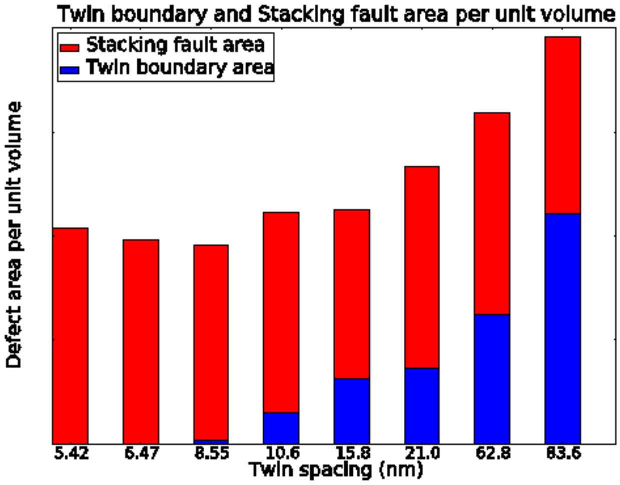

Figure 5.8. Stacking fault area and twin boundary area per unit volume versus twin spacing.

5.3.3 Strength

Our earlier discussion shows that for a nearly *perfect* crystal with only twin boundaries, the apparent yield stress is very high due to the lack of defects for the nucleation of the dislocations.

Fig. 5.9 describes the flow stress versus strain curves for eight of the samples. The strength of the *copper* is defined by the time-averaged von Mises stress after yielding. The relationship between the flow strength and twin spacing is illustrated in Fig. 5.10. The strength of nano twinned single crystal copper increases when the twin spacing decreases until the space is just a couple of nanometers. This curve can be well fitted to the Hall-Petch relationship: $\sigma_s = \sigma_0 + k_T / \sqrt{d}$ where σ_s is the flow strength (GPa) and d is the twin spacing (nm). σ_0 and k_T are fitting constants with values of 1.84 GPa and 3.016 GPa nm$^{0.5}$, respectively. This relationship is different from that of other MD simulations [8, 17] and experiments [1, 2, 4] on polycrystalline copper, in which the flow strength decreased when the twin spacing was below a critical value. The apparent softening at small twin spacings can be attributed to the fact that dislocation movements along the twin boundaries became dominant, which resulted in de-twinning. This mechanism requires the presence of normal grain boundaries, which play the role of generating or absorbing dislocations. In our simulations, there is no normal grain boundary, and thus the softening is not observed. The strengthening is due to the interaction of inclined partial dislocations with the twin boundaries. This can be proved by the following simple discussion.

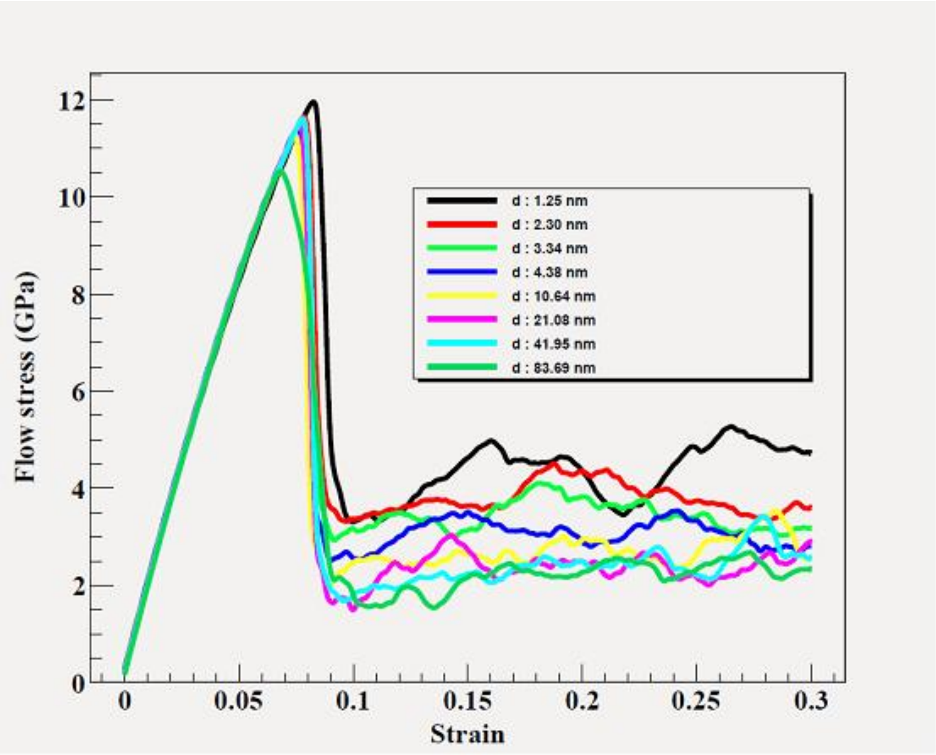

Figure 5.9. Flow stress versus strain for eight samples.

As shown in Fig. 5.11, a 90^o partial dislocation with a Burgs vector of b is formed between two twin boundaries denoted as two straight vertical lines.

The distance from the dislocation to one twin boundary is x and to the other twin boundary is d-x. The forces that the twin boundaries impose on the partial can be estimated as the forces between this partial and two imaginary partials A and B that are at mirror positions about the two twin boundaries, denoted as F_A and F_B. The sum of the work done by F_A and F_B is zero during the movement for the partial. Thus, the averaged shear stress applied by the external load can be evaluated from the energy balance condition, that is, the work done by the shear stress is equal to the sum of the increases in the stacking fault energy and dislocation energy, plus the work done by the frictional force on the moving dislocation.

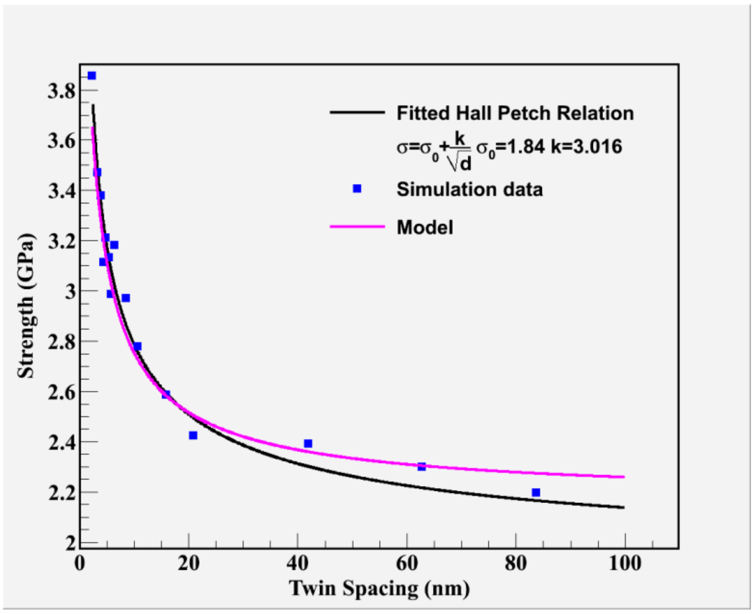

Figure 5.10. Strength versus twin spacing: simulation, fitted, and model.

The work done by the shear stress W_τ is:

$$W_\tau = \Delta x L \tau b \qquad \text{Eq. 5.7}$$

and the dislocation energy increase $\Delta_{dislocation}$ is

$$\Delta_{dislocation} = 2\Delta x \frac{Gb^2}{4\pi(1-\upsilon)} \ln(\frac{d\sqrt{2}}{a}) \qquad \text{Eq. 5.8}$$

Here, we assume that the width of the stacking fault *L* equals the twin spacing *d*. The increase in the stacking fault energy is:

$$\Delta_{SF} = \gamma d \Delta x \qquad \text{Eq. 5.9}$$

where γ is the stacking fault energy, γ=45 mJ/m^2 for copper. Thus, the energy balance condition requires:

$$W_\tau = \Delta_{dislocation} + \Delta_{SF} + W_f \qquad \text{Eq. 5.10}$$

Here, W_f is the work done by the frictional force on a moving dislocation, which is a constant value when the moving velocity of the dislocation is constant. The shear stress required for the movement of a partial dislocation in single crystal copper is obtained from Eq. 5.10:

$$\tau = \tau_{ideal} + \frac{Gb}{2\pi d(1-\upsilon)} \ln(\frac{d\sqrt{2}}{a}) \qquad \text{Eq. 5.11}$$

where τ_{ideal} is the sum of the last two terms in Eq. 5.10 and can be considered as the averaged flow stress of a perfect copper with the same geometry, which is about 2.2 GPa in this simulation. Applying all of the material parameters to Eq. 5.11 and plotting it on Fig. 5.10 shows the good agreement between this model and the simulation data.

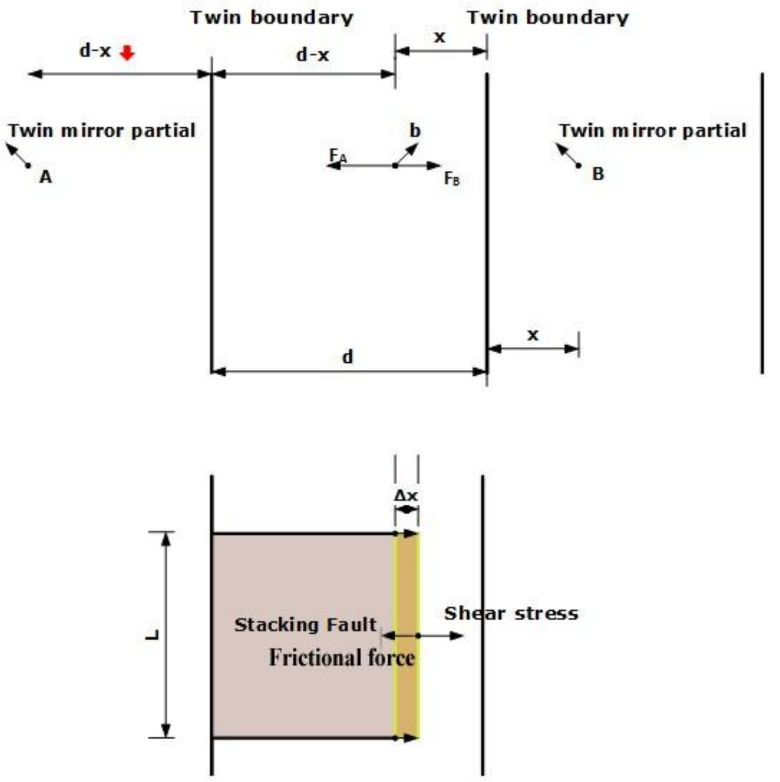

Figure 5.11. Dislocation model of a nano twinned single crystal.

5.4. Conclusion

MD simulations of uniaxial tensile loading along the <111> direction of nano twinned single crystal copper are presented.

- Partial dislocations are nucleated from HCP defective atom clusters formed by tensile loading in an originally nearly defect-free crystal structure (in which only twin boundaries are present).
- The morphology of the dislocations varies with the twin spacing: at small twin spacings (<10 nm), partial dislocations with stacking faults are the dominant defect, but when the twin spacing increases, secondary twin boundaries (deformation twins) start to form and the amount of deformation twins increases.

- The original twin boundary serves as an obstacle to dislocation movements on the glide planes tilted to the twin boundary, resulting in an enhanced flow strength.
- No softening is observed in the nearly perfect crystal. The Hall-Petch like relationship is still valid down to very small twin spacings (~1 nm), which can be explained by a simple energy balance model.

References

[1] Lu L, Shen YF, Chen XH, Qian LH, Lu K. Ultrahigh strength and high electrical conductivity in copper. Science. 2004;304:422-6.

[2] Lu K, Lu L, Suresh S. Strengthening Materials by Engineering Coherent Internal Boundaries at the Nanoscale. Science. 2009;324:349-52.

[3] Gleiter H. Nanostructured materials: basic concepts and microstructure. Acta Mater. 2000;48:1-29.

[4] Meyers MA, Mishra A, Benson DJ. Mechanical properties of nanocrystalline materials. Prog Mater Sci. 2006;51:427-556.

[5] Liu GZ, Tao NR, Lu K. 316L Austenite Stainless Steels Strengthened by Means of Nano-scale Twins. Journal of Materials Science & Technology. 2010;26:289-92.

[6] Y. T. Zhu XLW, X. Z. Liao, J. Narayan, S. N. Mathaudhu, and L. J. Kecskés. Twinning partial multiplication at grain boundary in nanocrystalline fcc metals. Appl Phys Lett. 2009;95:031909.

[7] Wang YB, Sui ML. Atomic-scale in situ observation of lattice dislocations passing through twin boundaries. Appl Phys Lett. 2009;94:3.

[8] Li X, Wei Y, Lu L, Lu K, Gao H. Dislocation nucleation governed softening and maximum strength in nano-twinned metals. Nature. 2010;464:877-80.

[9] Wu ZX, Zhang YW, Srolovitz DJ. Dislocation-twin interaction mechanisms for ultrahigh strength and ductility in nanotwinned metals. Acta Mater. 2009;57:4508-18.

[10] Shabib I, Miller RE. A molecular dynamics study of twin width, grain size and temperature effects on the toughness of 2D-columnar nanotwinned copper. Modell Simul Mater Sci Eng. 2009;17:055009.

[11] Jin ZH, Gumbsch P, Albe K, Ma E, Lu K, Gleiter H, et al. Interactions between non-screw lattice dislocations and coherent twin boundaries in face-centered cubic metals. Acta Mater. 2008;56:1126-35.

[12] Jin ZH, Gumbsch P, Ma E, Albe K, Lu K, Hahn H, et al. The interaction mechanism of

screw dislocations with coherent twin boundaries in different face-centred cubic metals. Scripta Mater. 2006;54:1163-8.

[13] A. G. Frøseth PMD, and H. Van Swygenhoven. Grown-in Twin boundaries affecting deformation mechanisms in nc-metals Appl Phys Lett. 2004;85:5863.

[14] Jinyu GUO KW, Lei LU. tensile properties of Cu with Deformation Twins Induced by SMAT. Journal of Materials Science & Technology. 2006;22(6):789.

[15] Shen YF, Lu L, Lu QH, Jin ZH, Lu K. Tensile properties of copper with nano-scale twins. Scripta Mater. 2005;52:989-94.

[16] Yamakov V, Wolf D, Phillpot SR, Mukherjee AK, Gleiter H. Deformation-mechanism map for nanocrystalline metals by molecular-dynamics simulation. Nature Materials. 2004;3:43-7.

[17] Schiotz J. Atomic-scale modeling of plastic deformation of nanocrystalline copper. Scripta Mater. 2004;51:837-41.

[18] Horstemeyer MF, Baskes MI, Plimpton SJ. Length scale and time scale effects on the plastic flow of fcc metals. Acta Mater. 2001;49:4363-74.

[19] Cheng S, Stoica AD, Wang XL, Ren Y, Almer J, Horton JA, et al. Deformation Crossover: From Nano- to Mesoscale. Phys Rev Lett. 2009;103:4.

[20] Wei Y. Scaling of maximum strength with grain size in nanotwinned fcc metals. PHYsical Review B. 2011;83:132104.

[21] Zhu L, Ruan H, Li X, Dao M, Gao H, Lu J. Modeling grain size dependent optimal twin spacing for achieving ultimate high strength and related high ductility in nanotwinned metals. Acta Mater. 2011;59:5544-57.

[22] Mishin Y, Mehl MJ, Papaconstantopoulos DA, Voter AF, Kress JD. Structural stability and lattice defects in copper: Ab initio, tight-binding, and embedded-atom calculations. Physical Review B. 2001;63:16.

[23] Plimpton S. Fast Parallel Algorithms for Short-Range Molecular Dynamics. Journal of Computational Physics. 1995;117:1-19.

[24] Ackland GJ, Jones AP. Applications of local crystal structure measures in experiment and simulation. PHYsical Review B. 2006;73:054104.

[25] Ogata S, Li J, Yip S. Ideal pure shear strength of aluminum and copper. Science. 2002;298:807-11.

[26] Chen K, Shi S, Lu J. Deformation twin induced by multi-mode deformation in nanocrystalline copper. Philos Mag Lett.

[27] Van Swygenhoven H, Derlet PM, Froseth AG. Stacking fault energies and slip in nanocrystalline metals. Nat Mater. 2004;3:399-403.

Chapter 6: Plastic deformation due to interfacial sliding in amorphous/crystalline nanolaminates

6.1. Introduction

“The smaller, the stronger” is a well-accepted concept in the materials scientific community. Recent promising developments in the manipulation of metal structures at the nano scale offer diverse approaches for achieving ultrahigh-strength materials [1]. An interesting approach is to create interfaces with nano-scale spacing in metals [2, 3]. Such interfaces can limit dislocation motion to the nano scale volume, thus exerting ultrahigh resistance to dislocation slip and inducing ultra-high strength. Examples of such bulk metallic materials include nanocrystalline [1] and nanotwinned metals [2], metallic nanolaminates [4] and so forth. The mechanical properties, most importantly the ductility/brittleness, of such materials strongly depend not only on the size of their microstructural features, but also on the properties of their interfaces [5-9]. Molecular dynamics (MD) has revealed preliminary dislocation structures in the grain boundaries of nanocrystalline metals [1] and bimetal interfaces in nanolaminates [8]. It is no surprise, therefore, that dislocation always nucleates at the interfaces in both nanocrystalline metals and nanolaminates. However, the grain boundaries and bimetal interfaces of the two materials are dissimilar. The grain boundary (GB) in nanocrystalline materials can carry considerable plastic deformation via grain boundary sliding, dislocation nucleation and annihilation [1, 10-12]. In contrast, while metallic nano-laminates are always high in strength, they are quite brittle because the bimetal interfaces with no coherency are unable to transmit dislocations at low stress level. This induces high-density dislocation pile-ups, which inhibits further plastic deformation and results in fractures at these interfaces [5, 9]. Twin boundaries (TBs) are another example of interfaces that possess high strength and considerable ductility. TBs not only exert a repulsive force on moving dislocations, but also allow them to penetrate or slide on the boundaries if the conditions are suitable [13-15]. It can be concluded, therefore, that the ability of an interface to release concentrated local stress via interfacial sliding or the transmission of plastic events is crucial for maintaining ductility.

A recent study showed that a macroscopic-sized nanolaminate with alternating 5-nm-amorphous $Cu_{\approx 3}Zr$ layers and 35-nm-nanocrystalline copper layers had high strength of about 1 GPa and almost ideal plasticity [16]. The MD simulations in that study revealed that amorphous/crystal interfaces (ACIs) play a significant role during deformation: in bulk metallic glass (BMG), dislocations in the crystal are transformed into shear transformation zones (STZs) at the ACIs, which accounts for the ideal plasticity [16]. It has been reported that the ultimate tensile strength decreases as the thickness of the amorphous layer decreases below about 100 nm [17], due to the size dependence of the suppression of shear localization. However, another MD simulation showed that a shear band can form in extremely thin amorphous layers under uniaxial compression [18]. The role of ACIs in this size dependence of shear localization remains unclear. Unlike other interfaces, the ACIs in such materials should have some unique features because the structures on the two sides of the interface are different: one side has an ordered structure and the other an amorphous structure. MD simulation identified similar complex interface dislocation structures at the ACI with a bimetal interface, which were confirmed to be closely linked to interfacial shear [19]. It was also reported that the composition gradient of the ACI extended from the amorphous layer across the interface into the crystalline layer [19]. As the structural features of the amorphous layer are identical to those of BMG, the ACI should be a common interface in BMG-based composites containing nano crystals. Investigation of the ACI may help to understand the mechanical properties of BMG-based composites. A deformation map of the dislocation emission and annihilation at the ACI and the transformation from dislocation to STZ was preliminarily illustrated by Wang et al. [16] and further elaborated by others [18, 20]. However, the structural change of the amorphous layer induced by the presence of an ACI has not been fully studied and the effect of such a change on the deformation of the amorphous layer remains unclear.

In this chapter, we investigated the ACI and its response to pure shear deformation using MD simulations. The results confirm that interfacial sliding at the ACI is an important plastic deformation mechanism. In addition, a new mechanism, the thickening of a micro-sliding band, is presented and atomistic insights into the BMG deformation mechanism are developed. The remainder of the chapter is organized as follows. Section 6.2 describes the simulation details, Section 6.3 discusses the results of the simulations in detail and Section 6.4 provides the conclusions.

6.2. Methodology

The simulations were performed in the LAMMPS [21] molecular dynamics simulator. The atomic interactions between Cu and Zr atoms are described according to the embedded atom method (EAM) potential, as developed by Cheng [22], which was optimized for varieties of Cu-Zr-Al BMGs and intermetallic systems. Two samples were prepared following two distinct thermodynamic treatments with periodic boundary conditions in all directions. The first sample was separately quenched (S1) and prepared by thermal relaxing from an original configuration of alternating layers of crystal copper and nanoglass. Nanoglass layers were formed by combining several well-quenched small samples of $Cu_{46}Zr_{54}$ BMG. A small BMG piece was prepared using the melt quench procedure. First, we randomly replaced Zr atoms with a probability of 54% in a copper crystal, with periodic boundary conditions set for all directions. This small system was rapidly quenched from 1600 K to 0 k in 16 ns with a cooling rate of 10^{11} K/*s*. The thicknesses of the crystal layer and nanoglass layer were 16 nm and 10 nm, respectively, along the z direction. The other dimensions were all 20 nm, which was sufficient to eliminate size effects on both the crystalline and the amorphous layer along the x- and y-directions. The crystalline directions of the copper layer were $[\bar{1}\bar{1}2]$, $[1\bar{1}0]$ and $[111]$ along the x, y and z directions, respectively. The sample geometry is illustrated in Fig. 6.1. A relaxation of S1 at 550 K was conducted for 50 ps after static energy minimization, inducing significant diffusion of the Zr atoms to crystalline copper. S1 was finally quenched to 1 K in 50 ps for further simulations.

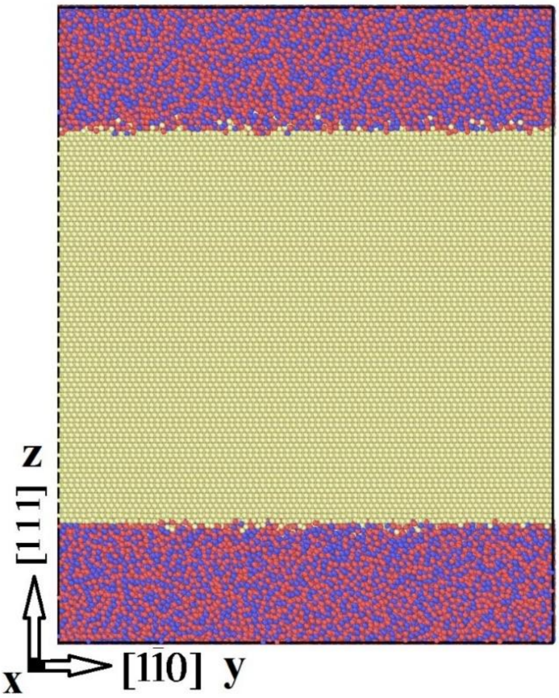

Figure 6.1. An illustration of sample geometry

The second, as-quenched sample (S2) had the same initial atomic configuration as S1 but was prepared using a different thermodynamic treatment. Consistent with the argument that Zr atoms should diffuse into the copper layer, the entire S2 was thermally relaxed at 800 K (above the glass transition temperature) for 1 ns, after being quenched from 1200 K to 800 K in 4 ns while the copper layer was still fixed. S2 was finally quenched from 800 K to 0 K in 8 ns for further deformation. The overall cooling rate of the amorphous layer in S2 was the same as that of the small BMGs in S1. S2 was assured to have a more realistic interface than S1 [19], as it had been verified experimentally that the amorphous layer is formed by the fast diffusion of Zr atoms into crystalline copper substrate [16].

Pure shear deformations were applied to S1 and S2 by directly changing the tilt factor of the supercells. The time steps during all deformations were set to be 1 fs and the tilt factor changed every 200 time steps to obtain a constant engineering shear strain rate, $\dot{\gamma}_{xz}(t)$. Shear deformations with different strain rates of $5\times10^9/s$ and $5\times10^8/s$ were applied to S1 and S2. The boundary conditions were set to be periodic for all deformations. A constant pressure and temperature ensemble was used to maintain the system temperature at 1 K and the other five stress tensor components were set to be traction free. Atomic shear strain analysis [23] and the common neighbor analysis (CNA) method [24] were used to display the deformation process. For convenience, in this work, atomic shear strain refers to von Mise atomic shear strain. Visualization of the simulations was performed by the software package OVITO [25].

6.3. Results and discussion

6.3.1 Interface characterization

Reference energy must be introduced to obtain the interfacial energy. A piece of BMG the same size as the amorphous layer and a crystal the same size of the crystalline layer were separately relaxed following the above procedures. The sum of the potential energies of the separately thermally relaxed BMG and the crystal was treated as the energy benchmark, $E_{benchmark}$. The interfacial energy of an ACI is defined as $(E_{potential}-E_{benchmark})/2\Delta S$, in which $E_{potential}$ and ΔS are the potential energy and cross-sectional area of nanolaminates S1 and S2 at a temperature of 1 K, respectively. Note that the interfacial energy definition is not based on the energy change in the affected zone of the interface alone, but on the energy change of the whole sample. The ACI changes the chemical composition distribution of the entire nano-sized amorphous layer, not just the zone near the interface, hence the energy distribution changes across the whole amorphous layer. The interfacial energy values for S1 and S2 were determined to be 72.60 mJ/m^2 and -133.1 mJ/m^2, respectively. The lower energy value for S2 than S1 implies that more zirconium diffused into the crystal in S2 than in S1, inducing more Cu-Zr bonding at the interface. Most importantly, the negative interfacial energy of S2 indicates that the distortion energy induced by the ACI was smaller than the energy reduction induced by the diffusion of zirconium into the crystal. This finding demonstrates that thermodynamic treatment can significantly alter the interfacial energy of the ACI in an amorphous/crystalline laminate.

It is known that GB energy consists not only of the excess energy of a highly disordered structure, but also the distortion of the neighboring crystalline structure. Akin to GB energy, ACI energy should also be stored with a spatial distribution. The crystalline materials are indexed as **C1**, **C2**, **C3**… **Ci,** in which "i" represents the ***ith*** {111} crystalline plane away from the interface. Similarly, the amorphous layers are indexed as **M1**, **M2**, **M3**…**Mi,** in which "i" represents the distance from the interface $\boldsymbol{i}\Delta z$, where Δz is a slice the width of three angstroms. The excess potential energy of each slice was calculated by subtracting an energy benchmark. We chose copper's cohesive energy, -3.54 eV, as the energy benchmark for the crystalline slices, even though they may have contained a few Zr atoms. For the amorphous slices, we chose the average atomic potential energy of a "perfect" $Cu_{46}Zr_{54}$, with the same number of atoms as the benchmark, even though the chemical composition of the slices was slightly different from $Cu_{46}Zr_{54}$. For simplicity, we chose only 10 slices on each side of the ACI.

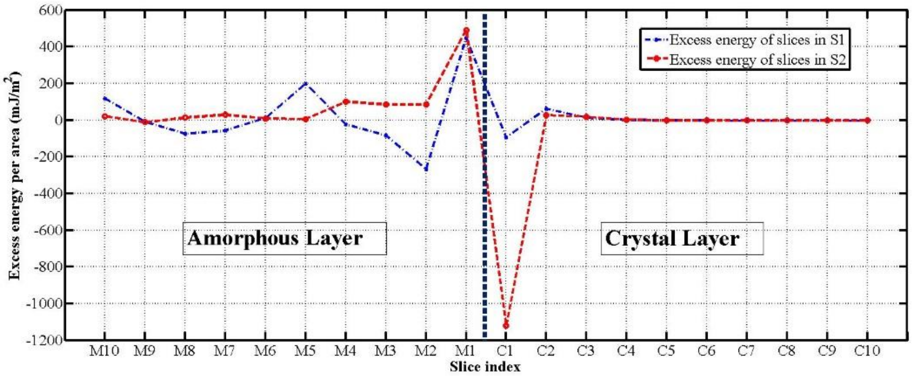

Figure 6.2. Excess energy of slices across the amorphous/crystal interface.

The excess energy distributions of S1 and S2 are shown in Fig. 6.2. Not surprisingly, in both S1 and S2, **C1** had negative excess energy due to the bonding of Cu-Zr both in and out of plane. **C1** in S2 had a much lower excess energy level (-1122 mJ/m^2) than that of **C1** in S1 (-95.26 mJ/m^2), because **C1** in S2 had many more Zr atoms (1038) than **C1** in S1 (102). Another reason that the ACI in the as-quenched S2 sample had lower energy than that in the separately quenched S1 sample and the benchmark system was that S2 had a 10-times higher zirconium concentration than S1. Lower energy is generally associated with a more stable structure. The as-quenched treatment of S2 significantly enhanced the segregation of Zr atoms in **C1** and induced stronger bonding between the amorphous layer and the crystalline layer through out-of-plane Cu-Zr bonding. Due to the low zirconium diffusivity in copper and the limited simulation time, **C2** in S1 had no zirconium atoms and **C2** in S2 had only one zirconium atom. Thus, the zirconium molar concentration gradients for the crystalline side were determined to be at the magnitudes of 10^8/m and 10^9/m for S1 and S2, respectively. Such a steep concentration gradient for the crystalline side of the ACI may still be valid for a real sample synthesized by the magnetic sputter decomposition method because the temperature is not high enough for zirconium to diffuse across the {111} plane. Another feature of the energy distribution on the crystalline side was that **C2** had the highest excess energy in both S1 and S2, - 61.58 and 27.25 mJ/m^2, respectively. The reason for the high excess energy was that **C2** had a much lower level of Zr-Cu bonding (only out-of-plane bonding with zirconium in **C1** and **M1**), and its excess energy mainly arose from the distortion caused by the interaction with the amorphous layer. It should be emphasized that **C2**'s excess energy was much lower than the GB energy of copper, and was comparable to copper's stacking fault energy (SFE). **C2** also had a perfect in-plane face-centered cubic (FCC) structure which, together with the low distortion energy, implies that it was not a structural planar fault similar to either a stacking fault (SF) or a twin boundary (TB). It was also clear that the excess free energy of the crystalline slices quickly decreased as the distance from the interface increased. Most of the distortion energy of the crystalline material was stored in **C2** and **C3**. We used a potential function cutoff of 0.65 nm, thus for **C2** and **C3,** the bonding regions of both the highly disordered amorphous layer and the zirconium atoms were within those of **C1**. The positive energy contribution from the distorted Cu-Cu bonding prevailed over the negative energy contribution from the out-of-plane Cu-Zr bonding in both **C2** and **C3**. **C3** had nearly the same excess energy in both samples, and from **C4** on, each slice's energy stayed very close to that of a perfect {111} copper plane. It can be concluded that the thickness of the ACI-affected zone on the crystalline side was limited to about 0.6 nm in **C1**, **C2** and **C3**.

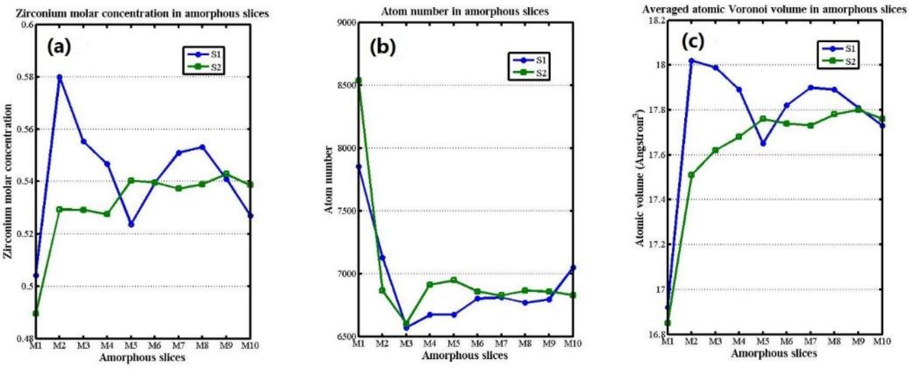

Figure 6.3. (a) zirconium molar concentration, (b) atom number and (c) averaged atomic Voronoi volume distribution on amorphous side of ACI.

On the BMG side of the ACI, the **M1** slices in S1 and S2 had similar positive excess energy levels of 447.7 and 491.5 mJ/m^2, respectively. A loss of zirconium atoms in **M1** was responsible for this positive excess energy. Generally, if the zirconium concentration (C_{zr}) is lower than that in the benchmark BMG (54%), the excess energy of the amorphous layer is positive; otherwise, it is negative. Fig. 6.3(a) shows that the zirconium molar concentration varied with the distance from the ACI. A significantly lower zirconium concentration was observed for the **M1** slices in both S1 and S2. However, from **M2** on, the zirconium molar concentration distributions in S1 and S2 showed a distinct trend. The zirconium concentration gradually increased to around 54% in S2 but fluctuated in S1, showing strong correlations with the excess energy distributions. The fluctuation in the excess energy and chemical composition of S1 provides strong evidence that S1 had a more heterogeneous structure than S2.

Fig. 6.3(b) shows the atom number distribution near the ACI inside the amorphous layer for both S1 and S2. There were significantly more atoms in **M1** than in the other slices on the amorphous side in both S1 and S2. However,

M1 in S1 had fewer atoms in total than **M1** in S2 (7851 and 8534, respectively), due to less sufficient thermodynamic diffusion. The **M1** slices in both S1 and S2 also had a higher copper atom concentration than the other slices on the amorphous side. The segregation of copper at the ACI is induced by diffusion due to the steep chemical potential gradient of copper across the amorphous layer and the crystalline layer. Zirconium's diffusion from **M1** to **C1** and copper's diffusion from **M2** to **M1** both contributed to the change in the chemical composition of **M1**. This change in composition caused the lower zirconium concentration and higher copper concentration in **M1** than in the other slices on the amorphous side of the ACI in both S1 and S2, making the structural properties of **M1** significantly different from the other parts of the amorphous layer. Fig. 6.3(c) shows that the average atomic Voronoi volume (the volume of the Voronoi cell around an atom) varied with the distance from the ACI on the amorphous side. **M1** had the smallest average atomic Voronoi volume in both S1 and S2, associated with the highest copper concentration and lowest zirconium concentration. There was a strong correlation between the zirconium concentration and average Voronoi volume in the amorphous slices, with correlation coefficients of 0.8556 and 0.9851 for S1 and S2, respectively. The average Voronoi volume can be considered as an indicator of the atomic free volume. The larger the Voronoi volume, the more empty space the material has. Generally, a small region with a larger free volume is more vulnerable to inelastic atomic rearrangement [26, 27]. The non-uniform atomic volume distribution on the amorphous side also suggests heterogeneities induced by the ACI, as implied by the excess energy concentration and zirconium molar concentration distribution.

To quantify the expected structural heterogeneity of the amorphous layer induced by the ACI, we define a parameter $\delta_a = \sqrt{\sum_{i=1}^{N}(a_i - \bar{a})^2 / N\bar{a}^2}$ in which *a* represents the atomic attributes and *N* is the total number of atoms. The larger the value of δ_a, the more heterogeneous the system. If we set *a* to be the atomic potential energy and δ_a to be the relative heterogeneous parameters for freestanding BMG, the amorphous layers in S1 and S2 are 0.2630, 0.2672 and 0.2648, respectively. A non-zero value of δ_a for freestanding BMG is induced by the intrinsically disordered structure of BMG. S1 was expected to have the largest δ_a because it did not undergo sufficient thermal relaxation during preparation. The higher value of δ_a for S2 than for freestanding BMG demonstrates that the ACI introduces structural heterogeneities into the amorphous layer in amorphous/crystalline nanolaminate. Such heterogeneity can also be characterized by several structural features, such as the atom number distribution and average Voronoi volume, as shown in Fig. 6.3, and the energy, as shown in Fig. 6.2. Note that the heterogeneity contains contributions from the fluctuations across the entire amorphous layer.

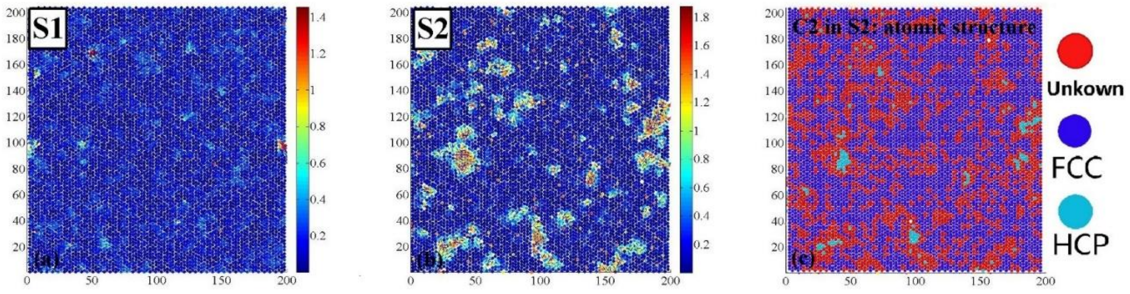

Figure 6.4. (a) Disregistry vector map for slice C_1 in S1. (b) Disregistry vector map for slice C_1 in S2. In (a) and (b), atoms are represented by dots colored by disregistry magnitude and

arrows show the vectors of disregistry. (c) Atomic structure map obtained by CNA method [25] for slice C_2 in S2: solid cyan circles represent atoms with HCP structure.

Another distinct feature of the ACIs in S1 and S2 is the intrinsic disregistry in **C1**, which shows a dislocated core structure. The disregistry vector is measured according to a relative in-plane displacement vector. For each sample, **C7**—a perfect crystalline plane—is chosen as the reference. Figs. 4(a) and (b) depict the intrinsic disregistry in **C1** for S1 and S2, respectively. Each dot represents an atom with the color corresponding to the magnitude and the arrow corresponding to the vector of the disregistry. The arrows in Fig. 6.4(a) are almost invisible due to their very small magnitudes by compared with the cross-section area. Several islands can be observed in **C1** of S2 in Fig. 6.4(b), with a disregistry magnitude of approximately 0.15 nm and diameter of about 2~3 nm, whereas no such island is observed in **C1** of S1. Detailed analysis shows that several regions of **C2** in S2 that correspond to these islands in **C1** have a hexagonal close packing (HCP) structure, as shown in Fig. 6.4(c), and the rest have an unknown structure. Thus, it is clear that there are partial dislocation loops in S2's interfaces, in agreement with the literature [19]. Because the ACI energy of S2 is much lower than that of S1, such an ACI configuration with small dislocation loops has minimal local energy. The absence of such dislocation loops in the ACI in S1 may be because the relaxation time was not sufficient to allow it to reach a local minimum energy state.

6.3.2 Shear deformation

Fig. 6.5 shows the shear stress versus the engineering shear strain curves of the shear deformation in S1 and S2 at different strain rates and at the same temperature (1 K). Such a low temperature was chosen because it largely eliminated the effect of thermodynamic fluctuation and allowed us to focus on displacive processes. Fig. 6.5(a) shows the stress-strain curves for S1 and S2 with $\dot{\gamma}_{xz}(t) = 5\times10^{9}/s$. Both samples show linear mechanical responses when γ_{xz}<1%. The shear modulus was fitted from the data obtained in an elastic regime. The shear modulus for S2 is 28.6 GPa higher than that for S1 (26.0 GPa). The discrepancy in the shear modulus between S1 and S2 originates from their amorphous layer structures. S2 is more stable than S1 due to its lower interface energy. After yielding, a nonlinear mechanical response starts to manifest in each sample. S1 and S2 show distinct inelastic behavior. A significant transition related to a discontinuous slope is observed when γ_{xz} = 4.15% and τ_{xz} =0.914 GPa on the stress-strain curve for S1. A similar transition is observed at $\gamma_{xz} = 6.35\%$ and τ_{xz} =1.43 GPa on the stress-strain curve for S2. Above $\gamma_{xz} = 4.15\%$, the stress in S1 continues to increase but with a decreasing slope, until the engineering shear strain reaches about 35.7%. Unlike the stress-strain curve for S1, the shear stress for S2 only increases up to $\gamma_{xz} \approx 11.0\%$, then gradually decreases and stays at a plateau until $\gamma_{xz} \approx 26.0\%$. The ultimate shear stress, which is defined as the stress corresponding to the highest point on the strain-stress curve, is reached at $\gamma_{xz} \approx 35.7\%$ and $\gamma_{xz} \approx 11.0\%$ for S1 and S2, respectively. The stress-strain curves show that S1 softens much later than S2. The stress-strain curves for S1 and S2 in Fig. 6.5(a) both show tails with inverted comb shapes.

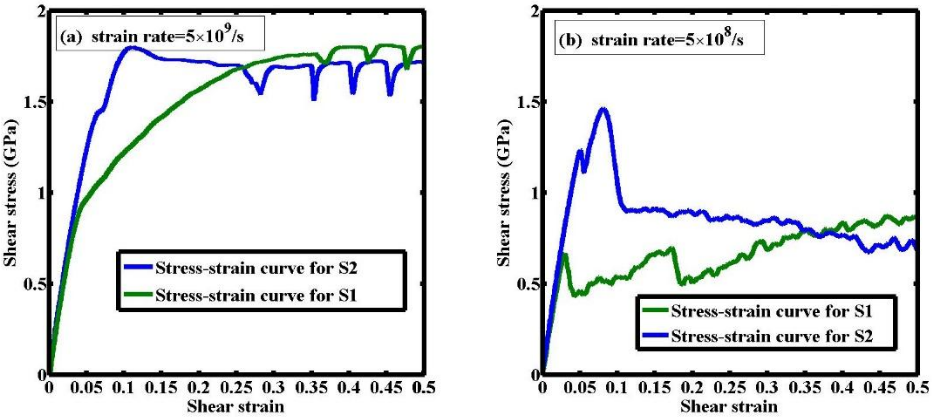

Figure 6.5. Shear stress versus engineering shear strain curves for S1 and S2 under different strain rates $5\times10^{9}/s$ (a) and $5\times10^{8}/s$ (b).

Multiple yielding behavior was expected for both S1 and S2 due to their complex shear responses, as discussed above. To find the atomic mechanisms associated with the stress-strain curve features, we performed the atomic strain analysis using OVITO [25], and analyzed the atomic structure output using the CNA method [24]. Fig. 6.6 shows the atomic shear strain maps at different macroscopic engineering shear strains. When γ_{xz}=3.0%, there are several small zones with shear strains that are clearly higher than their neighboring regions inside the amorphous layers in both S1 and S2. For convenience, these zones are considered to be shear transformation zones (STZs), as found in MD simulations of BMG [16, 28, 29], although there are other explanations for the shear concentration in BMG [27, 30]. In comparison, when γ_{xz}=3.0%, no STZs are found in the reference BMG under the same simulation conditions. The formation of STZs provides solid evidence that amorphous layers in amorphous/crystal nanolaminate yield quite early, before significant deviation from the elastic response occurs on the stress-strain curve. Unlike other simulations, the STZs in amorphous layers are incipient plastic events in nanolaminates during pure shear, rather than dislocation emissions at the ACI [16, 18]. Several STZs are found near the ACI, but other STZs are scattered inside the amorphous layer, indicating the absence of shear localization at the ACI. The early appearance of STZs during deformation demonstrates that the strength of the amorphous layers is lower in both S1 and S2 than in the reference BMG. Conversely, the nucleation of multiple STZs indicates that nano-sized amorphous layers may be capable of carrying much more plastic deformation than their bulk counterparts. In Section 6.3.1, it was confirmed that the ACI induced significant heterogeneity in the amorphous layers in both S1 and S2, with weakened regions in these layers. The weakened regions were vulnerable to local inelastic atom rearrangement and thus were easily plastically deformed, providing multiple nucleation sites for STZs. It is reasonable that both of the amorphous layers in S1 and S2 yielded earlier than in the other parts of the bulk.

Another interesting phenomenon is that no shear band formed during the simulation. The absence of a shear band is consistent with the size effect predicted by the ARGL model [29], allowing the rest of the nanolaminates to build up stress during deformation without forming a shear band. It should also be emphasized that the formation of the STZ in the early stage only drove the mechanical responses of S1 and S2 slightly away from a linear relationship before the significant transition points on the stress-strain curve, as shown in Fig. 6.5(a).

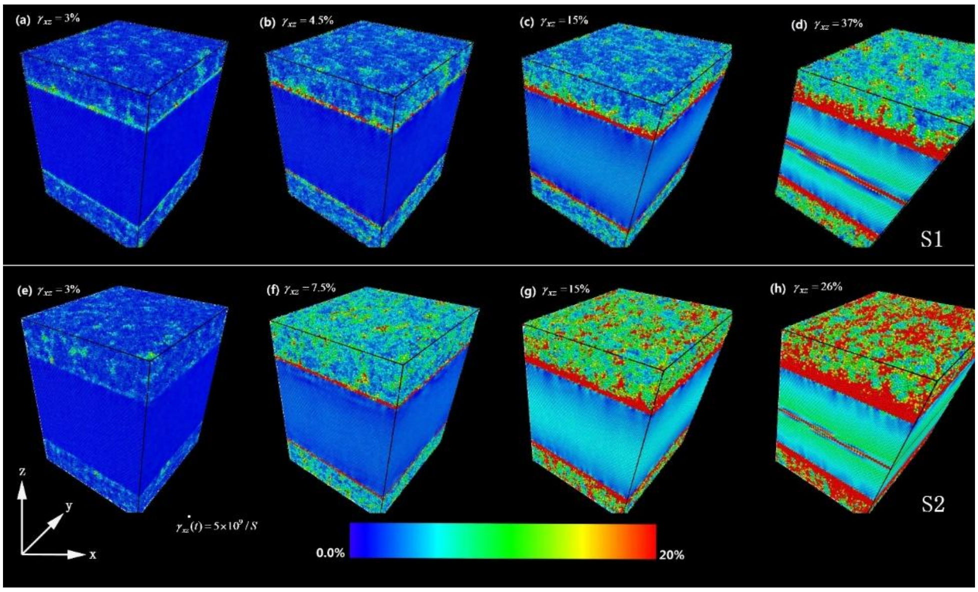

Figure 6.6. Perspective atomic shear strain map under $5\times10^9/s$ for S1 [(a), (b), (c), (d)] and S2 [(e), (f), (g), (h)] with different strain.

At the stress-strain transition point of γ_{xz}=4.15% for S1, slice **C1** and part of **M1** show highly localized shear strain, along with the release of localized shear stress at the ACI. The rapid formation of this shear strain localization at the ACI as the strain approaches γ_{xz}=4.15% can be seen in the dynamic evolution of the shear map. A similar localized shear strain is also formed in slices **C1** and **C2** in S2 when γ_{xz}=6.35%. The slope discontinuity of displacement versus z- coordinate at ACIs suggested that shear localization at the ACI was induced by interfacial sliding, which occurred via different deformation mechanisms for S1 and S2. The first yielding via interfacial sliding is consistent with a previous study on an amorphous CuZr/crystalline Zr layered micropillar [20]. Figs. 7 and 8 show the interfacial sliding processes of S1 and S2, respectively. In Fig. 6.7, times 7, 8, 9 and 10 ps correspond to engineering shear strains of 3.5%, 4%, 4.5% and 5%, respectively. A strong correlation between the atomic shear strains in **C1** and **M1,** from atom to atom, is observed in S1. There is also a strong one-to-one correspondence between the shear localization sites in C1 and **M1**. Meanwhile, the level of atomic shear strain in **C2** remained low during this process, indicating that **C2** did not participate in the interfacial sliding. That is, the interfacial sliding in S1 was due to the relative sliding between **C1** and **M1**. Red regions with high shear strain appeared in the “pre-deformed” areas in **C1** and **M1**. It is assumed that when t=7ps, these pre-deformed areas were achieved by shear localization on the amorphous layer side, which resulted in the formation of STZs. Identically, the interfacial sliding in S1 was mediated by the growth of STZs in **C1** and **M1**. In Fig. 6.8, times 8, 9, 12 and 14 ps correspond to engineering shear strains of 4%, 4.5%, 6% and 7%, respectively. Unlike in S1, there is a strong correlation between **C1** and **C2**. Meanwhile, much less shear strain localization is observed in the pre-deformed areas in **M1,** with strain increasing more than in the other two slices. Fig. 6.8(d) clearly shows the expansion of a stacking fault (represented by the HCP atomic plane) in **C2**, providing evidence of an interfacial dislocation loop spreading in **C2**. Thus, the interfacial sliding in S2 was mediated by the spreading of interfacial partial dislocation loops within **C1** and **C2,** rather than the growth of STZs in **M1** and **C1**. This mechanism has already been confirmed in simulations of non-coherent or semi-coherent interfaces, in which island-shaped dislocation structures always occur [8].

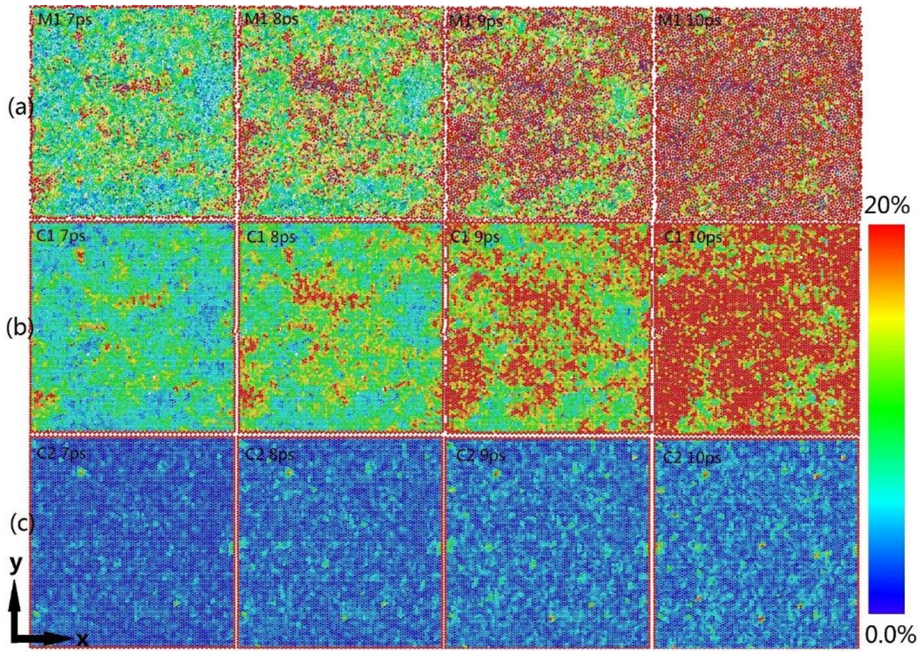

Figure 6.7. Atomic shear strain map of **C1** (a), **C1** (b), and **M1** (c) in S1 at different times during shearing.

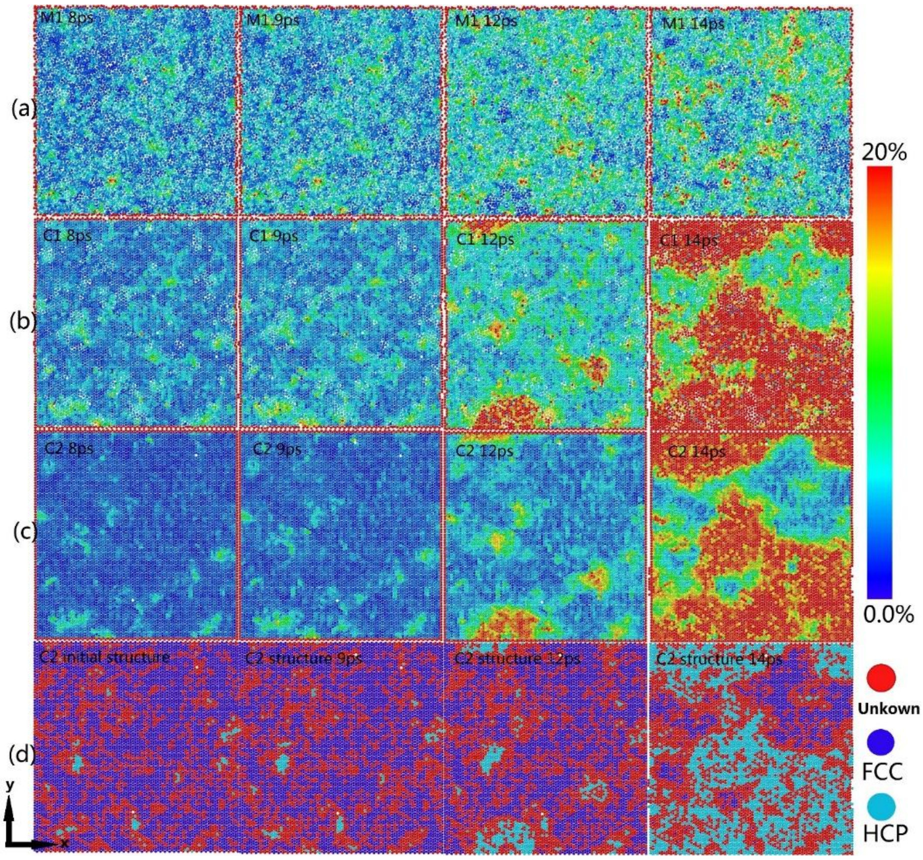

Figure 6.8. Atomic shear strain map of **C1** (a), **C2** (b), **M1**(c) and atomic structure map of **C2** (d) in S2 at different times during shearing.

The revelation of the sliding process in S1 and S2 demonstrates that interfacial sliding began heterogeneously at some weaker sites induced by the formation of STZs (S1) and at partial dislocations (S2), rather than homogeneously along the whole ACI. These interfacial sliding mechanisms at the ACI differ from the GB sliding mechanism observed in MD simulations of nanocrystalline metals [1, 31]. GB sliding within nanocrystalline metals is associated with atomic shuffling and stress-assisted free volume migration [31], and requires GB diffusion to accommodate the deformation [1, 32]. In comparison, ACI sliding is likely to be associated with the evolution of elementary plasticity carriers, STZs in S1 and dislocation in S2, rather than single-atom shuffling or free-volume migration.

Furthermore, the stress required to initiate interfacial sliding of the ACI was only 0.914 GPa for S1, but 1.433 GPa for S2. Thus, the ACI of S2 had much higher resistance to shear deformation than that of S1. To physically elucidate the ACI's resistance to sliding, we applied the concept of general stacking fault energy (GSFE), as in the literature, but with all atoms constrained [29, 33]. First we cut the bulk into two halves at a particular position along the z direction. Then we slid the lower half against the upper half in x direction, with a displacement δ. The increased energy per area is treated as GSFE. The GSFE curves are shown in Fig. 6.9. The slope of the GSFE curve quantitatively describes the inter-planar resistance to shear deformation. It is clear from the figure that the slope of the increase in GSFE between **C1** and **C2** in S1 is almost the same as that of the GSFE between **C1** and **C2** in S2. In S1, the GSFE curve between **C1** and **M1** is much shallower than that of the GSFE between **C1** and **C2,** indicating much weaker bonding between the amorphous layer and the crystalline layer. However, in S2, the slope of the GSFE curve between **C1** and **M1** is much steeper than that between **C1** and **C2**, indicating strong bonding between the amorphous and crystalline layers. Thus, the interfacial sliding mediated by the spreading of the interfacial dislocation loop in S2, rather than the growth of STZs in S1, can be explained from an energy perspective. The distinct slopes of the GSFE curves obtained between **C1** and **M1** agree very well with the distinct energy summations of **C1** and **M1** in S1 and S2, respectively. Fig. 6.9 also shows that the bonding between **C1** and **C2** in S2 was almost as strong as the bonding between two adjacent {111} crystal planes, and was much weaker than the bonding between **C1** and **M1**, suggesting that the shear resistance of a well stabilized amorphous/crystalline nanolaminate may reach the ideal shear strength of its crystalline constituent. The calculations for the GSFE in the

ACI, together with the previous analysis, confirm that appropriate thermodynamic treatment can change the structure and relative shear strength of the ACI..

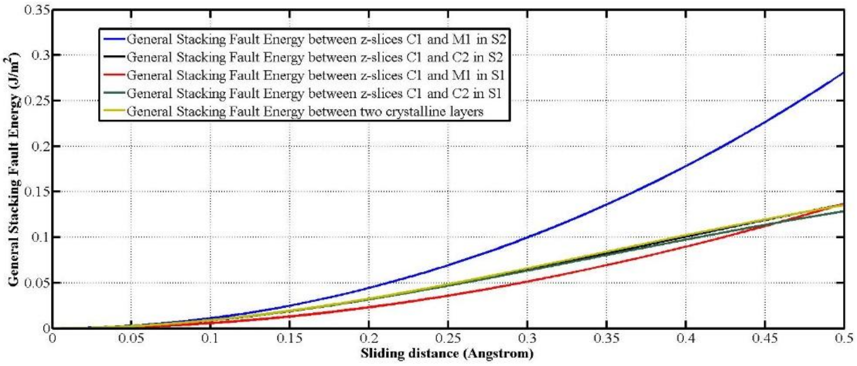

Figure 6.9. General stacking fault energy (GSFE) obtained by sliding sample along x axis at different z-coordinates.

Figs. 6.6(c) and 6.6(g) show that when γ_{xz}=4.15%, the STZs in S2 were already well developed, but those in S1 remained nearly the same size as those when γ_{xz}=4.15%. This phenomenon indicates that the interfacial sliding in S1 carried much more plastic deformation than that in S2. In other words, the deformation in S1 was more highly localized than in S2. To confirm this assumption, Fig. 6.10 plots the average von Mises atomic shear strain [23] along the z-direction in both S1 and S2 when γ_{xz}=8.5%. When the strain γ_{xz}=8.5%, the stress was still increasing in both S1 and S2. At this point, it is clear that the atomic shear strain in S1 was much more heavily localized in ACI than in S2, carried by interfacial sliding. Because the strain rate was rather high, other parts of S1 under low strain continued to build up stress and hence the total shear stress continued to increase, as shown in Fig. 6.5(a). Note that the distance between the two atomic strain peaks for S2 is shorter than that for S1, consistent with the fact that interfacial sliding occurred at different relative positions for S1 and S2. Fig. 6.10 also shows that the considerable shear strain in S2 was carried by the amorphous layer and that the shear strain was much less localized at the interface in S2 than in S1.

To further elucidate the shear deformation localization, we chose a in $\delta_a = \sqrt{\sum_{i=1}^{N}(a_i - \bar{a})^2 / N\bar{a}^2}$ to be the atomic shear strain, and thus δ_a became a parameter representing the heterogeneity of deformation. The parameter δ_a was calculated over the whole bulk with 8.5% strain. This heterogeneity parameter was 0.96 for S2 but 2.5 for S1, demonstrating that S2 deformed more homogeneously than S1. In conclusion, the shear strain was highly localized at its weak ACI, indicating that S1 was much more brittle than S2.

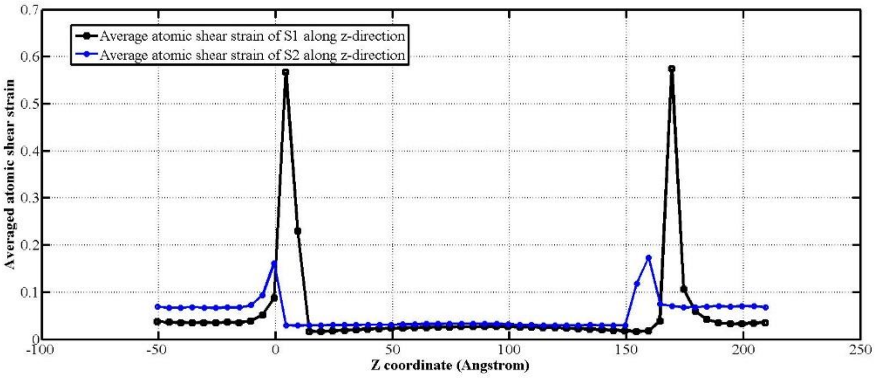

Figure 6.10. Average atomic shear strain of S1 and S2 along z-direction when shear strain=8.5%.

However, the reduction in stress in S2 in Fig. 6.5(a) after γ_{xz}≈11.0% cannot be explained by the growth of the STZ, which occurred much earlier. This could represent a new plastic deformation mechanism that may occur at the ACI. Fig. 6.6 also shows that a micro-band with highly localized shear strain formed along the ACIs in both S1 and S2. We define this band with highly localized shear strain as a micro-sliding band. For S2, the micro-sliding band started to thicken when γ_{xz}≈11.0%, corresponding to the stress peak followed by a gradual drop, as shown in Fig. 6.5(a). Thus, the thickening process of this micro-band may be considered a new plastic deformation process. At the very beginning, micro-sliding bands were formed at, and limited within, the ACIs. New interfaces were then formed between the micro-sliding bands, which had a finite thickness and amorphous layers with much lower shear strain. Because the amorphous layer in S2 carried considerable plastic deformation via STZ growth, some fragments of the newly formed interface were positioned between several STZs and the micro-sliding bands. We use f_1 to represent the viscosity of the crystalline layer, f_2 for the viscosity of the amorphous regions without STZs and f_3 for the viscosity of the STZs. It is well known that the structure of the STZ is disrupted, and that its viscosity dramatically decreases by large magnitudes from the viscosity of well-aged glass. Thus, it is reasonable that $f_1 >> f_2 >> f_3$. Because STZs have rather low viscosity, a considerable friction force is exerted on the STZs adjacent to the micro-sliding band, forcing the atoms in the STZs to flow. The internal friction-induced plastic flow in STZs actually transforms their structure from glue-like to liquid-like, with highly localized atomic shear strain and extremely low viscosity [29, 34] as they become part of a thickened micro-sliding band. This process occurs repeatedly during deformation. The thickening process is such that the micro-sliding band swallows the STZs inside the amorphous layer. Meanwhile, because the shear strain was highly localized in the micro-sliding bands, the STZs in S1 were not well developed, as shown in Fig. 6.5. Thus, the effective viscosity of the amorphous layer, which can be defined as the average viscosity of the deformed amorphous layer containing STZs, decreased much more slowly in S1 than in S2 as it contained fewer STZs. This helps to explain why the micro-sliding band thickened much more slowly in S1 than in S2.

The thickened micro-sliding band can be divided into two parts: the initial micro band induced by interfacial sliding and the swallowed amorphous regions. The latter regions had a severely deformed structure with a viscosity lower than that of the amorphous layer. However, the micro-sliding band would be expected to provide resistance to shear deformation through a displacive alienating process [29]. Thus, a steady plastic flow was expected inside it, which can be described by $\tau = \eta \dot{\gamma}_{xz}$, in which η is viscosity. This steady plastic flow explains the plateaus on the stress-strain curves of S2 in Fig. 6.5. The viscosity of the micro-sliding band in S2 can then be estimated by dividing the plateau stress by the strain rate. The viscosity η is approximately computed to be 0.34 Pascal●Second when $\dot{\gamma}_{xz} = 5 \times 10^{9} / s$ and approximately 1.8 Pascal●Second when $\dot{\gamma}_{xz} = 5 \times 10^{8} / s$. Two conclusions can be drawn from the estimation of the micro-sliding band's viscosity. The first is that the values of the two different strain rates were both very low compared with that of super-cooled liquid and crystal [34]. The second is that the viscosity obtained from the low strain rate simulation was higher than that obtained from the high strain rate simulation. The reason for the discrepancy is that the severely deformed structure of the micro-sliding band searches for a local minimum energy position via atomic displacive movements that comprise the recovery process in the glue zone in an embryonic shear band [29]. As the strain rate decreases, a more "solid" amorphous structure with higher viscosity can be achieved during deformation. With the temperature effect accounted for, two results can be expected. The first is that the structure of the micro-sliding band can more rapidly attain local minimums and thus appear more “solid” during deformation. The second is that even at the low strain rate of most experiments, the viscosity of the liquid-like structure will not be as high as that of its neighboring regions inside the amorphous layer due to the sharp increase in temperature resulting from energy localization. The first result is demonstrated by the similar stress-strain curve of S2 under the isoenthalpic-isobaric (NpH) ensemble, which allows the temperature to increase and $\dot{\gamma}_{xz} = 5\times10^{9}/s$ to equal that under T=1 K and $\dot{\gamma}_{xz} = 5\times10^{8}/s$. However, MD is still incapable of dealing with the second prediction.

Figs. 6.6(d) and 6.6(h) show that the crystalline layers of both S1 and S2 yield when there is sufficient shear strain. Atomic structure analysis shows that deformation twinning occurred in the center of the crystalline layers in both S1 and S2, via successive partial slips along the x-direction. Each stress drop at the tail of the stress-strain curves in Fig. 6.5(a) corresponds to a partial slip on a twin boundary. Neither deformation twinning nor Shockley partial slips were observed inside the crystalline layers in either sample when $\dot{\gamma}_{xz} = 5\times10^{8}/s$.

6.3.3 Interfacial sliding versus dislocation emission

Unlike previous simulations, we did not observe any partial dislocation emission from the ACIs under shear deformation. We assume that the interfacial sliding at the ACI competed with dislocation emission from the ACI. Next, we demonstrate that interfacial sliding can manifest in plastic deformation before dislocation emission from the ACI. As shown in Fig. 6.11, a tensile stress σ was applied on an amorphous/crystalline nanolaminate, with an angle of $90^{\circ}-\theta$ in respect to the normal vector of the ACI. The tetrahedron ABCD in Fig. 6.11 illustrates a slip system. The blue plane, BCD, represents the plane on which the ACI lies. There are partial dislocations in the ACI of well-quenched nanolaminates such as S2, and interfacial sliding occurs when they slip. It is clear that the easiest partial slip to activate in BCD is αB, as it has the largest Schimid factor. The shear stress acting on αB when interfacial sliding occurs is

$$\tau_{sliding} = \sigma \cos\theta \sin\theta = \sigma \sin(2\theta)/2 \qquad \text{Eq. 6.1}$$

in which $\tau_{sliding}$ is the interfacial sliding strength. The shear stress acting on the most easily activated slip system when dislocation emission occurs is described as

$$\begin{aligned}\tau_{slip} &= \sigma \cos(70.5^\circ - \theta)\sin(70.5^\circ - \theta) = \sigma \sin(141^\circ - 2\theta)/2,\ \theta < 70.5^\circ \\ \tau_{slip} &= \sigma \cos(\theta - 70.5^\circ)\sin(\theta - 70.5^\circ) = \sigma \sin(2\theta - 141^\circ)/2,\ \theta > 70.5^\circ\end{aligned}$$

Eq. 6.2

in which τ_{slip} is the critical shear stress to activate partial slip in the amorphous layer. Thus, if the inequalities

$$\begin{aligned}&2\tau_{sliding}/\sin(2\theta) < 2\tau_{slip}/\sin(141^\circ - 2\theta), \theta < 70.5^\circ \\ &2\tau_{sliding}/\sin(2\theta) < 2\tau_{slip}/\sin(2\theta - 141^\circ), \theta > 70.5^\circ\end{aligned} \qquad \text{Eq. 6.3}$$

are satisfied, interfacial sliding will occur before dislocation emission. The analytical solution for the inequalities in Eq. 6.3 is

$$\begin{aligned}&90^\circ - 0.5\arctan[0.6285\tau_{sliding}/(\tau_{sliding} + 0.7778\tau_{slip})] > \theta > 70.5^\circ \\ &0.5\arctan[0.6285\tau_{sliding}/(\tau_{sliding} - 0.7778\tau_{slip})] < \theta < 70.5^\circ\end{aligned} \qquad \text{Eq. 6.4}$$

The solution, $70.5^\circ > \theta > 0.5\arctan(0.6285\tau_{slip}/(\tau_{sliding} - 0.7778\tau_{slip}))$, can always be reached. When $\tau_{sliding} > 0.7778\tau_{slip}$, the solution is $\theta < 0.5\arctan(0.6285\tau_{slip}/(\tau_{sliding} - 0.7778\tau_{slip}))$. Note that the critical shear stress on the slip plane, τ_{slip}, increases as the thickness of the crystalline layer decreases. When the thickness of the crystalline layer reaches nano size in an Cu/Nb multilayer composite [9], τ_{slip} can reach about half of the ideal shear strength of copper due to the size effect [9, 35].

In a sample prepared with insufficient quenching such as S1, $\tau_{sliding}$ is quite low and $\tau_{sliding} < 0.7778\tau_{slip}$ is satisfied. Thus, if the tensile direction is not perpendicular to the interface plane, interfacial sliding always occurs before dislocation emission. In a well-quenched sample such as S2, $\tau_{sliding}$ can be as high as τ_{slip} and thus $\tau_{sliding} > 0.7778\tau_{slip}$ is satisfied. Thus, there is a range of θ within which interfacial sliding can occur before dislocation emission. However, S2 has a very reasonable ACI structure, which can be expected in a BMG-based composite. Several families of BMG composites with crystalline inclusions have been synthesized [36-39]. As an equilibrium ACI exists in such materials, the interfacial sliding and thickening of the micro-sliding band is to be expected.

The tensile ductility of BMG-based composites has been attributed to the crystalline components' ductility and ability to hamper shear-band propagation [39]. In this chapter, a new deformation scenario is proposed, based on the finding that the ACIs inside such materials can slide before dislocation emission. At the very beginning, the weakened regions around the crystalline material induced by the presence of ACIs yield first, and nano-sized STZs are formed. Interfacial sliding then occurs and a micro-sliding band forms at the ACI. If the fraction of ACI atoms in such materials is as high as the fraction of grain boundary atoms in nanocrystalline materials, interfacial sliding is capable of carrying considerable plastic deformation, thus making such BMG composites ductile. It should be noted that such ACI sliding may not induce catastrophic failure of the material [20]. The presence of STZs in the neighborhood causes the micro-sliding band confining the crystalline material to start to thicken due to swallowing of the weakened BMG zones. The structure of this band features highly localized shear strain and low viscosity. Once the thickness of the micro-sliding band grows to several nanometers, it is reasonable to assume that it will continue to thicken as it absorbs the STZs. This scenario may help to further understand the ductility of BMG with nano crystals.

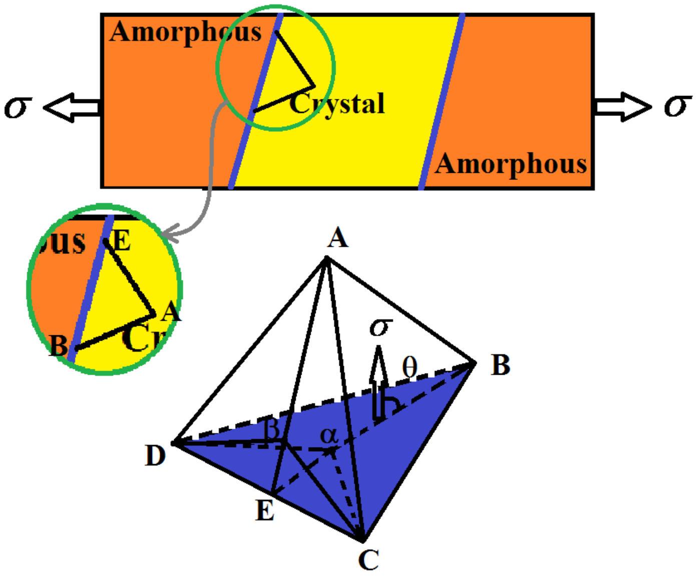

Figure 6.11. A model for mechanical analysis - the bottom tetrahedron represents slip system in FCC structure.

6.4. Conclusion

Two types of amorphous/crystalline interfaces were prepared via different thermodynamic treatments by MD simulation. A common structural inhomogeneity was observed in the amorphous $Cu_{46}Zr_{54}$ layers of both as-quenched and separately quenched samples. During shear deformation, the amorphous layers in both samples yielded first through the formation of STZs. Micro-sliding bands with highly localized atomic shear strain then formed at the ACIs in both samples via different interfacial mechanisms: sliding via the growth of STZs at the ACIs for the separately quenched sample, and sliding due to spreading of the dislocation loop at the ACI for the as-quenched sample. The thickening of the micro-sliding bands on the amorphous side via internal friction was determined to be a new plastic deformation mechanism in amorphous/crystalline nanolaminate that occurs under appropriate loading conditions. The micro-sliding band thickened more rapidly in the as-quenched sample than in the separately quenched sample. The crystalline layer finally yielded due to partial dislocation slip. In conclusion, MD simulations identified a new multi-yielding scenario involving interfacial sliding and thickening of the micro-sliding band, which is expected to operate in BMG-based nano-composites.

Reference

[1] M.A. Meyers, A. Mishra, D.J. Benson, Mechanical properties of nanocrystalline materials, Prog. Mater Sci., 51 (2006) 427-556.

[2] K. Lu, L. Lu, S. Suresh, Strengthening Materials by Engineering Coherent Internal Boundaries at the Nanoscale, Science, 324 (2009) 349-352.

[3] J. Löffler, J. Weissmüller, Grain-boundary atomic structure in nanocrystalline palladium from x-ray atomic distribution functions, Physical Review B, 52 (1995) 7076-7093.

[4] M.H. Frey, D.A. Payne, Grain-size effect on structure and phase transformations for barium titanate, Physical Review B, 54 (1996) 3158-3168.

[5] J. Wang, A. Misra, An overview of interface-dominated deformation mechanisms in metallic multilayers, Curr. Opin. Solid State Mater. Sci., 15 (2011) 20-28.

[6] L. Del Bianco, A. Hernando, E. Bonetti, E. Navarro, Grain-boundary structure and magnetic behavior in nanocrystalline ball-milled iron, Physical Review B, 56 (1997) 8894-

8901.

[7] O.A. Shenderova, D.W. Brenner, A. Omeltchenko, X. Su, L.H. Yang, Atomistic modeling of the fracture of polycrystalline diamond, Physical Review B, 61 (2000) 3877-3888.

[8] H. Van Swygenhoven, D. Farkas, A. Caro, Grain-boundary structures in polycrystalline metals at the nanoscale, Physical Review B, 62 (2000) 831-838.

[9] A. Misra, J.P. Hirth, R.G. Hoagland, Length-scale-dependent deformation mechanisms in incoherent metallic multilayered composites, Acta Mater., 53 (2005) 4817-4824.

[10] V. Yamakov, D. Wolf, S.R. Phillpot, A.K. Mukherjee, H. Gleiter, Dislocation processes in the deformation of nanocrystalline aluminium by molecular-dynamics simulation, Nature Materials, 1 (2002) 45-48.

[11] V. Yamakov, D. Wolf, S.R. Phillpot, A.K. Mukherjee, H. Gleiter, Deformation-mechanism map for nanocrystalline metals by molecular-dynamics simulation, Nature Materials, 3 (2004) 43-47.

[12] A. Caro, H. Van Swygenhoven, Grain boundary and triple junction enthalpies in nanocrystalline metals, Physical Review B, 63 (2001) 134101.

[13] L. Lu, Y.F. Shen, X.H. Chen, L.H. Qian, K. Lu, Ultrahigh strength and high electrical conductivity in copper, Science, 304 (2004) 422-426.

[14] L. Lu, X. Chen, X. Huang, K. Lu, Revealing the Maximum Strength in Nanotwinned Copper, Science, 323 (2009) 607-610.

[15] X.Y. Li, Y.J. Wei, L. Lu, K. Lu, H.J. Gao, Dislocation nucleation governed softening and maximum strength in nano-twinned metals, Nature, 464 (2010) 877-880.

[16] Y. Wang, J. Li, A.V. Hamza, T.W. Barbee, Ductile crystalline–amorphous nanolaminates, Proceedings of the National Academy of Sciences, 104 (2007) 11155-11160.

[17] J.-Y. Kim, D. Jang, J.R. Greer, Nanolaminates Utilizing Size-Dependent Homogeneous Plasticity of Metallic Glasses, Adv. Funct. Mater., 21 (2011) 4550-4554.

[18] B. Arman, C. Brandl, S.N. Luo, T.C. Germann, A. Misra, T. Çağin, Plasticity in Cu(111)/Cu46Zr54 glass nanolaminates under uniaxial compression, J. Appl. Phys., 110 (2011) -.

[19] C. Brandl, T.C. Germann, A. Misra, Structure and shear deformation of metallic crystalline–amorphous interfaces, Acta Mater., 61 (2013) 3600-3611.

[20] H. Van Swygenhoven, P.M. Derlet, Grain-boundary sliding in nanocrystalline fcc metals, Physical Review B, 64 (2001) 224105.

[21] S. Plimpton, Fast Parallel Algorithms for Short-Range Molecular Dynamics, Journal of Computational Physics, 117 (1995) 1-19.

[22] Y.Q. Cheng, E. Ma, H.W. Sheng, Atomic Level Structure in Multicomponent Bulk

Metallic Glass, Phys. Rev. Lett., 102 (2009) 245501.

[23] F. Shimizu, S. Ogata, J. Li, Theory of Shear Banding in Metallic Glasses and Molecular Dynamics Calculations, MATERIALS TRANSACTIONS, 48 (2007) 2923.

[24] A.S. Clarke, H. Jónsson Structural changes accompanying densification of random hard-sphere packings, Physical Review E, 47 (1993) 3975.

[25] A. Hasnaoui, H. Van Swygenhoven, P.M. Derlet, Cooperative processes during plastic deformation in nanocrystalline fcc metals: A molecular dynamics simulation, Physical Review B, 66 (2002) 184112.

[26] P.M. Derlet, S. Van Petegem, H. Van Swygenhoven, Calculation of x-ray spectra for nanocrystalline materials, Physical Review B, 71 (2005) 024114.

[27] M. Imaeda, T. Mizoguchi, Y. Sato, H.S. Lee, S.D. Findlay, N. Shibata, T. Yamamoto, Y. Ikuhara, Atomic structure, electronic structure, and defect energetics in [001](310)5 grain boundaries of $SrTiO_3$ and $BaTiO_3$, Physical Review B, 78 (2008) 245320.

[28] Y.M. Wang, R.T. Ott, M.F. Besser, A.V. Hamza, Temperature-dependent competing deformation mechanisms in nanocrystalline metals, Physical Review B, 85 (2012) 144122.

[29] T. Frolov, Y. Mishin, Thermodynamics of coherent interfaces under mechanical stresses. II. Application to atomistic simulation of grain boundaries, Physical Review B, 85 (2012) 224107.

[30] E.-M. Steyskal, B. Oberdorfer, W. Sprengel, M. Zehetbauer, R. Pippan, R. Würschum, Direct Experimental Determination of Grain Boundary Excess Volume in Metals, Phys. Rev. Lett., 108 (2012) 055504.

[31] D. Prokoshkina, V.A. Esin, G. Wilde, S.V. Divinski, Grain boundary width, energy and self-diffusion in nickel: Effect of material purity, Acta Mater., 61 (2013) 5188-5197.

[32] P. Simon, U. Schwarz, R. Kniep, Hierarchical architecture and real structure in a biomimetic nano-composite of fluorapatite with gelatine: a model system for steps in dentino- and osteogenesis?, J. Mater. Chem., 15 (2005) 4992-4996.

[33] P.M.D.A.A.G.F. H. VAN SWYGENHOVEN, Stacking fault energies and slip in nanocrystalline metals, Nat. Mat, 3 (2004) 399.

[34] D. Farkas, Atomistic theory and computer simulation of grain boundary structure and diffusion, J. Phys.: Condens. Matter, 12 (2000) R497.

[35] S. Ogata, J. Li, S. Yip, Ideal pure shear strength of aluminum and copper, Science, 298 (2002) 807-811.

[36] J. Eckert, J. Das, S. Pauly, C. Duhamel, Processing routes, microstructure and mechanical properties of metallic glasses and their composites, Adv. Eng. Mater., 9 (2007) 443.

[37] K. Lu, J. Lu, Nanostructured surface layer on metallic materials induced by surface

mechanical attrition treatment, Materials Science and Engineering: A, 375–377 (2004) 38-45.

[38] M.F. Yan, Y.Q. Wu, R.L. Liu, Grain and grain boundary characters in surface layer of untreated and plasma nitrocarburized 18Ni maraging steel with nanocrystalline structure, Appl. Surf. Sci., 273 (2013) 520-526.

[39] S.V. Divinski, G. Reglitz, G. Wilde, Grain boundary self-diffusion in polycrystalline nickel of different purity levels, Acta Mater., 58 (2010) 386-395.

Chapter 7: Effect of amorphous $Cu_{46}Zr_{54}$ coating layer on the mechanical response of copper nanowire

7.1 Introduction

Nanowire, as an one-dimensional nano material, having extremely large free surface to volume ratio, exhibits unique and diverse physical properties in different material systems, enabling extensive potential applications in future nanotechnology [1, 2]. To guarantee the usage and reliability of nanowire in service, the understanding of its mechanical properties under real environmental conditions is necessary. Several comprehensive reviews [3-5] have proposed that surface influences the mechanical response of nanowire via multiple mechanisms including surface stress, emission and annihilation of dislocations. Surface structure has significant impact on the mechanical properties of nanowire and micropillars, e.g. on their surface facets [6] and surface coatings [7-10]. However, most nanowires can have an amorphous surface layer and there is still a lack of study of the impact of amorphous coating layer on nanowire's mechanical responses.

The presence of an amorphous layer on nanowire is quite common in experimental observations. Extensive studies have revealed the formation of amorphous layers on silicon, boron and silicon carbide nanowire/nanopillar. These amorphous coating layers can be induced by oxidation as soon as nanowires contact air. Even for CuO nanowire, an amorphous layer can be formed during the cooling-down process [11]. Metallic nanowires inevitably suffer from oxidation. G.Y. Jing [12] *et al* found that silver nanowire with a diameter of 46.6nm has an oxidation layer with a thickness of 3.8nm. They also confirmed that an oxidation layer, thick or thin, always exists on the surface of silver nanowires of different diameters. Jing [12] *et al.* did not measure the crystallinity of the oxidation layer, instead, amorphous oxidation layers have been observed on Zn [13] and Cu nanowires [14]. Jang [14] *et al.* observed that focused ion beam (FIB) prepared nanotwinned copper nanowire with a diameter of 50nm has an oxidation layer with a thickness of about 5nm. Furthermore, they confirmed that this oxidation layer is of amorphous structure. Jennings [15] *et al.* found that their electroplated copper nanowire was coated by an amorphous tungsten layer. In addition to nanowires prepared by the “bottom-up” approach, Kiener [16] *et al.* suggest that focused ion beam (FIB) may generate amorphous structure on the surface of nanowire.

It has been pointed out that the amorphous layer on the surface of micropillars and nanopillars of sufficient diameter can cause dislocation pile-ups within the metallic crystalline core [16]. Amorphous layer coated nanowire has similar heterogeneous morphology to that of artificially coated pillars. There is little literature on the effect of a coating layer on the plastic deformation of nanowire. Gu and Ng [9, 10] et al. deposited a tungsten coating on an aluminum micropillar and Jennings [8] *et al.* utilized atomic layer deposition to coat a conformal TiO_2/Al_2O_3 layer onto copper micropillars. In situ compression tests on tungsten coated aluminum micropillars showed that, for larger diameters, coating can lead to the trapping of dislocation motion within the crystalline core, and that for smaller diameters coating cannot trap dislocation but can still strengthen micropillars, while Jennings *et al.* found that coated copper pillars retain the jerky flow after yielding and exhibit relative Bauschinger effect. Dislocation dynamics (DD) [7, 17, 18] has been adopted to simulate uniaxial deformation of hard or soft layer coated micropillars and has revealed increased flow stress due to Taylor hardening, as a result of the trapping of dislocation motion. However, these DD simulations are based on single arm dislocation source mechanism (SAS) and focus on diameters of 70nm or larger. For metallic nanowires, their plasticity is convincingly determined by dislocation emission and annihilation on free surface [3, 4, 19, 20], which is currently beyond the scope of DD simulation. While, previous studies have shown that an amorphous/crystalline interface has surprising impact on plasticity [21], indicating that amorphous layer coated nanowires may exhibit different mechanical responses from their pristine counterparts. Though a recent MD simulation [22] reproduced the dislocation confinement in nanopillars by setting surface atoms as radically fixed, this assumption of rigidity must overestimate the effect of the surface layer on the nanowire's mechanics. Overall there is no literature on directly simulating amorphous layer coated nanowire at atomic scale. In this study, we artificially coated an amorphous $Cu_{46}Zr_{54}$ layer on copper nanowire. For the first time, our study illustrates how such an amorphous layer affects the mechanical response of nanowire.

7.2 Methodology

A sketch of our samples in this study is shown in the inset of Fig. 7.1(a). The crystal core of a nanopillar has perfect FCC structure, whose crystallographic directions are $[01\bar{1}]$ along x-direction, $[2\bar{1}\bar{1}]$ along y-direction and $[111]$ along z-direction respectively. Chemical compositions in the amorphous coating layer contain copper and zirconium, with molar fractions of 46% and 54%, respectively. Atomic interactions are described by the alloy EAM potential developed by Y.Q. Cheng [23] *etc*…. The validity of this potential has been widely accepted. All samples were prepared following the same procedure, first undergoing a static energy minimization followed by being heated from 100K to 1200K in 55ps, then samples were relaxed at 1200K for 0.5ps, and finally quenched from 1200K to 300K in 45ps. During the whole process, uniaxial stress was kept to zero. Zirconium atoms did not diffuse into the crystal core and radial pair functions centered by zirconium atoms confirmed that all coating layers had amorphous structure.

The LAMMPS [24] software package was employed for all simulations. Before tensile deformation, all samples were equilibrated at a temperature of 300K for 15ps with no uniaxial external stress along the z-direction. Uniaxial tensile deformation along the z-direction of all samples was conducted via a scale-relaxation method. The strain rate and temperature for all samples were $5 \times 10^8/s$ and *300* K, respectively. Stress was computed following the Virial formula. The Ackland [25] method was utilized to analyze local atomic structure. The OVITO [26] software package was used for visualization of our simulations, including visualization of von Mises atomic shear strain.

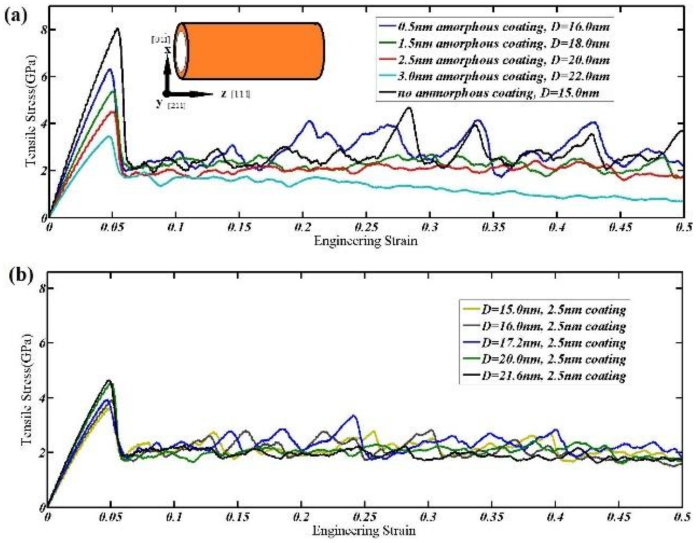

Figure 7.1. Tensile stress versus engineering strain curves for: (a) copper nanowires with same crystalline core diameter (*15.0nm*) but varying amorphous coating thickness; (b)

copper nanowires with same amorphous coating thickness but varying diameter. The inlet in (a) is a sketch of models used in simulations.

7.3 Results

The tensile stress versus engineering strain curves for *<111>* oriented copper nanowire ($r=7.5nm$) with amorphous $Cu_{46}Zr_{54}$ coating layer on the surface (thickness varying from *0.5nm* to *3.0nm*) and without coating layer are shown in Fig. 7.1(a). Fig. 7.1(b) shows the stress versus engineering strain for copper nanowire of varying diameter coated by an amorphous layer of thickness *2.5nm*. The chemical compositions of coatings corresponding to the curves in Fig. 7.1 are all $Cu_{46}Zr_{54}$. Bulk metallic glass (BMG) with the same chemical composition exhibits Young's modulus of *83.5GPa* and yield strength of *1.40GPa,* obtained by an extra MD simulations in this study. It's clear that the mechanical responses of copper nanowire with a coating thickness of only *0.5nm* show similarities to those of the non-coated one-for instance, the serrated flow. The same serrated flow can also be observed in stress-strain curves for copper nanowire of small diameter (*D=15.0, 16.0, 17.2nm*) in Fig. 7.1(b), but with significantly lower magnitude of fluctuation. However, coatings with thicknesses of *1.5nm, 2.5nm and 3.0nm* drive the mechanical response of coated nanowire far away from that of its pure crystalline counterpart. To illustrate the dissimilarities between the mechanical responses of amorphous coated and non-coated copper nanowires, Young's modulus, ultimate tensile strength and yield strain are compared among the samples.

Young's modulus of all samples is obtained by linearly fitting stress-strain curves with engineering strain being smaller than *1.5%*. The Young's Modulus versus coating thickness curve is shown in Fig. 7.2(a). It must be emphasized that the amorphous coating can significantly reduce the Young's modulus of copper nanowire – for example, by nearly a half, from *168GPa* in a non-coated pillar to *94.4GPa* in a *3.0nm* coated pillar. Even though the thinnest coating (*0.5nm*) only slightly reduces Young's modulus, a trend that *E* decreases with increasing thickness of coating can be concluded from Fig. 7.2(a). Fig. 7.2(b) reveals a significant trend: *E* increases with increasing coating thickness in nanowire with a *2.5nm* amorphous coating layer. It's also clear that the Young's modulus depicted in Fig. 7.2(b) is at most 66% of that of a non-coated nanopillar, and 58% of that of the bulk modulus (*191GPa*).

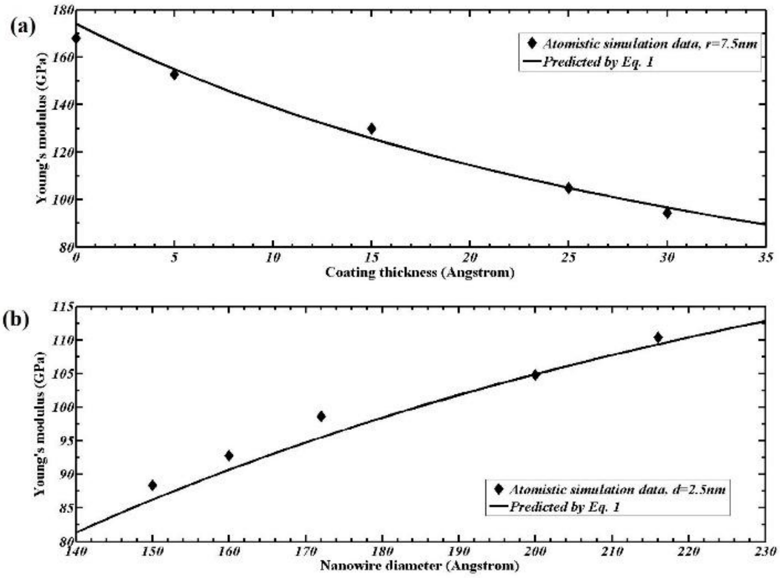

Figure 7.2. Young's modulus for: (a) copper nanowires with same crystalline core diameter (*15.0nm*) but varying amorphous coating thickness; (b) copper nanowires with same amorphous coating thickness but varying diameter.

The strong dependence of Young's modulus on nanowire diameter indicated in Fig. 7.2 is rarely seen in other MD simulations with nanowire diameter falling into the range that we have discussed. This fact enhances the diversity of the trends by which Young's modulus varies with diameter. Previous experiments have suggested different size dependencies of Young's modulus on nanowire diameter. Increase in Young's modulus with decreasing diameter ranging from *140nm* to *20nm* has been observed in silver nanowire [12, 27]. The same trend also occurs in lead [27] and ZnO [28] nanowires. In contrast, the opposite tendency has been revealed in Cr and Si nano-cantilevers. However, gold nanowire doesn't show size dependence when its diameter lies between *40nm* and *250nm* [29]. The tendency of Young's modulus to vary with diameter can be attributed to whether the surface layer is stiffer than crystal bulk. Nanowire can be assumed to consist of outmost surface layer and crystal core, due to the large surface atoms to bulk atoms ratio. Models obtained by atomistic simulations have been employed in explaining whether the surface layer is stiffer than the crystal core. By using both MD and *ab-initio* calculations, Zhou and Huang [30] proposed that the reason that surface layer can be stiffer than bulk is that the stiffening of surface due to surface electron redistribution can overcome the softening due to surface bonding loss. Haiyi Liang *et al.* attributed the size-dependent elasticity of nanowire to the nonlinear response of the crystalline core by comparing the mechanical response of copper nanowire which suffers from compressive strain induced by surface stress with that of strained bulk copper along the same directions. However, even though atomistic models are quite encouraging for explaining different size dependence of Young's modulus, these simulations still ignore very important structural features of nanowires and are quite different from experimental results. First, the diameter of nanowire in these models is very small in comparison to that used in experiments and the surface effect may thus be overestimated. Second, very few simulations have considered surface defects which may manipulate the nanowire's mechanical response. Most importantly, no MD simulations have considered the effect of the coating layer which should widely present on surface of nanowire due to oxidation or preparation process.

A continuum core-shell model was employed to interpret the Young’s modulus versus coating thickness relationship. Nanowire is regarded as made of coating layer and crystal interior which undergo the same tensile strain during elastic deformation. Then the Young’s modulus of a coated nanowire can be expressed by the volume fraction core-shell rule, as in Eq. 7.1 in which D, d, $E_{crystal}$ and E_{coat} are the diameter of nanowire, the coating thickness, and the Young’s modulus of crystal interior and amorphous coating, respectively. By fitting Eq. 7.1 to our MD simulation results, $E_{crystal}$ and E_{coat} are determined to be *174GPa* and *16GPa*, respectively. It should be noted that fitted $E_{crystal}$ is quite close to *190GPa*, which is the Young’s modulus of crystal copper along *<111>* crystallographic direction, while fitted E_{coat} is far away from the Young’s modulus of BMG with the same chemical composition. This indicates that the atomic structure of our coating layer is distinct from that of BMG. A finite width of amorphous/crystalline interface has been reported to be about *1~2nm* elsewhere [31, 32]; the free surface also affects the coating’s atomic structure. Since the thickness of amorphous coatings in our samples was too thin ($\leq 3.0nm$), a different atomic structure in our amorphous $Cu_{46}Zr_{54}$ coating layers than that in BMG was yielded due to surface effect. Thus it’s reasonable that the fitted Young’s modulus of the coating layer should be as low as *16GPa*. In particular, by substituting $D=50nm$ and $d=5nm$ in Eq. 7.1, a modulus of *117GPa* is obtained. Direct tensile test[14] on nanotwinned *<111>* nanowire with diameter of *50nm* yields a Young’s modulus of about *60GPa*, which is only a third of the theoretical value and about half of our predicted value. Our results may help explaining the dramatic Young’s modulus reduction of nanotwinned copper nanowire with an amorphous oxidation coating layer whose Young's modulus should be lower than 81.6GPa [11]. Together with the probable presence of an oxide layer on most metallic nanowires, our model implies that the heterogeneous structure of nanowire may be another cause of the size dependence of Young's modulus. As an exception, gold nanowire is hardly oxidized and thus has very small size dependence on elasticity [29].

$$E = E_{crystal}(1-2d/D)^2 + E_{coat}[1-(1-2d/D)^2]$$

Eq. 7.1

The clear size dependent plasticity, as shown in Fig. 7.1 and Fig. 7.2, of an amorphous coated layer can also be observed. We simultaneously observed suppression of serrated flow and significant reduction in strength of amorphous coated copper nanowires. Fig. 7.1 shows that the post-yielding plastic deformation behavior varies with coating thickness. A sample with 0.5nm coating shows significant serrated flow to be the same as that for a non-coated sample, while a two and an half nanometer coated sample shows nearly ideal plasticity. The suppression of serrated flow agrees well with the compression tests on micropillars with conformal coating, indicating different plastic deformation behavior within amorphous layer coated nanowire core from that in a pristine nanowire. The stress and strain at the peak of the stress-strain curve are defined as ultimate tensile stress (UTS) and yield strain (YS), respectively. It is shown that amorphous coating can induce significant reduction in both UTS and YS. In MD simulations of tensile deformation of metallic nanowire and nanopillars, UTS and YS correspond to the nucleation of dislocation. Since samples used in this study contained no initial dislocations, the quick stress relaxation observed on all stress-strain curves was induced by a massive increase of dislocation density, after which UTS was reached. UTS and YS are quantitative descriptions of the ability of a nanowire with no initial dislocation to deform elastically. In our simulations, UTS for pristine copper nanowire was about *8.0GPa*, which is consistent with previous MD simulations [33], while UTS for coated nanowire with a *3.0nm* thick coating was only about *3.4GPa*, less than half of that for non-coated nanowire. The tendency for UTS to decrease with increasing coating thickness is clearly shown in Fig. 7.3(a). The reason for this trend may be that coating layer lowers the critical stress required for dislocation nucleation at the interface between amorphous layer and crystalline core. Fig. 7.3(c) shows that the strength of nanowires with same coating thickness increases with increasing diameter. Jennings [8] *et al.* have experimentally demonstrated this trend of strength in conformally passivated copper micropillars. As another yield signature, YS for pristine nanowire is determined to be *5.4%*, larger than that of any coated nanowire in this study. Fig. 7.3(c) depicts that a maximum YS is reached when coating thickness is *2.5nm* among coated nanowires. However, Fig. 7.3(d) shows no obvious pattern of how YS varies with nanowire diameter.

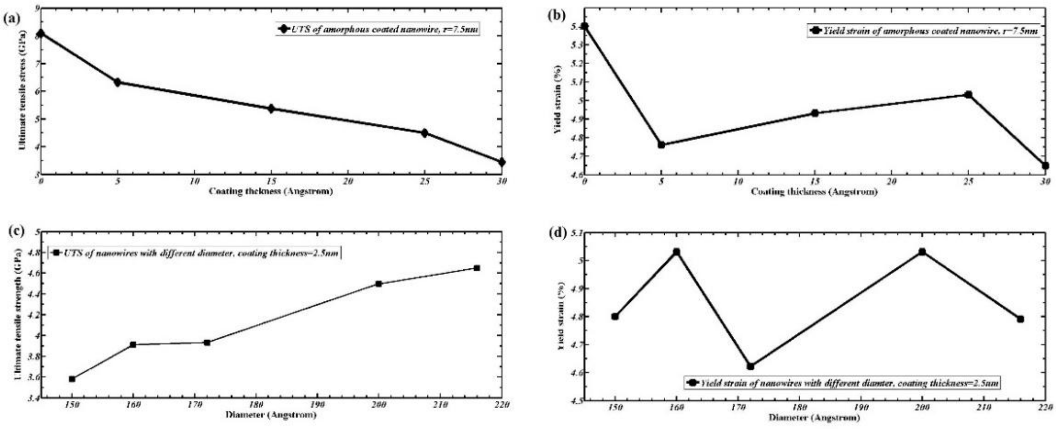

Figure 7.3. Ultimate tensile strength (UTS) and yield strain (YS) for: (a) copper nanowires with same crystalline core diameter (*15.0nm*) but varying amorphous coating thickness; (b) copper nanowires with same amorphous coating thickness but varying diameter.

The size dependence of yield strength shown in Fig. 7.3(a) and (c) can also be attributed to the heterogeneous structure of coated nanowire. It is proposed in this study that the presence of an amorphous coating layer on Cu nanowire can reduce the yield strength by as much as ~57.5% of the magnitude of the yield strength of a pristine one. As a comparison, a preset circumferential surface defect results in a drop in yield strength of ~36% relative to pristine Cu nanowire[33]. It should also be noted that the reduction in yield strain induced by surface defects[33] is much larger than that observed in this study. A circumferential surface defect functions mostly as a stress concentrator during deformation and cannot significantly reduce the Young's modulus of nanowire, thus it can reduce significantly both yield strength and yield strain of nanowire via lowering the dislocation nucleation energy barrier. With a circumferential surface defect, the amorphous coating layer can reduce both the Young's modulus of nanowire and yield strength, but not yield strain. This fact suggests that an amorphous layer may not be able to lower as much dislocation nucleation energy as a circumferential surface defect. It can be concluded that the yield stress reduction induced by the amorphous coating layer occurs mostly because the amorphous layer is much softer than the crystalline core. Increasing yield strength with increasing diameter in this study is a direct result of the fact that the fraction of amorphous layer atoms decreases with increasing diameter. It also needs to be emphasized that the amorphous coating layer may have only a small effect on yield strength of Cu nanowire when the diameter is larger than *100nm* (volume fraction of amorphous layer is smaller than 9.75%, assuming amorphous oxidation layer thickness is smaller than *2.5nm*).

Our simulations reveal that an amorphous coating layer can affect the yield strength of nanowire due to simple load sharing. Previous MD simulations quite convincingly show that the yield strength of nanowire directly depends on the activation energy of dislocation nucleation. Recently Jennings *et al.* have proposed an analytical model based on quantitative description of surface dislocation nucleation energy to predict yield strength of nanowire under experimental conditions [34] by employing a survival probability model proposed by Zhu [20] et. al. They achieved reasonable agreement of the analytical model with the results of experiments on Au nanowire. However, their model yields a strength ten times larger than the experimental results for Cu nanowire, even though the model agrees well with MD simulations. Possible reasons for this large discrepancy include the presence of surface roughness and pre-existing defects. Our simulations indicate that another possible reason may be the fact that atomistic simulations fail to describe the presence of an amorphous oxidation layer on copper nanowire, which may significantly reduce its strength. The absence of an oxidation layer on gold nanowire may be the reason why the Jennings model [34] agrees well with experimental results.

To make clear the underlying mechanism behind the yielding of amorphous layer coated nanowire, both atomic strain analysis and atomic structure analysis are employed. Fig. 7.4 shows an atomic strain distribution evolution of nanowire with *2.5nm* thick coating (*r=7.5nm)* during deformation via a perspective view. Only surface atoms and HCP atoms in the crystalline core in half a nanowire are shown in Fig. 7.4, and colored by von Mises atomic shear strain. Single atomic planes within the crystalline core represent Shockley partial dislocations. It can be clearly deduced from Fig. 7.4(a) that spots with atomic shear strain concentration appear at the interface between amorphous coating layer and crystalline core when strain is *3.0%*, which is before UTS is reached. These spots are akin to shear transformation zones (STZs), which are the elementary plastic deformation carriers in bulk metallic glass [35, 36] (BMG). The coating layers yield in a way akin to STZ formation [23, 37]. Another supporting evidence of coating layer yielding is the significant deviation from linear relation before UTS is reached on stress-strain curves, as shown in Fig. 7.1. Similarly, surface atoms can also be rearranged in pristine crystal nanowire, contributing to deformation before the yielding point. The surface rearrangement mechanism and its connection with further deformation in pristine nanowire still remains unclear. However, in this study, the rearrangement of coating layer atoms has significant impact on dislocation behaviors, including on both nucleation and slip in the crystal core.

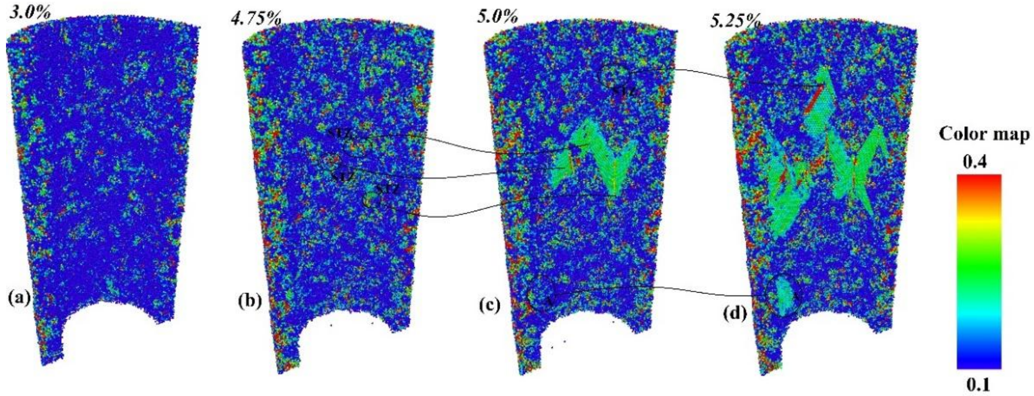

Figure 7.4. Von Mises atomic shear strain maps of copper nanowire with different strain. Amorphous coating thickness is *2.5 nm*, overall diameter is *20 nm*. Only surface atoms and HCP atoms in crystalline core in half a nanowire are shown. Atoms are colored by von Mises atomic shear strain. Single atomic planes within crystalline core represent partial dislocations.

We observed a dislocation nucleation mechanism in nanowire distinct from the surface nucleation mechanism. The crystalline core of nanowire yields via dislocation nucleation from STZs at the interface between coating and crystal. Fig. 7.4(b) and (c) show that three individual STZs within the amorphous coating, when strain is *4.75%,* developed into multiple partial dislocations within the crystalline core when strain increases to *5.0%,* which was just a bit earlier before the yield point on the stress-strain curve. Fig. 7.4(c) and (d) show that two more individual STZs within the coating induced partial dislocations within the crystalline core when strain increased to *5.25%,* which resulted in the dramatic stress relaxation on the stress-strain curve after UTS is reached. This STZs-trigger-dislocation mechanism is very similar to that observed in previous MD simulation of amorphous/crystalline nanolaminates [21]. The knowledge obtained in MD simulations on BMG [38, 39] has suggested that the diameter of STZs is at the scale of the thickness of the coating layer used in this study. Thus STZs induced by inelastic atomic rearrangement of a thin coating surface layer during tensile loading mostly reside near the amorphous/crystal core interface. STZs have higher energy than neighboring amorphous regions and are able to activate dislocation nucleation [21, 36, 38]. The activation volume of the STZ-triggered dislocation mechanism is close to that of dislocation nucleation on a “perfect” free surface [40].

When amorphous coating layer is thicker than *0.5nm,* simulations results clearly paint a physical picture that the interface between amorphous coating layer and crystal core can provide multiple dislocation nucleation sites via formation of STZs before overall yielding of the nanowire. This mechanism is responsible for the ability of an amorphous coating layer with enough thickness to suppress dislocation starvation states in nanowires during loading and to induce ideal flow instead of serrated flow. Dynamic atomic microstructure evolution processes visualized by OVITO show dislocation structure evolution for *2.5nm* and *0.5nm* coated samples, respectively. Atoms are colored according to their local structures, yellow dots represent HCP atoms and FCC atoms have been removed. Multiple dislocation starvation states during the dislocation evolution process can be clearly seen during deformation of the *0.5nm* coated sample. However, no such dislocation starvation states appear during deformation of the *2.5nm* coated sample. Fig. 7.1 shows that the *0.5nm* coated sample is the only one that demonstrates serrated flow similar to that of non-coated nanowire. The reason is that *0.5nm* coating thickness is lower than typical size of STZ [36, 38], and is not able to support the STZ-trigger-dislocation mechanism. It can be concluded that an amorphous coating layer (thickness>*0.5nm*) can provide a significant suppression effect on serrated flow. The transformation between STZ within the amorphous layer and dislocation within the crystalline layer at the interface accounts for the experimentally observed near-ideal plasticity [21]. In our study, the absence of a dislocation starvation state in most coated samples indicates that an amorphous/crystalline interface can provide both continuum dislocation sources and dislocation annihilation sinks during deformation. Thus it’s rather reasonable to suppose that a stable plastic flow can be sustained in amorphous layer coated nanowire. Our simulation can help explain the absence of serrated flow in a recent test on nanotwinned copper nanowire [14]. It should be also noted that the continuum dislocation nucleation and annihilation mechanism shown here is unlike the mechanism which indicates that dislocation pile ups can be formed within hard coated micropillars, which show an increase in compressive strength [7, 9, 10, 18, 22].

7.4 Conclusion

In summary, the mechanical response of copper nanowire coated by an amorphous $Cu_{46}Zr_{54}$ layer has been investigated by molecular dynamics. Significant size dependent elasticity and plasticity of copper nanowire have been observed. Young's modulus and yield strength of nanowire are found to decrease with increasing coating thickness and decreasing nanowire diameter. A new plastic deformation mechanism for nanowire has been observed in this study. The amorphous layer yields first via STZ formation without the overall yielding of nanowire. Then dislocation nucleates from STZs at the interface between amorphous shell and crystalline core induce yielding and stable plastic flow. This mechanism enables the suppression of serrated flow which has been frequently observed in atomistic simulations of nanowire due to the establishment of dislocation starvation states during deformation. A simple core-shell model is utilized to explain our results and help explain experimental results.

Reference

[1] H.G. Craighead, Nanoelectromechanical Systems, Science, 290 (2000) 1532-1535.

[2] C.M. Lieber, Z.L. Wang, Functional Nanowires, MRS Bull., 32 (2007) 99-108.

[3] T. Zhu, J. Li, S. Ogata, S. Yip, Mechanics of Ultra-Strength Materials, MRS Bull., 34 (2009) 167-172.

[4] H.S. Park, W. Cai, H.D. Espinosa, H. Huang, Mechanics of Crystalline Nanowires, MRS Bull., 34 (2009) 178-183.

[5] O. Kraft, P.A. Gruber, R. Mönig, D. Weygand, Plasticity in Confined Dimensions, Annual Review of Materials Research, 40 (2010) 293-317.

[6] C. Deng, F. Sansoz, Effects of twin and surface facet on strain-rate sensitivity of gold nanowires at different temperatures, Physical Review B, 81 (2010) 155430.

[7] C. Zhou, S. Biner, R. LeSar, Simulations of the effect of surface coatings on plasticity at small scales, Scripta Mater., 63 (2010) 1096-1099.

[8] A.T. Jennings, C. Gross, F. Greer, Z.H. Aitken, S.W. Lee, C.R. Weinberger, J.R. Greer,

Higher compressive strengths and the Bauschinger effect in conformally passivated copper nanopillars, Acta Mater., 60 (2012) 3444-3455.

[9] R. Gu, A.H.W. Ngan, Effects of pre-straining and coating on plastic deformation of aluminum micropillars, Acta Mater., 60 (2012) 6102-6111.

[10] K.S. Ng, A.H.W. Ngan, Effects of trapping dislocations within small crystals on their deformation behavior, Acta Mater., 57 (2009) 4902-4910.

[11] E.P.S. Tan, Y. Zhu, T. Yu, L. Dai, C.H. Sow, V.B.C. Tan, C.T. Lim, Crystallinity and surface effects on Young's modulus of CuO nanowires, Appl. Phys. Lett., 90 (2007) -.

[12] G.Y. Jing, H.L. Duan, X.M. Sun, Z.S. Zhang, J. Xu, Y.D. Li, J.X. Wang, D.P. Yu, Surface effects on elastic properties of silver nanowires: Contact atomic-force microscopy, Physical Review B, 73 (2006) 235409.

[13] Y. Yan, P. Liu, M.J. Romero, M.M. Al-Jassim, Formation of metallic zinc nanowires, J. Appl. Phys., 93 (2003) 4807-4809.

[14] D. Jang, X. Li, H. Gao, J.R. Greer, Deformation mechanisms in nanotwinned metal nanopillars, Nat Nano, 7 (2012) 594-601.

[15] A.T. Jennings, J.R. Greer, Tensile deformation of electroplated copper nanopillars, Philosophical Magazine, 91 (2010) 1108-1120.

[16] D. Kiener, C. Motz, M. Rester, M. Jenko, G. Dehm, FIB damage of Cu and possible consequences for miniaturized mechanical tests, Materials Science and Engineering: A, 459 (2007) 262-272.

[17] R. Gu, A.H.W. Ngan, Dislocation arrangement in small crystal volumes determines power-law size dependence of yield strength, Journal of the Mechanics and Physics of Solids, 61 (2013) 1531-1542.

[18] J.A. El-Awady, S.I. Rao, C. Woodward, D.M. Dimiduk, M.D. Uchic, Trapping and escape of dislocations in micro-crystals with external and internal barriers, Int. J. Plast., 27 (2011) 372-387.

[19] J. Li, The mechanics and physics of defect nucleation (vol 32, pg 151, 2007), MRS Bull., 32 (2007) 462-462.

[20] T. Zhu, J. Li, A. Samanta, A. Leach, K. Gall, Temperature and Strain-Rate Dependence of Surface Dislocation Nucleation, Phys. Rev. Lett., 100 (2008) 025502.

[21] Y. Wang, J. Li, A.V. Hamza, T.W. Barbee, Ductile crystalline–amorphous nanolaminates,

Proceedings of the National Academy of Sciences, 104 (2007) 11155-11160.

[22] S. Xu, Y.F. Guo, A.H.W. Ngan, A molecular dynamics study on the orientation, size, and dislocation confinement effects on the plastic deformation of Al nanopillars, Int. J. Plast., 43 (2013) 116-127.

[23] Y.Q. Cheng, E. Ma, H.W. Sheng, Atomic Level Structure in Multicomponent Bulk Metallic Glass, Phys. Rev. Lett., 102 (2009) 245501.

[24] S. Plimpton, Fast Parallel Algorithms for Short-Range Molecular Dynamics, Journal of Computational Physics, 117 (1995) 1-19.

[25] G.J. Ackland, A.P. Jones, Applications of local crystal structure measures in experiment and simulation, PHYsical Review B, 73 (2006) 054104.

[26] S. Alexander, Visualization and analysis of atomistic simulation data with OVITO–the Open Visualization Tool, Modell. Simul. Mater. Sci. Eng., 18 (2010) 015012.

[27] S. Cuenot, C. Frétigny, S. Demoustier-Champagne, B. Nysten, Surface tension effect on the mechanical properties of nanomaterials measured by atomic force microscopy, Physical Review B, 69 (2004) 165410.

[28] C.Q. Chen, Y. Shi, Y.S. Zhang, J. Zhu, Y.J. Yan, Size Dependence of Young’s Modulus in ZnO Nanowires, Phys. Rev. Lett., 96 (2006) 075505.

[29] B. Wu, A. Heidelberg, J.J. Boland, Mechanical properties of ultrahigh-strength gold nanowires, Nat Mater, 4 (2005) 525-529.

[30] L.G. Zhou, H. Huang, Are surfaces elastically softer or stiffer?, Appl. Phys. Lett., 84 (2004) 1940-1942.

[31] C. Brandl, T.C. Germann, A. Misra, Structure and shear deformation of metallic crystalline–amorphous interfaces, Acta Mater., 61 (2013) 3600-3611.

[32] C.R.S. da Silva, A. Fazzio, Formation and structural properties of the amorphous-crystal interface in a nanocrystalline system, Physical Review B, 64 (2001) 075301.

[33] Z.X. Wu, Y.W. Zhang, M.H. Jhon, J.R. Greer, D.J. Srolovitz, Nanostructure and surface effects on yield in Cu nanowires, Acta Mater., 61 (2013) 1831-1842.

[34] A.T. Jennings, C.R. Weinberger, S.-W. Lee, Z.H. Aitken, L. Meza, J.R. Greer, Modeling dislocation nucleation strengths in pristine metallic nanowires under experimental conditions, Acta Mater., 61 (2013) 2244-2259.

[35] A.L. Greer, Y.Q. Cheng, E. Ma, Shear bands in metallic glasses, Materials Science and Engineering: R: Reports, 74 (2013) 71-132.

[36] L. JS, Shear-transformation-zone theory of deformation in metallic glasses, Scr. Mater., 54 (2006) 375.

[37] Y.Q. Cheng, E. Ma, Atomic-level structure and structure–property relationship in metallic glasses, Prog. Mater Sci., 56 (2011) 379-473.

[38] Z. M, S. K, J. WL, M. SG, Plastic deformation of metallic glasses: size of shear transformation zones from molecular dynamics simulations, Phys. Rev. B, 73 (2006) 172203.

[39] S.G. Mayr, Activation Energy of Shear Transformation Zones: A Key for Understanding Rheology of Glasses and Liquids, Phys. Rev. Lett., 97 (2006) 195501.

[40] Y.M. Wang, A.V. Hamza, T.W. Barbee, Incipient plasticity in metallic glass modulated nanolaminates, Appl. Phys. Lett., 91 (2007) -.

Chapter 8: Conclusion and future work

The study of interfacial plasticity will benefit our understanding of mechanical response of materials, and provide atomistic insights for designing materials with both high strength and ductility. Interface mediated deformation mechanisms revealed by molecular dynamics may be employed in continuum mechanics modeling of materials at meso scale in future. In this dissertation, interfacial plasticity in several typical nanomaterials including nanocrystalline, nanotwinned, nanowire and nanolaminate materials has been studied by molecular dynamics. The research focused on atomistic deformation mechanisms mediated by different interfaces and their relationship with macro mechanical responses of materials of interest. In general, major conclusions are made in this dissertation as follows:

1. In nanocrystalline copper, appropriate multi-mode deformation was confirmed to be able to generate high density of nano twins by molecular dynamics. Shearing after a compression to the elastic limit is the best formation condition for deformation twin nucleation. Two deformation mechanisms to nucleate twins were observed: one via Shockley partial dislocation glide on neighboring (111) planes and another via three Shockley partial dislocation slips. The reaction between deformation twin and partial dislocation were also observed.
2. By simulating uniaxial tensile deformation along the <111> direction of nano twinned single crystal copper, it was found that twin boundary cannot behave as a dislocation nucleation source and partial dislocations are nucleated from HCP defective atom clusters formed by tensile loading in an originally nearly defect-free crystal structure. Two deformation

mechanisms were observed in samples with different twin spacing. At small twin spacings (<10 nm), partial dislocations with stacking faults are the dominant defect, but when the twin spacing increases, secondary twin boundaries (deformation twins) start to form and the amount of deformation twins increases. The original twin boundary serves as an obstacle to dislocation movements on the glide planes tilted to the twin boundary, resulting in an enhanced flow strength. Thus, the Hall-Petch like relationship is still valid down to very small twin spacings (~1 nm), which can be explained by a simple energy balance model.

3. By changing thermodynamic treatments in molecular dynamics simulation, two types of amorphous/crystalline laminates, in which amorphous layers have different structural heterogeneity, were prepared. Both as-quenched sample and separately-quenched sample yielded first through the formation of STZs in the amorphous layer. After that, micro sliding bands with highly localized atomic shear strain were formed at ACIs in both samples via different interfacial mechanisms, sliding via STZs growth at ACIs for the separately-quenched sample and sliding via dislocation loop spreading at ACIs for the as-quenched sample. The thickening of micro sliding bands on the amorphous side via internal friction is determined to be a new plastic deformation mechanism. The micro sliding band thickening rate was higher in the as-quenched sample than that in the separately-quenched sample. A simple mechanical analysis showed that the thickening of the micro sliding band should be universal for BMG-based composites.

4. The mechanical response of copper nanowire coated by an amorphous $Cu_{46}Zr_{54}$ layer has been investigated by molecular dynamics. Significant size dependent elasticity and plasticity of copper nanowire

have been observed. Young’s modulus and yield strength of nanowire are found to decrease with increasing coating thickness and decreasing nanowire diameter. A new plastic deformation mechanism for nanowire has been observed in this study. The amorphous layer yields first via STZ formation without the overall yielding of nanowire. Then dislocation nucleates from STZs at the interface between the amorphous shell and crystalline core induce yielding and stable plastic flow. This mechanism enables the suppression of serrated flow which has been frequently observed in atomistic simulations of nanowire due to the establishment of dislocation starvation states during deformation. A simple core-shell model is utilized to explain our results and help explain experimental results.

This work has provided direct atomistic insights into interfacial plasticity in several nanomaterials. An ultimate goal is to utilize knowledge obtained in atomistic simulations to guide materials design. However, the bridge between atomistic mechanisms and experimental mechanical responses of true materials currently can only be built by qualitative comparison. Quantitative explanations and prediction of materials’ mechanical properties from molecular dynamics are still not available. To reach our ultimate goal, atomistic simulations and experiments should approach and correct each other. On one hand, more realistic conditions should be considered in atomistic simulations and it is necessary to produce models based on physical picture obtained by atomistic simulation to predict experimental results. On the other hand, experimental condition control, including strain rate, material microstructure and so on, is able to allow direct comparison between atomistic simulations and experiments. In addition, the role of atomistic simulations should be re-considered under the multiscale framework. In nanomaterials, represent volume of material and volume that molecular dynamics can deal with are at the same scale, and thus molecular dynamics has been applied in predicting these materials' mechanical responses. But in traditional materials, mesoscale collective response of microstructural defects manipulates materials' behavior. Atomistic simulations are far from being able to cope with mesoscale. Even though several mesoscale approaches, including dislocation dynamics and crystal plasticity, have been being developed to simulate materials' mechanical responses, there is still a lack of effective modeling methods to deal with interfacial plasticity at mesoscale. With all these considerations, there are many topics which require further investigations.

First, in addition to the interfaces discussed in this dissertation, more interfaces in different material systems, including metal/metal, ceramic/metal, organic/metal, organic/ceramic interfaces and so on, can be modeled by atomistic simulations. It will not be easy to successfully describe such systems due to lack of reliable potential functions, but it is possible to conclude some key features of interfaces for material design.

Second, atomistic simulation at experimental strain rates has eventually become possible. Mechanical response and microstructure evolution of interface at experimental strain rate can be studied by employing potential sampling methods. Such methods will also be utilized to determine two fingerprints of interfacial plasticity: activation volume and activation energy. Atomistic insights obtained by these methods can be directly used as input for mesoscale approaches.

Third, structural biomaterials are very good examples of nanomaterials in which interfaces between organics and minerals are key reasons for their good mechanical performance. Several interfacial plasticity mechanisms in biomaterials have been identified by experiments recently. It will be interesting to repeat these mechanisms observed in biomaterials in atomistic models and to learn material design from nature.

Fourth, recently high intensity laser has been used to generate shockwave propagation in materials and to study the dynamic behavior of materials. In such experiments, targeted foil has a thickness of several micrometers and strain rate generated by laser is about 10^{10}/s. Sample thickness and strain rate in laser loading experiments are quite close to the current capability of molecular dynamics simulation on high performance cluster. It is practical to simulate dynamic responses of and interface at such high strain rate and to directly compare molecular dynamics results with experimental results. Our preliminary results show that shockwave scattering at interfaces in nanolaminates can change both mechanical and thermodynamic responses of local volume, inducing isentropic states in materials.